BEHAVIOR OF TiN INCLUSIONS AND THEIR INFLUENCE IN RANDOM GRAIN FORMATION IN Ni-BASED SUPERALLOYS

by

RAJESWARI SOUNDARARAJAN

B.Sc., Madras University (INDIA), 1990

M.Sc., Anna University (INDIA), 1992

A THESIS SUBMITTED IN PARTIAL FULFILLMENT OF
THE REQUIREMENTS FOR THE DEGREE OF

MASTER OF APPLIED SCIENCE

in

THE FACULTY OF GRADUATE STUDIES

(Department of Metals and Materials Engineering)

We accept this thesis as conforming
to the required standard

THE UNIVERSITY OF BRITISH COLUMBIA

October 1998

In presenting this thesis in partial fulfilment of the requirements for an advanced degree at the University of British Columbia, I agree that the Library shall make it freely available for reference and study. I further agree that permission for extensive copying of this thesis for scholarly purposes may be granted by the head of my department or by his or her representatives. It is understood that copying or publication of this thesis for financial gain shall not be allowed without my written permission.

Department of Metals and Materials Engineering

The University of British Columbia
Vancouver, Canada

Date October 16, 1998

DE-6 (2/88)

Abstract

Studies on the columnar to equiaxed transition and random grain formation in superalloy turbine blades have suggested that non-metallic inclusions may be a possible nucleation source. Though there is no strong evidence to substantiate the idea, during directional solidification if the inclusions are able to survive in the region ahead of the solidification front, they could act as potential nucleation sites and may aid in the formation of random grains. On the basis of the Turnbull-Vonnegut lattice dis-registry model, the lattice mismatch between the FCC Ni-matrix and a typical cubic TiN inclusion is determined to be less than 20%. Hence, a TiN particle can act as a potential heterogeneous nucleant in Ni-based superalloys with sufficient undercooling. The undercooling required in the Ni-based superalloys for TiN inclusion is calculated to be about 19 ^{0}C, which is comparable to the undercooling found in some single crystal superalloy turbine blades. Therefore, if the TiN particles are stable in the region ahead of the liquidus isotherm, they may be potential nucleation sites and hence cause the formation of random grains. This thesis reports on a quantitative study to verify the hypothesis that the TiN particles are stable in the region ahead of the solidification front during directional solidification. Thermodynamic calculations concerning the solubility of nitrogen and the formation of TiN in alloy IN718 have determined that the equilibrium nitrogen content required for the formation of TiN is about 39 ppm [N] (at T_{liq} =1340^{0}C). Experimental studies on alloy IN718 at various conditions have indicated that TiN precipitation will not take place once the equilibrium nitrogen content is below this value of 39 ppm at T_{liq}. In the solid/liquid mushy region, the combined effects factors such as: a) cooling, b) segregation of Ti and nitrogen, and c). rejection of nitrogen into the bulk liquid, reduce the solubility limit to below 39 ppm. Hence TiN precipitation takes place in the segregation zone. The experiments have established that TiN particles precipitated in the solid/liquid mushy zone will not float out of the interface. Therefore, the nitrogen content must

exceed the saturation solubility of TiN at T_{liq} to provide nuclei for random grain formation. Due to nitrogen rejection into the bulk liquid, there is TiN precipitation just above the T_{liq}. Directional solidification (DS) experiments on IN718 samples under nitrogen pressure and at a withdrawal rate of 2.4μm/sec have revealed that TiN particles of size > 10 microns (which have a rise velocity > 28 μm/sec) are able to float and eventually get collected at the top of the ingot (which is the final portion to solidify). These might be the TiN particles that are precipitated in the liquid ahead of the solidification front, i.e. above the T_{liq}, and which subsequently undergo flotation. Smaller TiN particles of size < 4 microns are found at the bottom portions of the ingot which indicates that these particles may be precipitated later during solidification in the solid/liquid mushy zone, and thus didn't "escape" out of the interface. Hence, the withdrawal rate should be at least an order lesser in magnitude than the velocity of rise of the TiN particles for substantial flotation to occur.

Table Of Contents

Abstract	ii
Table of Contents	iv
List of Figures	vii
List of Tables	xii
List of Symbols	xiii
Acknowledgements	xv
Introduction	1
Chapter 2: Literature Review	4
2.1 Random grain formation	4
2.1.1 Fundamentals of CET	5
2.1.1.1 Dendrite Undercooling	7
2.2 Spurious Grain Formation in Ni-Based Alloys	9
2.2.1 Thermosolutal convection	9
2.2.2 Constitutional Undercooling	14
2.3 Criterion For Spurious Grain Nucleation	15
2.4 Inclusions and Random Grain Formation	20
2.5 Thermodynamics of Inclusion Formation	25
2.5.1 Nitrogen in Superalloys	25
2.5.1.1 Solubility of Nitrogen	25
2.5.2 Chemistry of TiN Precipitation	27
2.5.3 Studies in Alloy IN718	29
2.6 Summary	32
Chapter 3: Objectives	34
Chapter 4: Theoretical Methodology for TiN Formation in Alloy IN718	35
4.1 Solubility of Nitrogen in Alloy IN718	35
4.2 Solubility of TiN in Alloy IN718	36

Chapter 5: Experimental Studies 41
5.1 Alloy Compositions used for Experiments 41
5.2 Sample Preparation 41
5.3 Apparatus and Procedure 43
5.4 Metallographic Analysis 47
5.5 Primary Dendrite Arm Spacing 51
5.6. Buoyancy Effect On TiN 54
5.7 Experiments 57
5.7.1 Nitrogen Analysis of the DS cast Samples 60

Chapter 6: Results 61
6.1 Directional Solidification and Quenching Experiments 61
6.2 Directional Solidification experiments 63
6.2.1 Samples 90 ppm [N], and 64 ppm [N] 63
6.2.2 Homogeneous Sample Preparation 66
6.2.3 90 ppm [N] samples DS at 3.5 x 10^{-5} Torr 66
6.2.4 90 ppm [N] DS at 100 microns Nitrogen Pressure 68
6.2.5 90 ppm [N] Sample DS at 400 microns Nitrogen Pressure 72
6.2.6 DS Experiments With 20 ppm [N] Samples 76

Chapter 7: Discussions 80
7.1 Directional Solidification and Quenching Experiments 80
7.2 Directional Solidification (DS) Experiments 80
7.3 Summary of TiN Particle Distribution and Nitrogen Analysis 83
7.4 TiN Particle Distribution 93

Chapter 8: Conclusions and Recommendations 95
8.1 Summary 95
8.2 Recommendations For Future Work 100

References 102

Appendix 1 109
Appendix 2 111
Appendix 3 113
Appendix 4 115
Appendix 5 119
Appendix 6 121
Appendix 7 124
Appendix 8 128

List of Figures

Figure 1. Fatigue properties of IN718, illustrating the influence of inclusions on premature failure at T = 350 °C; strain amplitude = 0.62%. (from [1]). 3

Figure 2. The three regimes of grain defect formation and the dependence on dendrite arm spacing. (from [5]). 10

Figure 3. Isolated mis-oriented columnar grains during directional solidification of alloy SX-1 (after [5]). 11

Figure 4. Complete breakdown of single solidification and blockage of solidification Front by equiaxed grains. (after [6]). 11

Figure 5. A typical freckle chain observed during solidification of alloy SX-1. (from [6]). 12

Figure 6. The dependence of freckle chain formation on primary dendrite arm spacing. (after [6]). 13

Figure 7. Depending upon the undercooling capacity of the given alloy a macroscopic concave curvature of the liquidus isotherm can cause the formation of stray grains (a) or result in fast lateral growth of secondary dendrites (b). (from [35]). 16

Figure 8. Schematic diagram showing the growth of a secondary dendrite arm into a platform in the presence of a transverse temperature gradient. (from[6]). 17

Figure 9. Effect of transverse temperature gradient in alloy CMSX-4. (from [6]). 19

Figure 10. Lattice mis-match vs. nucleation undercooling in delta iron of various oxides, nitrides and carbides. (from [5]). 22

Figure 11. Cooling curves measured at different withdrawal rates. (from [34]). 24

Figure 12. Temperature and solubility dependence of the saturation solubility of TiN. [from 62]. 28

Figure 13. Nitrogen distribution in alloy IN718. (from [63]). 29

Figure 14. Size distribution of TiN inclusions as a function of nitrogen content in alloy IN718, with a constant LST. (from [63]). 30

Figure 15. Dependence of k_{TiN} on Cr content in some superalloys. (from [63]). 30

Figure 16. Temperature dependence of the saturation solubility of TiN in IN718 (from [1]). 31

Figure 17. Relation between superheat and the equilibrium nitrogen contents required for the formation of TiN particles in alloy IN718. 38

Figure 18. Segregation of Titanium in the mushy region in alloy IN718. (from [68]). 39

Figure 19. The DSQ apparatus. 44

Figure 20. Schematic of the DSQ apparatus. 45

Figure 21. Temperature distribution along the induction coil in the DSQ (at 2.5 kW). 46

Figure 22 (a) and (b). Exterior of a directionally solidified ingot (directly taken out from the DSQ). 46

Figure 23. Quenched interface perpendicular to the direction of withdrawal. 49

Figure 24. Quenched interface at an angle to the direction of withdrawal. 49

Figure 25. Schematic quantitative analysis of TiN in (a) DSQ samples, (b) DS samples. 50

Figure 26. A typical TiN inclusion showing a prominent alumina core. 50

Figure 27. Dendrite arm spacings for several directionally solidified superalloys as a function of the cooling rate. (from [69]). 51

Figure 28. Schematic of the mushy interdendritic region in alloy IN718 with TiN Precipitates. 51

Figure 29. SEM picture of the PDS in sample 2(64 ppm [N], DSQ sample). 52

Figure 30. SEM picture of the PDS in sample 1 (68 ppm [N], DSQ sample). 52

Figure 31. Schematic of PDS determination at different sections of the DS cast ingot (sample 5, 64 ppm [N]). 53

Figure 32. Schematic of the stages involved in preparing samples 3 (48 ppm [N]) and 4 (90 ppm [N]). (a) severing the sample in half (b). drilling a hole at the top of the bottom half and, (c). fiiling the hole with Cr_2N and closing it with the upper half. 59

Figure 33. Schematic of the procedure to prepare homogeneous IN718 samples. 59

Figure 34. TiN distribution in the directionally solidified and quenched samples 1 (68 ppm [N], 2 (64 ppm [N]), and 3 (48 ppm [N]) at a withdrawal rate (R) = 8.1 μm/sec. 61

Figure 35. Temperature distribution of TiN particles in the directionally solidified and quenched samples 1(68 ppm [N], 2 (64 ppm [N]), and 3 (48 ppm [N]) at a withdrawal rate (R) = 8.1 μm/sec. 62

Figure 36. TiN distribution in the Directionally solidified sample 4 (90 ppm [N]) at R = 8.1 μm/sec. 63

Figure 37. TiN distribution in the DS samples 5 and 6 (64 ppm [N], from the same alloy B) at R = 8.1 μm/sec. 64

Figure 38. Nitrogen analysis for the DS cast sample 5 (64 ppm [N] at R = 8.1 μm/sec). 65

Figure 39. TiN distribution in the 90 ppm [N] content DS cast IN718 ingots. Sample 7 at R = 8.1 μm/sec and sample 8 at R = 2.4 μm/sec. 67

Figure 40. Nitrogen distribution in 90 ppm [N] content IN718 ingots. Sample 7 at R = 8.1 μm/sec and sample 8 at R = 2.4 μm/sec. 67

Figure 41. Nitrogen distribution in the 90 ppm [N] content IN718 ingots directionally solidified at 100 microns nitrogen pressure. Sample 9 and 10 at R = 8.1 μm/sec and sample 11 and 12 at R = 2.4 μm/sec. 69

Figure 42. TiN distribution in the 90 ppm [N] content IN718 samples directionally solidified at 100 microns nitrogen pressure. Sample 9 at R = 8.1 μm/sec and sample 11 at R = 2.4 μm/sec. 70

Figure 43. (a) and (b) Etched sections from DS samples (90 ppm [N]) showing TiN particles of the very top of the ingot. 71

Figure 44. (a), (b), and (c) TiN particles on the upper outer surface of the ingot. 72

Figure 45. Nitrogen distribution along sample 13 (90 ppm [N] content) directionally solidified at 400 microns nitrogen pressure at a withdrawal rate of 8.1 μm/sec. 73

Figure 46. TiN distribution along sample 13 (90 ppm [N] content) directionally solidified at 400 microns nitrogen pressure at a withdrawal rate of 8.1 μm/sec. 73

Figure 47. (a), (b), and (c) SEM pictures of the top section of sample 13 showing Large TiN particles. 74

Figure 48. (a) and (b) TiN clusters on the outer surface of the DS cast sample 13 (90 ppm [N]). 75

Figure 49. Nitrogen distribution along the 20 ppm [N] directionally solidified ingots at a withdrawal rate of 2.4 μm/sec. Sample 14 and 15 were DS at a nitrogen pressure of 40 microns and samples 16 and 17 were DS at a nitrogen pressure of 10 microns. 77

Figure 50. TiN distribution along the 20 ppm [N] directionally solidified ingots at a withdrawal rate of 2.4 μm/sec. Sample 14 and 15 were DS at a nitrogen pressure of 40 microns and samples 16 and 17 were DS at a nitrogen pressure of 10 microns. 77

Figure 51. (a), (b), and (c) TiN particles found at the very top of the DS ingot (20 ppm [N], at 40 microns nitrogen pressure). 79

Figure 52. Distribution of TiN along the DS cast IN718 ingots at a withdrawal rate of 2.4 μm/sec. 84

Figure 53. Distribution of nitrogen along the DS cast IN718 ingots at a withdrawal rate of 2.4 μm/sec. 85

Figure 54. Distribution of TiN along the DS cast IN718 ingots at a withdrawal rate of 8.1 μm/sec. 86

Figure 55. Distribution of nitrogen along the DS cast IN718 ingots at a withdrawal rate of 8.1 μmsec. 87

Figure 56. Equilibrium nitrogen contents required for the formation of TiN in the l/s mushy region at different temperatures, accounting for Ti segregation. 88

Figure 57. (a) Initial stage during DS (dendrites are beginning to form) (b) intermediate Stage, and (c) final stage of DS. 89

Figure 58. Nitrogen distribution along the DS samples at various k values for nitrogen. 91

Figure 59. TiN particle distribution along the directionally solidified IN718 ingots. Data are from the following samples: 90 ppm [N] samples DS cast at 100 microns nitrogen pressure - sample 11 (at R = 2.4μm/sec) and 20 ppm [N] content sample 14 directionally solidified at a nitrogen pressure of 40 microns, at R = 2.4 μm/sec. 93

Figure 60. TiN saturation solubility ahead of the liquidus from the present studies And a typical casting liquidus[63]. 96

Figure 61. (a), and (b) a hexagonal, and a cubic TiN precipitate respectively. 110

Figure 62. (a) and (b) TiN agglomerations bridged by alumina particles. 112

Figure 63. TiN inclusions bridged by alumina particles. 112

Figure 64. Nitrogen distribution in samples 18, 19 (DS cast under argon pressure of 100 μm), 7 and 8 (DS cast at 3.5 x 10^{-5} Torr, and at 8.1 and 2.4 μm/ sec respectively). 116

Figure 65. TiN distribution in samples (18), (19) (DS cast under argon pressure of 100 μ), (7) and (8) (DS cast at 3.5 x 10^{-5} Torr, and at 8.1 and 2.4 μ/ sec respectively). 116

Figure 66. (a) and (b). TiN inclusions on the outer walls of the Directionally Solidified samples 18 and 19. 117

Figure 67. SEM picture of Niobium-carbides. 124

Figure 68. A typical carbonitride (TiN with an alumina core and surrounded by Nb carbide phase). 125

Figure 69. (a) Delta phase, (b) TiN inclusion precipitated on needle shaped delta phase (c) and (d) show TiN inclusion on Nb rich Laves phases. 126

Figure 70. Chromium rich deposit on the top of the ingot. 128

Figure 71. A TiN particle amidst chromium globules on the upper outer surface Of the DS cast ingot. 128

List Of Tables

Table 1. Composition of alloys SX-1 (From [5]), AM1, MAR-M200 [49] and SC-16. [6]. 13

Table 2. Prediction of undercooling of TiN and HfN in Ni-based superalloys. 23

Table 3. Saturation solubility of TiN in IN718 (from [62]). 32

Table 4. Relation between P_{N2} and [%N] for alloy IN718 (at T_{liq} = 1340 ^{0}C). 36

Table 5. Equilibrium nitrogen contents required for the formation of TiN particles above T_{liq} in alloy IN718. 37

Table 6. Effect of Ti segregation on the equilibrium nitrogen contents required for the formation of TiN below the T_{liq} in alloy IN718. 40

Table 7. Alloy compositions used in the experiments. 42

Table 8. Primary dendrite arm spacing of sample 1 and 2 as calculated from the SEM pictures. 53

Table 9. Average primary dendrite arm spacing at different portions of the DS sample 5 (64 ppm [N]). 54

Table 10. Velocity of rise (V_s) of TiN particles of various sizes. 56

Table 11. IN718 Samples used for different experiments. 58

Table 12. Nitrogen distribution along the DS cast ingots a). high temperature gradient b). low temperature gradient. 113

Table 13. Directional solidification experiments conducted under argon atmosphere. 115

Table 14. Effects of Hf addition on the equilibrium nitrogen content for HfN formation at T_{liq} (1340 °C) in alloy IN718. 120

Table 15. Relation between the equilibrium nitrogen contents required for the formation of TiN and P_{N2} for alloy CMSX-4 (at 1390^{0}C). 122

Table 16. Solubility of TiN in alloy CMSX-4 above T_{liq} (1390^{0}C). 122

List Of Symbols

A	Atomic mass (of the element)
CET	Columnar to equiaxed transition
C_0	Equilibrium solute concentration (wt%)
C_I	Composition of the solute element i (wt%)
C_s	Solid solute concentration (wt%)
C_l	Liquid solute concentration (wt%)
D	Diffusion coefficient (cm^2/sec)
DS	Directional solidification
DSQ	Directional solidification and quenching
d_s	Distance travelled by the secondary dendrite arm (cm)
d_p	length of the platform (of the turbine blade) (cm)
f	Activity coefficient (of the solute element)
f_s	Fraction solidified
I	Nucleation rate (/sec/cc)
G	Thermal gradient (°C/cm)
ΔG^o	Standard free energy (Joules)
ΔH^o	Enthalpy of formation (Joules)
k	Equilibrium partition coefficient
K	Equilibrium constant (for the reaction)
m_l	Liquidus slope of a solute element (°C/wt%)
N_o	Nucleation site density (/cc)
P_c	Solutal Pectal number

PDS	Primary dendrite arm spacing (μm)
R	Withdrawal rate (μm/sec)
ΔS^o	Standard Entropy of formation (Joules/°C)
SX	Single crystal
T_{liq}	Liquidus temperature (°C)
T_{sol}	Solidus temperature (°C)
ΔT	Undercooling (°C)
ΔT_s	Dendrite tip undercooling (°C)
ΔT_{nuc}	Undercooling for heterogeneous nucleation (°C)
TiN	Titanium nitride (precipitate)
V_s	Stokes' velocity of rise (for the TiN particle) (μm/sec)
Ψ	A parabolic function describing the transverse variation of temperature with distance.
ε	Wagner interaction parameter (for the element)
δ	percentage lattice mismatch between the substrate and the nucleant
ρ	Density of solid TiN particle (g/cm^3)
σ	Density of liquid IN718 alloy (g/cm^3)
η	Coefficient of viscosity (of liquid IN718 alloy) (Ns/m^2)

Acknowledgements

I would like to thank my supervisor, Dr. Alec Mitchell for his invaluable guidance throughout this work. I would also like to thank Dr. Steve Cockroft, Dr. Warren Poole, and Dr. Desmond Tromans for their useful discussions and suggestions. The help rendered by A. Schmalz in designing, and building of the experimental equipment is duly acknowledged. A special thanks to Philippe Auburtin, for all his help throughout this thesis. I am very thankful to Special Metals Corporation in providing help with the alloys used in this study. I am very grateful to my family for their encouragement and support. Finally, I am very thankful to Mani for making all this possible.

Chapter 1: Introduction

The demands for the operation of turbine engines at increased level of temperatures and reduced engine weight have been the principal contributing factor for the development of nickel base superalloy castings with enhanced mechanical properties. In spite of the improvements, the materials are still found to undergo premature failure at defects such as inclusions. It has been established that the low cycle fatigue crack (LCF) origins are primarily at the clusters of inclusions such as nitrides and only in very clean alloys is failure produced at the carbides or structural features such as grain boundaries [1], as illustrated in Figure 1. From the critical crack size versus inclusion size graph it can be seen that the agglomerate TiN is very detrimental to the mechanical properties. It is further known that the primary carbides and nitrides block the interdendritic fluid flow and thus have an effect on the formation of defects such as microporosity and freckles [2]. Among the non-metallic inclusions, the most important one is titanium nitride (TiN). It is found that the particles themselves not only detoriate the mechanical properties, but also influence the solidification structure [3]. Hence, it is important to know the thermodynamics of formation of nitride inclusions and the solubility of TiN in nickel base superalloys in order to predict under what conditions they may form. Chapter 2 of this report deals with this aspect.

An added problem in superalloys is that, they all have a long freezing range (solidus and liquidus temperatures) owing to their complex compositions. Therefore, they exhibit heavy segregation on solidification which has an influence on the nucleation conditions required for the CET (columnar to equiaxed transition). Random grain growth has been one of the major problems in the commercial casting of single crystal components for turbine engines. The reasons for the formation of random grains have been attributed to factors like discrepancy in

solidification due the complex geometry of the cast component, formation of freckle chains and nucleation etc.

It has been shown that the segregation created ahead of the solidifying dendrite tip and the undercooling in this region are contributing factors in the process of nucleation. It is to be noted that under normal industrial conditions of directional solidification in alloys, the undercooling mainly refers to the solutal undercooling and not the thermal undercooling. Solutal undercooling occurs due to the fact that as alloys solidify, they reject solute into the liquid at the interface. The accumulation of solute ahead of the interface effectively results in a region of supersaturation ahead of the dendrite tip. This supersaturation (or the related solute undercooling) represents the driving force for the diffusion of solute at the dendrite tip in an alloy. This undercooling is essential for heterogeneous nucleation to take place. A detailed study on the kinetics of nucleation and random grain formation in superalloys is presented in chapter 2 of this report.

However, in practice, secondary grains are found in many single crystal castings without any freckling or any drastic change in the thermal conditions. Hence, the source for the formation of secondary grains in single crystal castings is yet to be established. Though there is no strong evidence to substantiate it, there is a high probability that if the non-metallic inclusions like nitrides are rejected into the liquid immediately ahead of the liquidus isotherm during solidification, and if the heterogeneous nuclei are stable in this region, they are very attractive as nucleation sites. This may be an influential factor in random grain production in single crystal casting. Chapter 4 and 5 of this thesis present the theoretical and experimental studies on the problem stated above. The results and discussions are presented in chapter 6 and chapter 7 respectively, followed by conclusions with the recommendations for future work presented in the final chapter.

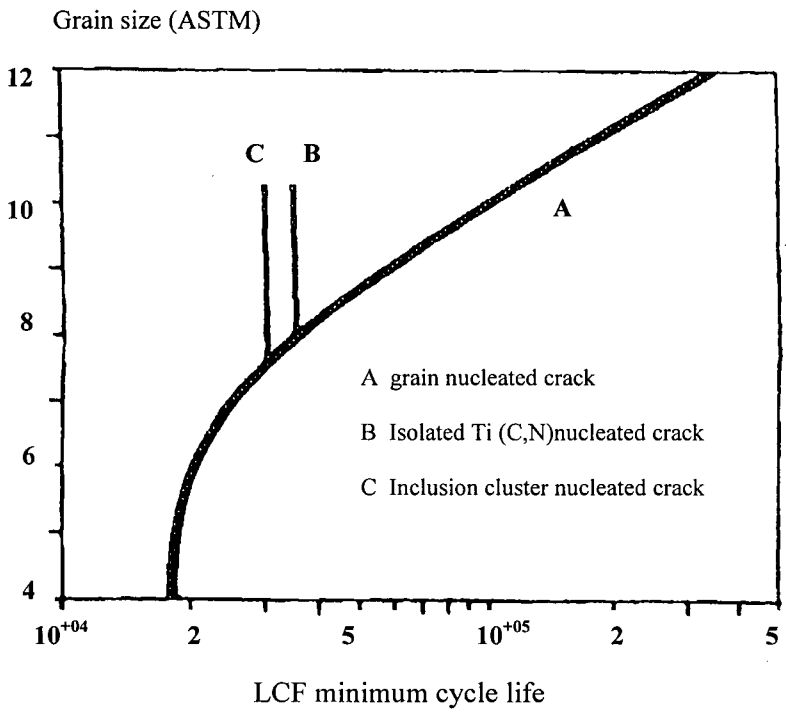

Figure 1. Fatigue properties of IN718, illustrating the influence of inclusions on premature failure at T = 350 °C; strain amplitude = 0.62% (from [1]).

Chapter 2 : Literature review

This chapter presents a literature review on the random grain formation and the nucleation aspects of inclusion formation in superalloys. An account of random grain formation through the columnar to equiaxed transition (CET) in superalloys, and the various explanations and contributing factors which have been attributed to the formation of random grains in superalloys in the past years is presented under the first sections of this chapter.

The absence of grain boundaries in the SX materials, and elimination of grain boundary strengthening elements like C, B, Zr allows higher temperature solution cycles and greater alloy microstructural homogeneity which improves alloy creep strength. SX/DS casting alloys are now extensively used for turbine blade materials (both aero and industrial turbine blades). In spite of the desirable mechanical properties, these materials are found to exhibit random grain formation during solidification. It is proposed in this thesis that the TiN inclusions may be a possible source for spurious nucleation in the SX/DS alloys. Since data for SX alloys such as a) the saturation solubility of TiN, and b) thermodynamic data pertaining to nitrogen solubility and TiN formation are not available, alloy IN718 was selected as a model system. Other reasons for selecting alloy IN718 are: a) it is a very common Ni-based superalloy, and b). studies on alloy IN718 have been done earlier, which are relevant to the present studies. Hence, it makes IN718 alloy a convenient model system.

Spurious grain formation in Ni- based superalloys, particularly the studies carried out by Pollock and Murphy [4,5] on the formation of equiaxed grains in single crystal superalloys and that carried out by Cockroft et. al [6] in the determination of a criterion for spurious grain formation in superalloy turbine blades, is described in Sections 2.2 and 2.3.

An account of the effects of inclusions in random grain formation in iron alloys and in

superalloys, and the theory of heterogeneous nucleation based on the Turnbull-Vonnegut [7] lattice disregistry model are presented in Section 2.4. Following this analysis, an account of the chemistry behind the solubility of nitrogen and the formation of TiN in Ni-based superalloys is discussed under Section 2.5. Sub-section 2.5.3 presents some earlier studies made on the formation of TiN inclusions in alloy IN718.

2.1 Random Grain Formation

Owing to their complex compositions, superalloys have a long freezing range. Therefore, they are subjected to heavy segregation on solidification and thus have an influence on the conditions required for the CET (columnar to equiaxed transition). It has been shown that the segregation ahead of the solidifying primary dendrite tip and the undercooling in this region contribute towards nucleation of equiaxed grains.

Though there is no strong evidence to substantiate it, there is a high probability that if the non-metallic inclusions like nitrides are rejected in the liquid immediately ahead of the liquidus isotherm during solidification, they would be very attractive as nucleation sites, which may be influential in random grain formation.

2.1.1 Fundamentals of CET

CET is a sudden change in the grain morphology of a casting from a columnar structure where the grains are oriented parallel to the direction of heat flow, to an equiaxed structure where the grains have a random orientation distribution. The CET phenomenon involves two processes: 1). formation of equiaxed grains, 2). growth of equiaxed grains and how they hinder the columnar grains. Addressing the first aspect, two main hypotheses have been put forward to explain the formation of equiaxed grains namely, 1). heterogeneous nucleation 2). dendritic fragmentation. The heterogeneous nucleation model has two invariants depending upon the method of casting.

In the case of conventional casting the mold is preheated to a temperature above the liquidus temperature of the alloy and the liquid alloy is directly poured into the crucible. The crucible is open at the bottom end which is in direct contact with a water cooled copper chill. According to the "big-bang" model [8], spurious nucleation occurs during the initial stages of solidification due to the drastic cooling of the liquid alloy when it comes into contact with the water cooled copper chill.

Alternatively, in the case of directional solidification or single crystal casting, where the mold is withdrawn through a temperature gradient at a specific withdrawal rate, nucleation can occur at anytime during solidification due to supercooling [9]. Studies by Fredriksson et. al [10,11] on lead and aluminum alloys and on steel ingots revealed that the CET at the vertical solidification front was caused by the development of free crystals. It was proposed that free crystals are formed in the liquid ahead of the solidification front, which is cooler than the liquid in the central part of the mould. When they multiply to large quantities, they physically adhere to the solidification front and thus hinder the growth of the columnar grains. According to this theory, higher the cooling rate of the mould, and lower the solidification process, easier was the CET.

Studies have revealed the occurrence of CET in experimental ingots depending upon the imposed conditions. For example, the presence of heterogeneous catalysts has caused nucleation during solidification [12]; equiaxed grains have been induced in ESR (electroslag remelted) iron alloys by addition of TiC [13] etc. However, in the case of larger conventional ingots, the most important process to cause the CET is likely to be the 'big bang' process.

The dendritic fragmentation model also has many invariants like the dendrite arm melt-off due to thermal effects such as convection [14]; or fragmentation due to mechanical damage [15]; or due to fall-out from the upper surface of the ingot [16].

Regarding the second aspect of CET namely the growth of equiaxed grains and how they hinder the growth of the columnar grains, much work has been done. It was established by

Doherty et. al., [17] that in order to grow, the latent heat of the growing nuclei should be conducted out to the ingot mold, past the tips of the columnar dendrites. Therefore, the equiaxed grains must grow at a higher temperature than the columnar grains. Witzke et. al., [18] derived the thermal and chemical fields ahead of the growing tips of the columnar dendrites from theories of natural convection and have suggested two necessary conditions for the growth of equiaxed grains: 1). the intensity of constitutional undercooling, and 2). The volume of the undercooled liquid both must reach a sufficient value. This aspect of undercooling occurring ahead of the growing dendrites is discussed in detail in the following sub-section.

2.1.1.1 Dendrite Undercooling

Two different types of dendrite undercooling have been identified. One occurs with dendrite growth into an imposed temperature gradient, where the undercooling increases for faster dendritic growth (cellular or constrained dendritic growth) [19,20]. The situation for the columnar or directional solidification is often referred to as constrained growth, where the rate of advance of the isotherms constrains the dendrites to grow at a given velocity. The second where the dendrite growth occurs with no temperature gradient in which, the undercooling increases as the dendrites grow faster [21-23]. The role of temperature in gradient causing this difference was suggested by Doherty et. al., [22] and was verified experimentally and theoretically by Burden and Hunt [19].

The phenomenon of dendrite tip growth has been extensively studied for binary alloys [24-27]. Coates et. al [27] have mathematically extended (with some modifications) this to ternary and multiconstituent alloys and have shown that each solute element makes an individual contribution towards the constitutional supercooling of the interface. Bobadilla [28] and Rappaz et al. [29] have modified the KGT [30] model and have shown that the individual undercoolings

of each solute element 'i' may be summed to determine the overall undercooling of the dendrite tip as:

$$\Delta T_c = \sum_i \Delta T_{c,i} = \sum_i \frac{m_l . C_{o,i}}{1-(1-k_i).I(P_{c,i})} \quad (1)$$

where,

m_l = slope of the liquidus

C_0 = equilibrium composition

C_i = composition of solute element i

k_i = distribution coefficient for the element i

I(Pc) = Ω = Ivanstov function of the solutal Pectal number Pc, given by: [31]

$$P_c = \frac{R\rho}{2D_l} \quad (2)$$

where,

R = rate of advance of the dendrite tip

ρ = radius of the tip

D_l = liquid diffusion coefficient

Equation (1) was further simplified by assuming that the liquid diffusion coefficients for each element are equal , which implies that the Pectal numbers and supersaturations associated with the solutes are equal. Hence, the equation reduces to the expression 3 from which the dendrite tip undercooling for a multiconstituent alloy can be calculated if the growth rate is known.

$$\Delta T = \Omega . \sum_i m_i . C^*_{l,i} . (1-k_i) = \Omega . \overline{mc} . (1-\bar{k}) \quad (3)$$

for which, the "pseudo-binary" variables $\overline{C}$, $\overline{m}$, and $\overline{k}$ are given by:

$$\overline{C} = \sum_i C^*_{i,l} \tag{4}$$

$$\overline{m} = \frac{\sum_i m_i . C^*_{i,l}}{\overline{c}} \tag{5}$$

and

$$\overline{k} = \frac{\sum_i m_i . C^*_{i,l} . k_i}{\overline{m} . \overline{c}} \tag{6}$$

Therefore, it can be inferred from equation 1, 2 and 3 that the rate of solidification plays an important role in determining the undercooling of the dendrite tips.

2.2 Spurious Grain Formation In Ni-Based Superalloys

Random grains or spurious grains have been observed in single crystal and directionally solidified turbine blade castings, which severely detoriate the mechanical properties. The source for heterogeneous nucleation and undercooling are the primary factors causing CET and spurious grain formation in Ni-based superalloy castings. Many models have been put forward to explain the phenomenon of breakdown of columnar structure and the formation of equiaxed grains in Ni-based superalloys. These theories have considered either of the two views for grain nucleation namely, a). Thermosolutal convection, and b). Constitutional undercooling, which are discussed in the following sub-sections.

2.2.1 Thermosolutal Convection

Pollock and Murphy [4,5] have studied grain defect formation in a number of superalloys and their observations have suggested that in high refractory content superalloys, the breakdown of

single crystal solidification and the formation of mis-oriented grains and defects such as freckles are dependent on thermosolutal convection processes. It was found that the transition from single crystal to equiaxed grain structure occurred gradually for a fixed alloy composition and withdrawal rate. As the thermal gradients were decreased, isolated and highly mis-oriented columnar grains appeared until the advance of the single crystal front was completely blocked. A major factor that affected this transition was the primary dendrite arm spacing (PDS). Figure 2 shows the number of grains observed as a function of primary dendrite arm spacing for each of the experiments.

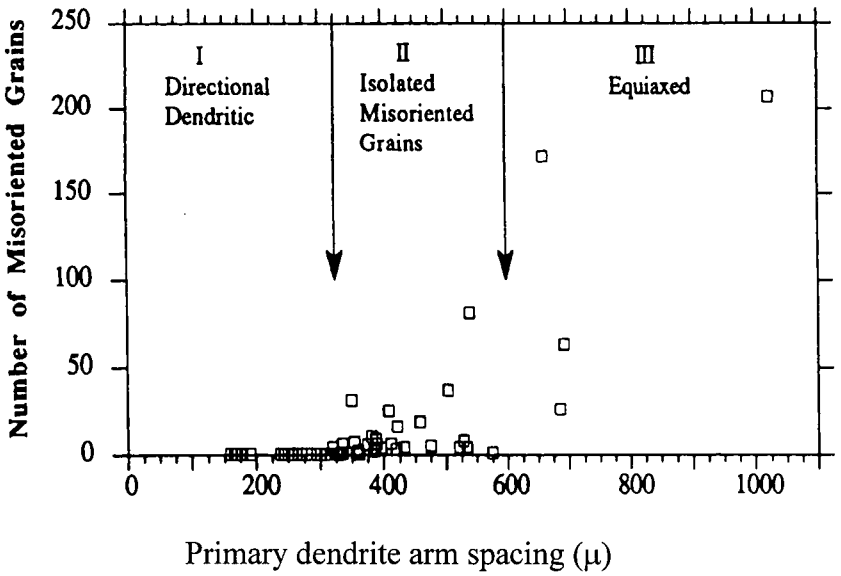

Figure 2. The three regimes of grain defect formation and the dependence on dendrite arm spacing. (from [5]).

It can be seen from Figure 2 that on the basis of the primary dendrite arm spacing, three regimes of behavior can be identified. 1). Region of single crystal solidification for PDS < 320 μm 2). Region of solidification interrupted by occasional nucleation resulting in the formation of mis-oriented columnar grains for a PDS between 320-600 μm and 3). Region of equiaxed

solidification with complete blockage of the solidification front beyond a PDS value of 600 μm. CET was generally observed to occur in the third regime.

Nucleation and growth of isolated columnar grains and freckles occurred in the intermediate range. An example of a mis-oriented isolated columnar grain is presented in Figure 3. A systematic study on these defects has revealed that the nucleation on inclusions in the melt cannot be attributed to the formation of these defects, but occasional internal grains with no surface connections were observed.

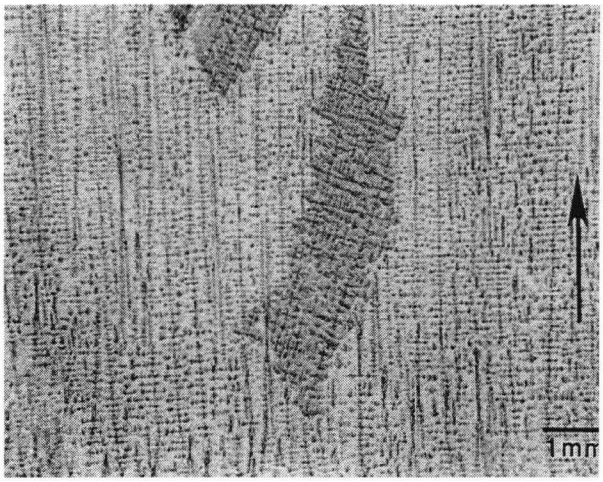

Figure 3. Isolated mis-oriented columnar grains during directional solidification of alloy SX-1 (after [5]).

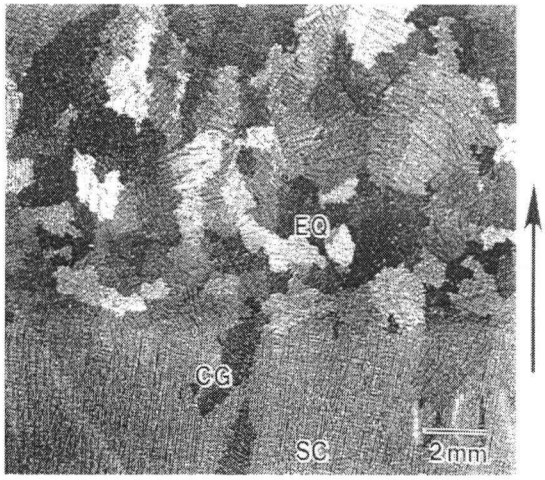

Figure 4. Complete breakdown of single solidification and blockage of solidification Front by equiaxed grains. (after [6]).

In experiments where the thermal gradients were decreased below 15 °C/cm, there was a transition from single crystal to equiaxed grains. Figure 4 presents such a transition from the airfoil region to the base of the turbine blade. The complete breakdown of the single crystal solidification has occurred here.

In addition to the formation of columnar and equiaxed grains, freckle type defects have also been identified. Figure 5 shows an example of a freckle chain. These are observed in the

low-gradient regime. During the unidirectional solidification of the alloys, due to solute rejection there is density inversion developed in the interdendritic liquid, resulting in convective flow and formation of solute-rich channels.

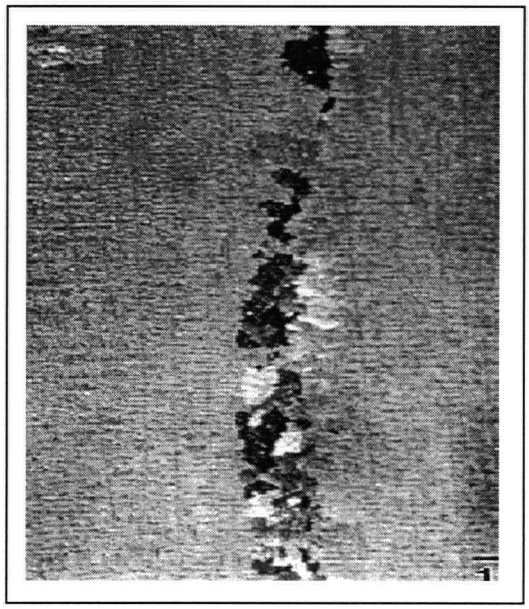

Figure 5. A typical freckle chain observed during solidification of alloy SX-1. (from [6]).

Pollock [5] has observed that the elements which influenced defect formation to the greatest extent were refractory elements like Re, W, and Ta, which are high density elements (they have densities about two times that of nickel in the solid state) as well as more strongly partitioning elements. It was also observed that freckles were rich in elements that have a partition coefficient < 1. While elements like Al ($k=0.98$) and Ta ($k=0.53$) segregated to the interdendritic liquid, there was a strong depletion of elements with partition coefficients > 1 like Re ($k=1.65$) and W ($k=1.37$) relative to the base material from the freckled regions. Figure 6 shows the relation between the number of freckled chains and the primary dendrite arm spacing. For alloy SX-1, the onset of freckles (as shown in Figure 6) was observed at the same primary dendrite arm spacing

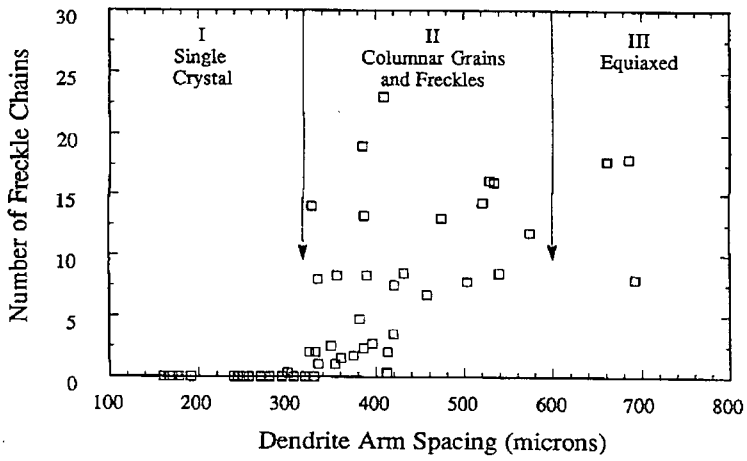

Figure 6. The dependence of freckle chain formation on primary dendrite arm spacing. (after [6]).

Alloy / elememts	SX-1 wt%	AM1 wt %	MAR – M200 wt %	SC-16 wt %
Ni	Bal.	Bal.	Bal.	Bal
Cr	4.5	7.52	8.4	16
Co	12.5	6.64	9.52	-
Mo	-	2.06	0.03	3
Al	6	5.34	4.98	3.5
Ti	-	1.25	1.92	3.5
W	5.8	5.59	11.9	-
Ta	7	7.8	0.10	3.5
Nb	-	0.01	0.86	-
Hf	0.16	0.004	1.18	-
Re	6.3	-	-	-
C	-	80 ppm	0.14	-
B	-	3 ppm	150 ppm	-
Zr	-	10 ppm	400 ppm	-

Table 1. Composition of alloys SX-1 (From [5]), AM1, MAR-M200 (from [49]) and SC-16 (from [6]).

where columnar grains began to nucleate [as shown in Figure 2]. The general composition of alloy SX-1 is given in Table 1. Since the columnar grain nucleation and freckles were found to occur under similar thermal and solutal conditions, it was proposed that convection and dendritic fragmentation contribute to the nucleation of columnar grains and freckle type defects, and ultimately to the formation of random or equiaxed grains. This is not substantiated by the model configuration of remelting times for fragments by Erdeljac et al [32]. According to their model, larger dendrite-like particles (> 1.6 mm) would not melt completely and would be entrapped in the mushy zone.

2.2.2 Constitutional Undercooling

The best-suited model to apply to Ni-based superalloys is the Hunt's [33] model for steady-state analysis of columnar and equiaxed growth. According to this model heterogeneous nucleation in the constitutionally undercooled liquid at the columnar front is the only source for equiaxed grains. CET will occur once the volume fraction of the equiaxed grains ahead of the columnar dendrites reaches a value of 0.49. The critical thermal gradient in the liquid ahead of the columnar dendrites, below which a CET will occur, is given by:

$$G < 0.617\, N_0\, 1/3 \left[1 - \frac{(\Delta T_N)^3}{(\Delta T_c)^3}\right] \Delta T_c \qquad (7)$$

Where,

G = critical thermal gradient at the liquid/solid interface below which CET occurs

N_o = nucleation site density

ΔT_c = columnar dendrite tip undercooling

ΔT_N = heterogeneous nucleation undercooling at which 1 site/cc becomes active

Since the solidification rate (R) is incorporated in the equation 7 for undercooling (ΔT_c), both the factors G and R affect the CET phenomenon. The cooling rate (G x R) during the solidification determines the amount of time that the equiaxed grains have to grow before the arrival of the columnar front. If the equiaxed grains have not grown to a full volume fraction of 0.49, CET will not occur. Therefore, CET is favored by high solidification rate, which maximize the solidification front undercooling. The role of the thermal gradient is to provide a finite volume of constitutionally undercooled liquid ahead of the interface in which active nucleation sites may be found. Therefore, CET is favored by low thermal gradients that maximize the volume of the undercooled liquid.

2.3 Criterion For Spurious Grain Nucleation

The formation of spurious grains was investigated by Cockroft et. al [6] in Ni-based superalloy turbine blades of CMSX-4 using a modified Hunt's model for CET in Al-Cu alloys. A general mathematical model was developed to avoid spurious nucleation in the body of the blade and the extremities of the head and the root. This was done by determining the limiting conditions for the solidification rate 'R' and the axial temperature gradient 'G', which are the most important solidification parameters in a SX or DS casting process.

It has been established that the probability of nucleation of equiaxed grains depends upon the dendrite tip undercooling, which can be calculated for binary alloys using the KGT model. Since superalloys are complex multi-component systems, the KGT model was extended, as suggested by Bobadilla [28] and Rappaz [29] and the pseudo-binary values were calculated using equations 3 to 6. The density of equiaxed grains (dn) at a given undercooling d(ΔT) was calculated using a continuous nucleation distribution of the form of a Gaussian distribution, originally proposed by Rappaz [34]. This is given by:

$$n(\Delta T) = \int \frac{n_{max}}{\sqrt{2\pi}.\Delta T_\sigma} \exp\left[-\frac{1}{2}\left(\frac{\Delta T - \Delta\overline{T}}{\Delta T_\sigma}\right)^2\right] d(\Delta T) \tag{8}$$

where, n_{max} , is the total number of nucleation sites available (2.5 x 10^8 m^{-3}), $\Delta\overline{T}$ and ΔT_σ (1.5 °C) are the distribution parameters at the center and the standard deviation respectively. Using these values for alloy CMSX-4, the value of $\Delta\overline{T}$ was found to be 6.7 °C. It was found that CET can occur if the volume fraction of equiaxed grains ahead of the columnar dendrite front exceeded a critical value of 0.66. This value was employed to study the spurious grain formation in the body of the turbine blades.

When a columnar dendritic front (which is also the curvature of the liquidus isotherm) passes through extreme enlargements in cross-sections of the component (for e.g. transition from the blade to the outer shroud), depending upon the undercooling occurring during the process two phenomenon can occur [35], as illustrated in Figure 7.

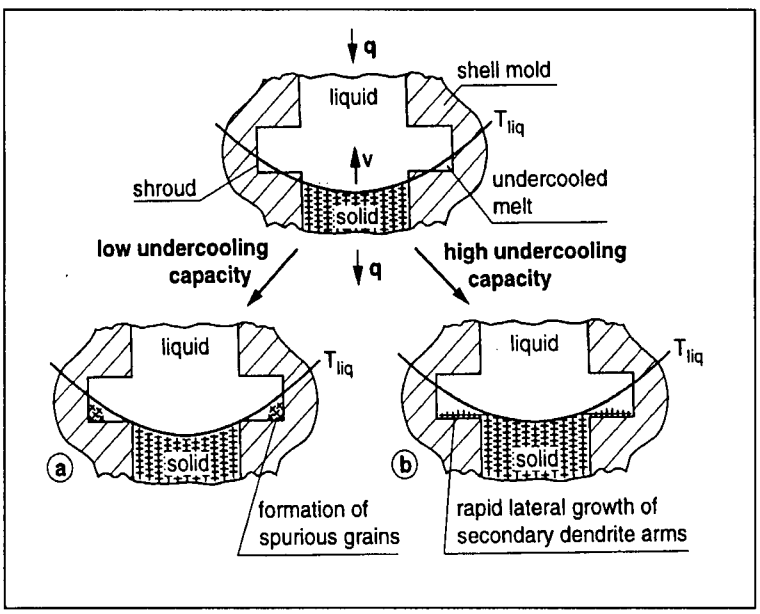

Figure 7. Depending upon the undercooling capacity of the given alloy a macroscopic concave curvature of the liquidus isotherm can cause the formation of stray grains (a) or result in fast lateral growth of secondary dendrites (b). (from [35]).

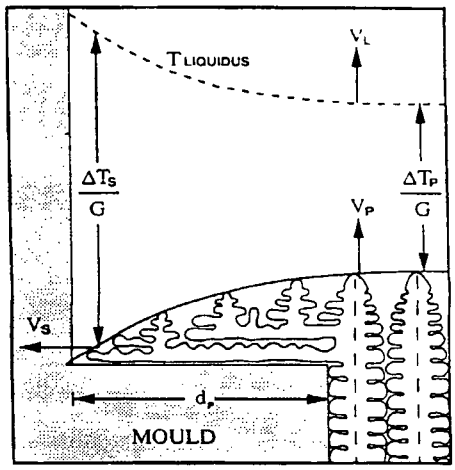

Figure 8. Schematic diagram showing the growth of a secondary dendrite arm into a platform in the presence of a transverse temperature gradient. (from[6]).

1). A concave liquidus isotherm can result in isolated, thermally undercooled regions of the melt. Depending upon the number of nuclei available in the melt and the extent of undercooling in this region heterogeneous nucleation and the formation of spurious grains can occur close to or at the ceramic mold as showed in Figure 7(a).

2). If nucleation is suppressed, secondary dendrites will grow rapidly laterally towards the far corners of the shroud, as soon as the primary dendrites reach the shroud. This is schematically represented in Figure 7(b).

The secondary dendrite arm must grow up to the new lateral surface of the mold in order to propagate the single crystal in these open regions of the liquid by tertiary branching mechanism, as represented in Figure 8[6]. Once inside this region and unconstrained by neighboring solute fields, the tertiary arms can break free to become new primary dendrites. The rate at which the secondary dendrites grow into the cavity is finite and is a function of the

undercooling of the liquid immediately ahead of the dendrite tip. At appropriate conditions, the undercooling adjacent to the mold wall at the extremity of the cavity may increase to such a point when the heterogeneous site would become active prior to the arrival of the secondary dendrite arm. This results in the formation of "stray crystals" [36-38].

Conditions under which spurious grains can form in the turbine blade platform were derived based on assessing whether the secondary arm was able to traverse the length dp of the platform, before the dendrite tip undercooling ΔT_s exceeded the critical undercooling for heterogeneous nucleation ΔT_{nuc} [6].

The condition for the formation of spurious grains is given by:

$$\Delta T_s \geq \Delta T_{nuc} \quad \text{at ds = dp} \tag{9}$$

and the condition under which spurious grains will not form is given by:

$$\Delta T_s \leq \Delta T_{nuc} \quad \text{at ds = dp} \tag{10}$$

where, ds is the distance traveled by the secondary dendrite arm.

The undercooling at the tip of the secondary arm is given by:

$$\Delta T_s = V.G.t + \Psi(d_s) \tag{11}$$

where, V is the mold withdrawal velocity, G is the axial temperature gradient, t is the time, and Ψ is some function describing the transverse variation in temperature with distance. The distance traveled by the secondary arm is given by:

$$ds(t) = \int_0^t v_s dt \tag{12}$$

where, v_s is the growth velocity of the secondary dendrites. The effect of transverse temperature gradient on the limiting conditions for G and V for spurious grain nucleation in the platform have been studied by varying the temperature gradient G [6]. The parabolic function to describe the relation between the distance traveled by the secondary dendrite arm (d_s) and the temperature is given by:

$$\Psi(d_s) = T_{max} - \sqrt{\frac{(d_p + d_m - d_s)}{(d_p + d_m)}} T_{max} \tag{13}$$

where, T_{max} is the maximum temperature difference between the center of the blade and outside of the mold wall at the extremity of the platform, dp is the platform length, and dm is the thickness of the mould.

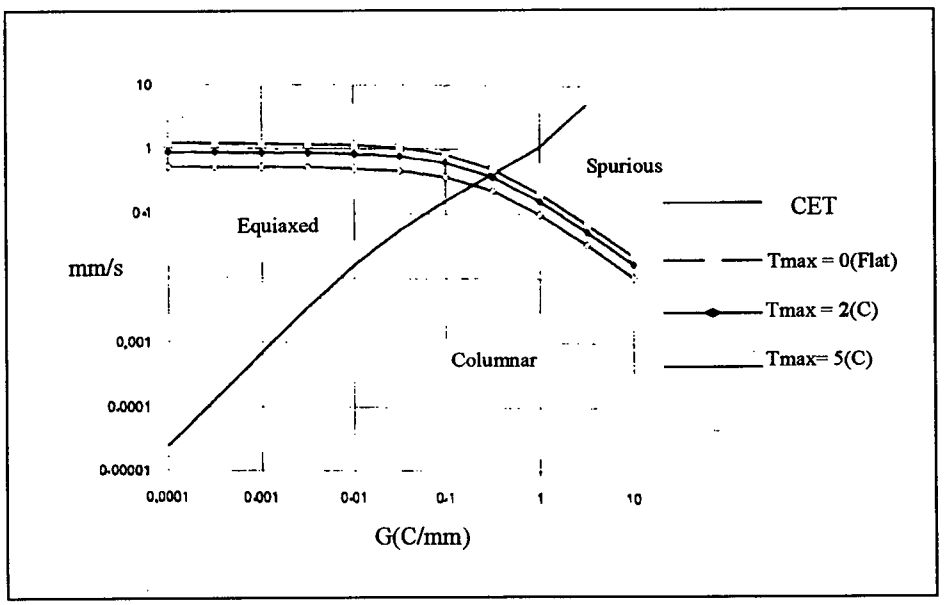

Figure 9. Effect of transverse temperature gradient in alloy CMSX-4. (from [6]).

The results are presented in Figure 9, which indicate that in the platform-limited region, the limiting conditions for V are decreased as the transverse temperature gradient G is increased. This brings out the need for minimizing the extent to which the extremities of the platform are cooler than the body of the blade. Hence, it would be beneficial to keep the extremities of the platform hotter than the body of the blade. This could be achieved by slowing the rate of withdrawal V and the rate at which the radiation shield is opened at the platforms if it could be determined, on-line, exactly when to make the change.

2.4 Inclusions and Random Grain Formation

Investigations of superalloys using the EB button melting technique have showed the presence of oxides and nitrides [39] and also the presence of TiN in high temperatures in liquid superalloys [40,41]. Eliminating the source responsible for the production of equiaxed grains in liquid superalloys would also eliminate the production of spurious grains.

Studies on revert alloys have attributed the presence of high [N] to be the source for equiaxed grains [42] and also TiN particles were found in revert alloys. Painter et al. [43] found CrN and TiN to be efficient grain refiners in equiaxed castings. Studies on IN738 by Liu et. al. [44] have revealed that additions of B, NiAl, and NbC favored CET by increasing the size of the equiaxed zone and decreasing the grain size. Pardo [45] found CET to occur in ferritic stainless steel GTA welds only in the presence of TiN particles, which were also found to be effective nucleating agents at an undercooling of 1.7 ^{o}C by Bramfitt [46]. Recently, The effectiveness of TiN as an inoculant for ferritic, and ferrite/austenite stainless steels was studied by Poole et. al [47]. Their studies have revealed that TiN is an effective nucleant for ferritic stainless steels, which have been slowly directionally solidified, but is not an effective inoculant for austenitic stainless steels. This is because, the lattice mismatch between TiN, which has an FCC crystal structure, and ferritic matrix (2.9315 A^{o}) is less when compared to the lattice mismatch between

TiN and the austenitic matrix (3.6773 A^{o}). Hence the presence of TiN induces heterogeneous nucleation in ferritic stainless steel. The concept of lattice disregistry and heterogeneous nucleation is explained in detail below.

The Turnbull–Vonnegut model [7] has emphasized the contribution of the crystallographic lattice disregistry between the substrate and the nucleated solid towards heterogeneous nucleation. This model was valid up to a disregistry of 20% (a value above this implies poor coherency between the two phases), and only for substrates and nucleating solid having similar crystal structures. The degree of supercooling of a liquid was postulated to be a parabolic function of the disregistry factor. The expression for undercooling is given by:

$$\Delta T_c = 0.556\left(\frac{\delta^2}{8}\right) \tag{14}$$

where,

ΔT_c = undercooling

δ = percent lattice disregistry given by:

$$\delta = \frac{\Delta a_o}{a_o} \text{ x } 100 \text{ \%} \tag{15}$$

where a_0 is the lattice parameter of the solid inclusion, and Δa_0 is the difference in the lattice parameter between the substrate and the solid inclusion. It is to be noted that the undercoolings thus calculated give an approximate idea as to whether the inclusions can act as effective heterogeneous nucleation sites in the substrate. Bramfit [46] extended this linear disregistry theory to describe similar as well as dissimilar lattice arrangements between the substrate and the nucleating phase. Bramfit [46] and Ohashi [48] have determined the undercoolings before

nucleation on a number of nitrides, carbides and oxides in δ-iron, as presented in Figure 10. It is evident from the Figure that TiN is one of the most effective nucleants in delta iron.

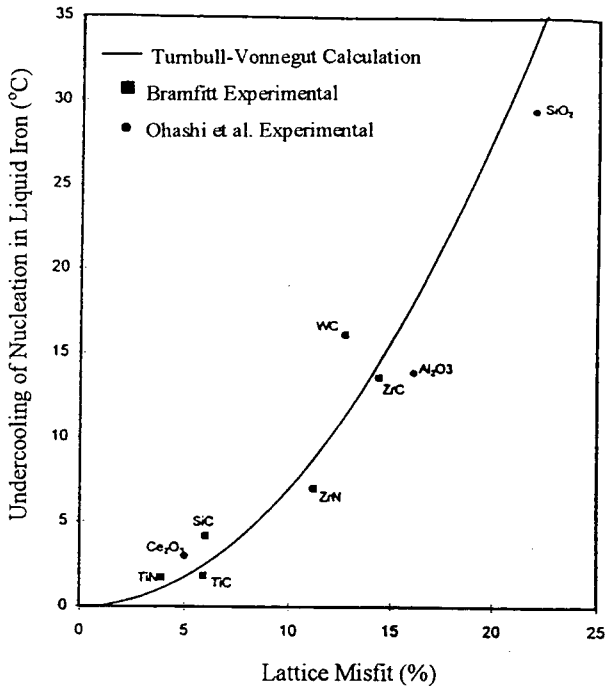

Figure 10. Lattice mis-match vs. nucleation undercooling in delta iron of various oxides, nitrides and carbides (from [5]).

Experiments conducted by Fernihough [49] on Ni-based superalloys confirm that heterogeneous nucleation in the region of undercooled liquid ahead of the dendritic tip, due to solute rejection, is the source for equiaxed grain formation. The appearance of spurious grains in the platform of turbine blades can be explained on the basis of whether sufficient volume of undercooled liquid is present and also to the extent of undercooling. The contribution of lattice disregistry towards undercooling can be extended to Ni-based superalloys. Taking into account the lattice expansion at the liquidus temperatures, we can calculate the undercooling required for nucleation on TiN and HfN (which are the stable nitride found in single crystal alloys) in Ni-based superalloys. The values are presented in Table 2.

inclusion	Lattice parameter at 1340 °C (a_o) A°	% lattice mismatch (with matrix in Ni-based superalloys)	Undercooling (°C) $\Delta T_c = 0.556\left(\frac{\delta^2}{8}\right)$
TiN	4.303	16.7	19
HfN	4.593	21.8	33

Table 2. Prediction of undercooling of TiN and HfN in Ni-based superalloys.

Since TiN and NbC have a similar crystal structure (both are cubic) and the lattice parameters are very similar, they can dissolve in one another i.e. they are isomorphous. The observed carbonitrides in IN718 alloys are (Nb, Ti) (C,N). However, in single crystal superalloys for turbine blades containing Hf, the stable carbonitride phase would to be (Hf,Ti) (C,N). The Hf/Ti ratio may vary between 0.3 – 0.4 in the nitride core, and between 12-19 in the outer carbide phase. As discussed before, for heterogeneous nucleation to occur, there should be a good lattice fit between the nucleant atom and the matrix atoms. In Ni-based alloys, the precipitated phases invariably have a cubic structure, which has a good lattice fit with the FCC matrix. TiN and HfN have an FCC structure, but the mismatch in the lattice parameter between HfN and the Ni matrix is much larger (21.7%) when compared to the mismatch between TiN and the Ni matrix (16.8%). Consequently, the undercooling required for nucleation on HfN (calculated using equation 14) is large. This indicates that TiN is a more effective nucleant. In casting single crystal superalloy turbine blades, as the mold is withdrawn into the cold zone, the platforms are observed to supercool by several degrees before the arrival of the dendrites from the main body of the blade. Hence, the contribution of the dendrite arms towards the formation of equiaxed grains can be ruled out. Studies by Fernihough [49] on alloys AM1 and MAR-M200 have revealed an

undercooling of about 3.5 to 3.8 °C at a withdrawal rate of about 5.8 x 10^{-3} mm/min. On the other hand, studies by Meyer et. al [35] on turbine blades of SC-16 (composition is given in Table 1) have revealed an undercooling of about 10 K in the leading edge and an undercooling of about 12K in the trailing edge of the blade which also lead to the formation of spurious grains in these regions. Also, the withdrawal rate was found to affect the undercooling produced. By using a withdrawal rate of 3 mm/min, undercoolings of up to 40K were measured in the outer regions of the shroud. Also, a withdrawal rate of 2 mm/min was found to decrease the undercooling in the shroud area up to 2 K. It is to be noted that in these studies the withdrawal rates used are much higher than the withdrawal rates used in practice for turbine blade casting (< about 1 mm/min), which places a practical limitation on these manipulations. Figure 11 presents the cooling curves measured in the trailing edge at different withdrawal velocities. It can be seen that raising the velocity causes an increase of the cooling rate and of the extent of undercooling.

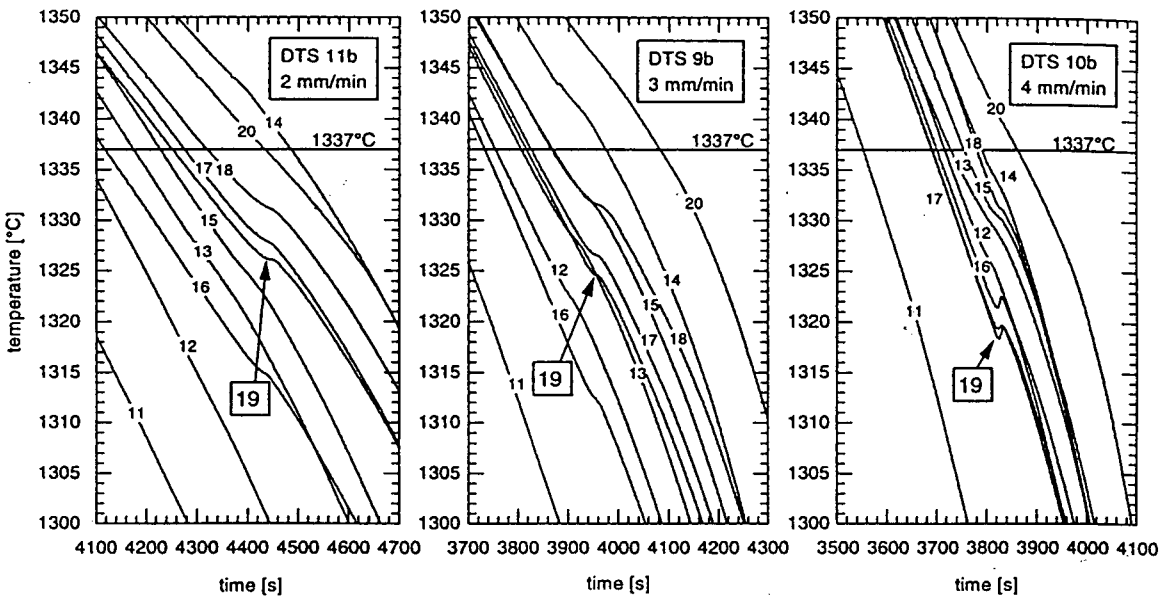

Figure 11. Cooling curves measured at different withdrawal rates [35].

Comparing the calculated values for undercooling of TiN and HfN in Ni-based superalloys with the undercoolings produced during the directional solidification of single crystal turbine blades [38], compels the idea that the source for spurious grain formation may be a foreign substrate like a TiN inclusion. The following sections deal with the thermochemistry behind the dissolution of nitrogen and the formation of TiN in nickel based superalloys.

2.5 Thermodynamics Of Inclusion Formation

2.5.1 Nitrogen in Superalloys

Studies on revert superalloys have attributed the presence of microporosity and detoriation in mechanical properties to an increase in nitrogen content [50-53]. R.E Painter et. al. [51] considered that microporosity was not a function of the total nitrogen content, but the form in which the nitrogen was present in the superalloy. The nitrogen content of an alloy comes from the impurity levels of the raw material and contamination during the melting and casting processes. For a specific commercial application, the appropriate nitrogen content is specified in superalloys. Alloy IN718, which finds general application as forged rotating parts, has a specified nitrogen content of 60ppm - 80ppm. The casting alloys, when used for critical application have a lower value of nitrogen content ranging from 15ppm to 25ppm and when used for less stressed parts have a nitrogen content of 40ppm - 80ppm [1]. The reason for this difference is attributed to the formation of casting defects associated in alloys with high nitrogen contents. In the case of single crystal alloys, due to the higher titanium content the solubility of titanium nitride is lower in these alloys.

2.5.1.1 Solubility of Nitrogen

The solubility of nitrogen in iron, iron-nickel alloys [54-59, 40] and in multicomponent nickel-based alloys [60] is reported in the literature. On the basis of statistical theory for the lattice

model of solutions a formula was derived for the solubility of nitrogen in alloys of iron and nickel, with other transition metals. This is given by:

$$[\%N] = [\%N]_{Me} \frac{A_{Me}}{A_M}\left(1-\frac{1}{6}\sum_{j=3}^{n}\varepsilon_N^j x_j\right)^6 \quad (16)$$

Where, [%N] and $[\%N]_{Me}$ are the solubility of nitrogen (in mass fractions) at P_{N2} = 1 atm, and the temperature 1600 °C in an alloy M, and in a pure metallic solvent Me, respectively. x_j is the mole fraction of the j-th component in the alloy; ε_N^j is the Wagner interaction parameter of nitrogen with the j-th component in the solvent Me; n is the number of components in the alloy; $A_M = A_{Me}X_{Me} + \sum A_j x_j$, where Aj is the atomic mass of the j-th component. Using this method, the possibility of calculating the solubility of nitrogen in nickel-based alloys using only the first-order interaction parameters was shown by Bol'shov et al. [60].

Studies have shown that Sievert's law holds for molten, pure iron over modest nitrogen pressures (<10 MPa) and for all titanium bearing alloys up to a nitrogen partial pressure below 1 atm. [40,61]. The dissolution of nitrogen in liquid iron alloy can be written as:

$$\frac{1}{2}N_2(g) = [N] \text{ (1 wt\% in liquid iron)} \quad (17)$$

$$k = \frac{f_n[N]}{P_{N_2}^{1/2}} \quad (18)$$

where, k is the equilibrium constant for equation 17 and f_N is the activity coefficient of nitrogen in 1 wt% standard state iron. The activity coefficient of nitrogen can be calculated using the known thermodynamics and the following relationship:

$$\log f_N = \sum_i e_N^i [\%i] \quad (19)$$

Where, e_N^i is the first order interaction coefficient between nitrogen and element i. The standard free energy for the reaction 17 is given by:

$$\Delta G^\circ = \Delta H^\circ - T\Delta S^\circ = -RT \ln k \quad (20)$$

where, ΔH° and ΔS° represent the standard heat and entropy of nitrogen solution at temperature T. The above equations 17-20 can be applied for nickel-based alloys, assuming a similar behavior, and hence the solubility of nitrogen in Ni-based superalloys can be calculated.

2.5.2 Chemistry of TiN Precipitation

It is found that in nickel-based alloys containing niobium, the precipitated nitrides are pure titanium nitrides and do not contain any detectable Nb or carbon [1]. Nitrides other than TiN have not been reported in alloys containing Nb. The reaction between Ti and N is fully determined for alloys that contain over 0.2 wt% Ti. The reaction for the formation of TiN for iron alloys can be applied to Ni-based superalloys and can be written as:

$$TiN_{(s)} = [Ti]_{(l)} + [N]_{(l)} \quad (21)$$

The Gibbs Standard free energy for the above reaction is given by:

$$\Delta G^\circ = -RT \ln (K_{sp}) \quad (22)$$

where, K_{sp} is the solubility product of TiN in a superalloy which is defined as:

$$K_{sp} = [\text{Ti wt\%} \times f_{Ti}] [\text{N wt\%} \times f_N] \quad (23)$$

Where, fi is the activity coefficient of component i.

The activity coefficient of Ti is given by the expression :

$$\log f_{Ti} = \sum_i e_{Ti}^i [\%i] \quad (24)$$

where, e_{Ti}^i The first order coefficient of Ti and the element i.

For practical convenience, Cockroft et. al [62] have incorporated the product of the activity coefficients in the solubility constant and hence re-defined reaction 23 as:

$$K'_{sp} = [\text{Ti wt\%}] [\text{N wt\%}] \quad (25)$$

It is evident that equation 21 is temperature controlled such that the equilibrium shifts to the right with increasing temperature as shown in Figure 12. It is also composition dependent, being controlled by the activity coefficients and contents of Ti and N, and hence being a function of segregation during freezing.

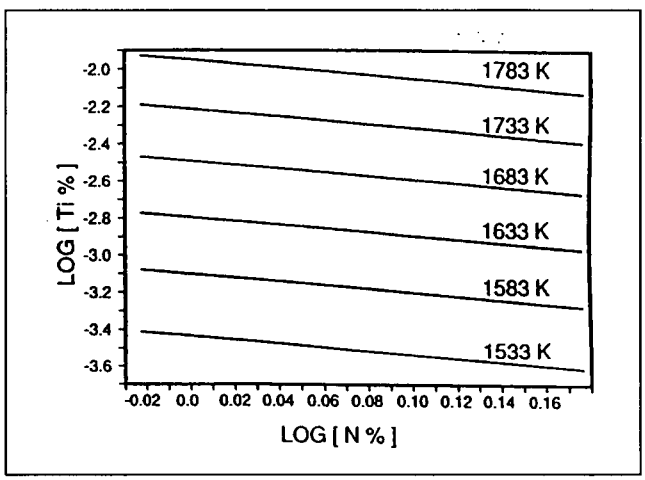

Figure 12. Temperature and solubility dependence of the saturation solubility of TiN. [from 62]

2.5.3 Studies in alloy IN718

The solubility of N and TiN in nickel-based alloy IN718 by equilibration methods has been extensively studied [1, 62-64]. The solubility of nitrogen homogenized to the liquidus temperature of alloy IN718 presented given in Figure 13. It can be seen that the solubility of N increases with an increase in superheat.

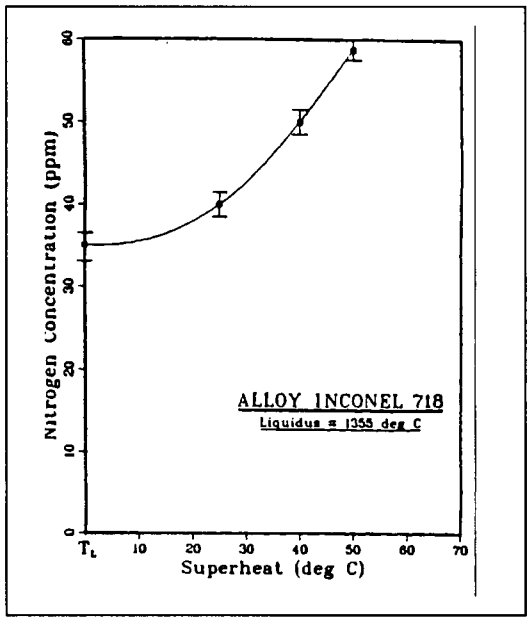

Figure 13. Nitrogen solubility in alloy IN718. (from [63]).

An increase in nitrogen content in the liquid alloy results in the precipitation of large numbers of TiN particles at the liquidus temperature in alloys like IN718, which have low titanium levels. Also, the nitrogen content in the alloy is directly found to affect the precipitated TiN particle size. Figure 14 gives the relationship between the size distribution of agglomerated and individual TiN inclusions and the nitrogen content in alloy IN718, with a constant local solidification time. It can be seen that as the nitrogen content increases, the nitride inclusion size also increases.

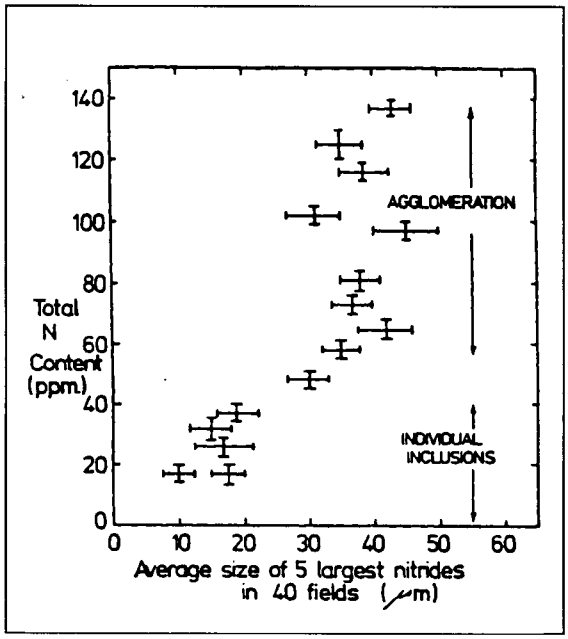

Figure 14. Size distribution of TiN inclusions as a function of nitrogen content in alloy IN718, with a constant LST. (from [63]).

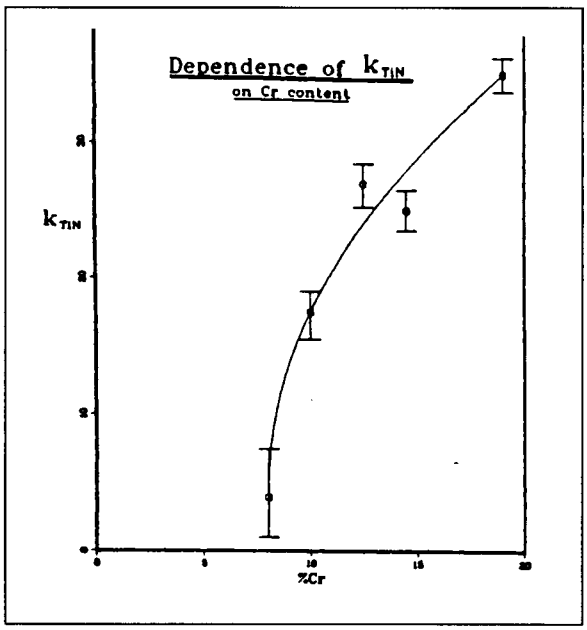

Figure 15. Dependence of k_{TiN} on Cr content in some superalloys (from [63]).

It has been shown that the saturation solubility of TiN is not only a function of the Ti and N content, but can also be affected by Cr content. Figure 15 presents the relation between solubility of TiN and Cr content for various nickel-based alloys. The solubility of TiN is found to increase with Cr content.

As mentioned earlier, the solubility of TiN is a strong function of temperature. This is presented in Figure 16. It can be seen from Figure 16 that the solubility in the interdendritic regions (II) is less than that of the bulk alloy (I). This is due to the segregation of titanium and nitrogen in the interdendritic region (this is discussed in detail under section 4.2).

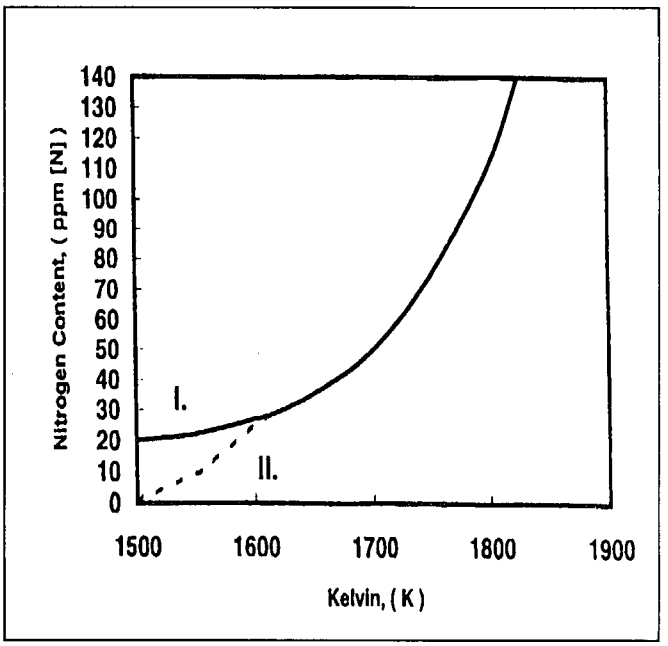

Figure 16. Temperature dependence of the saturation solubility of TiN in IN718 (from [1]).

Table 3 presents the saturation solubility relationships for TiN as a function of temperature and partial pressure of nitrogen (P_{N_2})in alloy IN718 [62].

It can be seen from the table that TiN is highly stable at high process temperatures (1700 K) and under high vacuum. The solubility of N in alloy IN718 at T_{liq} (1340 ^{0}C) as determined from the solubility product of TiN is found to be about 39 ppm [N]. This implies that

the TiN inclusion content in the liquid alloy will become zero, when the equilibrium nitrogen content is less than 39 ppm at T_{liq}.

T (K)	P_{N2} (atm)	Saturation [N] (ppm)
1700	4.8×10^{-5}	39
1800	4.0×10^{-4}	112
1900	2.7×10^{-3}	290
2000	1.2×10^{-2}	620

Table 3 Saturation solubility of TiN in IN718. (from [62]).

2.6 Summary

Studies on random grain formation in superalloys in the past years have suggested that one or more of the following factors were responsible for the formation of spurious grains in superalloys. They are a). Thermosolutal convection (where the limiting factors are determined to be the temperature gradient and the primary dendrite arm spacing between the advancing dendrites), b). Constitutional undercooling (where the criterion for spurious grain formation are determined to be the temperature gradient, and the solidification rate).

On the basis of the Turnbull-Vonnegut lattice disregistry model, TiN has been found to be an effective inoculant in ferritic stainless steels. Application of this disregistry theory to TiN precipitation in Ni-based superalloys reveals that the lattice mis-match between TiN particle and the FCC Ni matrix is < 20%. Hence, TiN is an effective heterogeneous nucleant.

Considering the following facts, a) the high casting temperatures (typically 1500 °C) used in typical casting experiments; b) the stability of TiN particles under these conditions; and c) comparing the calculated values for undercooling of TiN and HfN in Ni-based superalloys with

the undercoolings produced during the directional solidification of single crystal turbine blades [38], compels the idea that the source for spurious grain formation may be a foreign substrate like a TiN inclusion.

Chapter 3: Objectives

The principal aim of this study is to verify the hypothesis that the TiN particles are stable in the region ahead of the solidification front (just above the liquidus isotherm) during solidification. Other objectives of the study address some critical issues regarding TiN precipitation during directional solidification.

A quantitative study on the TiN precipitation kinetics under different conditions (nitrogen partial pressures, withdrawal rates etc.) would enable to determine if the TiN particles precipitated in the solid/liquid mushy region can float out of the solidifying interface. At this point, it is essential to distinguish between the survival of equilibrium TiN particles that are precipitated just above the liquidus isotherm and the flotation (if at all) exhibited by TiN particles precipitated in the solid/liquid mushy region.

Considering the density difference between the TiN particles (5.2 g/cm^3) and that of liquid IN718 alloy (7.6 g/cm^3), and also taking the effect of buoyancy forces in the liquid alloy, is it reasonable to assume that the TiN inclusions would float out of the solidifying interface? Also, it is to be noted that high temperature gradients cause re-solutioning of TiN particles. Hence, finally the conditions that lead to the flotation of TiN particles have to be determined.

Chapter 4: Theoretical Methodology For TiN formation In Alloy IN718

The determination of the equilibrium nitrogen concentration for the formation of TiN at various conditions (temperature, nitrogen pressure etc.) is a crucial and an essential part of this thesis. There are insufficient thermodynamic data or citations available in the earlier studies to theoretically determine the equilibrium nitrogen content required for the formation of TiN in alloy IN718. This chapter describes in detail the theoretical methodology and thermodynamic calculations employed to determine the equilibrium conditions for the solubility of nitrogen and the formation of TiN in alloy IN718.

4.1 Solubility of Nitrogen in alloy IN718

The dissolution of nitrogen in liquid iron alloys can be applied to nickel-based superalloys, on the assumption of a similar behavior, and is represented by:

$$\tfrac{1}{2}\,N_2 \leftrightarrow [N]\ (1\text{wt\% liquid iron}) \tag{26}$$

The free energy of the reaction is given by [65]:

$$\Delta G^{o} = 3598 + 23.89T \text{ Joules} \tag{27}$$

The available values for the first order interaction coefficients of nitrogen with various elements in steel, as determined by Elliot [66], were substituted in equation 19 in order to determine the activity coefficient of nitrogen (f_N) in alloy IN718. This value was determined to be 0.065. The solubility constant for the reaction can be calculated using equation 20, and at the liquidus

temperature for alloy IN718 (1340 °C), it was found to be 0.0432. The solubility of nitrogen can be calculated at various pressures using equation 28.

$$f_N [\%N] = K (\sqrt{P_{N_2}}) \quad (28)$$

This data is presented in Table 4.

Nitrogen pressure Units used in experiments	P_{N2} (atm)	[N] (ppm)
400 microns	5.5×10^{-4}	156
100 microns	1.4×10^{-4}	78
40 microns	5.5×10^{-5}	49
10 microns	1.4×10^{-5}	25
3.5×10^{-5} Torr	4.5×10^{-8}	1.4

Table 4. Relation between P_{N2} and [%N] for alloy IN718 (at T_{liq} = 1340 ^{0}C)

From Table 4, it can be seen that for alloy IN718, the solubility of nitrogen is quite high at pressures of about 10^{-4} to 3.5×10^{-5} atm.

4.2 Solubility of TiN in alloy IN718

The dissolution of TiN in iron alloys can be applied to nickel based alloy systems and is given by equation 29. The free energy for the reaction is given by equation 30[67]:

$$TiN(s) = [Ti](1 \text{ wt\% in liquid iron}) + [N](1 \text{ wt\% in liquid iron}) \quad (29)$$

$$\Delta G^o = 308780 - 114.35T \text{ Joules} \quad (30)$$

The first order interaction coefficients for Ti and nitrogen were determined from the corresponding data available for steel [66], and were assumed to be the same for alloy IN718. This was then substituted in equation 24. The activity coefficients for Ti and nitrogen were determined to be 0.372 and 0.065 respectively. The solubility constant K was calculated using equation 22 and was found to be 94.26 x 10^{-6}. The equilibrium nitrogen content required for the formation of TiN can be calculated using equation 31.

$$(\%N) = \frac{K_{sp}}{(\%Ti)(f_{Ti} \cdot f_N)} \tag{31}$$

Table 5 presents the variation of the equilibrium nitrogen contents with temperature (above the liquidus temperature 1340 °C)

Figure 17 is a graphical presentation of the relation between superheat and the equilibrium nitrogen contents required for the formation of TiN, as presented in Table 5.

T °C	Superheat (°C)	[N] ppm
1340	0	39
1390	50	78
1440	100	149
1490	150	311

Table 5. Equilibrium nitrogen contents required for the formation of TiN particles above T_{liq} in alloy IN718.

Below the liquidus temperature, the segregation effects of Ti and nitrogen in the mushy region, along with the effect of temperature play a significant role in reducing the TiN solubility

considerably. The segregation of titanium in the mushy region in alloy IN718 is known and is presented in Figure 18 [68]. Though it is established that Ti segregation and nitrogen segregation take place simultaneously, the extent of nitrogen segregation is unknown. Table 6 presents the variation of the equilibrium nitrogen contents required for the formation of TiN particles below the liquidus temperature in alloy IN718, taking into account Ti segregation.

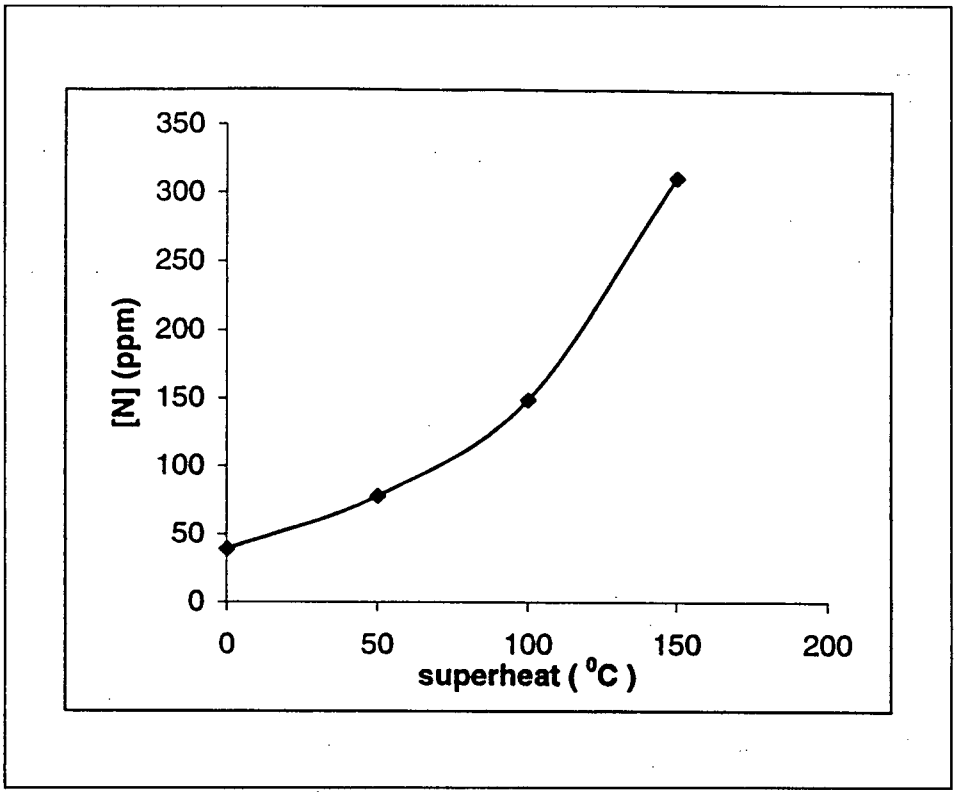

Figure 17. Relation between superheat and the equilibrium nitrogen contents required for the formation of TiN particles in alloy IN718.

These results indicate that TiN formation in nickel based superalloys is dependent upon the following factors: a) Temperature, b) nitrogen pressure, c) segregation effects of elements (e.g. Ti and nitrogen in alloy IN718), and d) the equilibrium nitrogen concentration.

Therefore, the above calculations indicate that when the nitrogen content of the alloy at the liquidus temperature (1340 ^{0}C) is below the equilibrium nitrogen concentration of 39 ppm, there is no TiN precipitation.

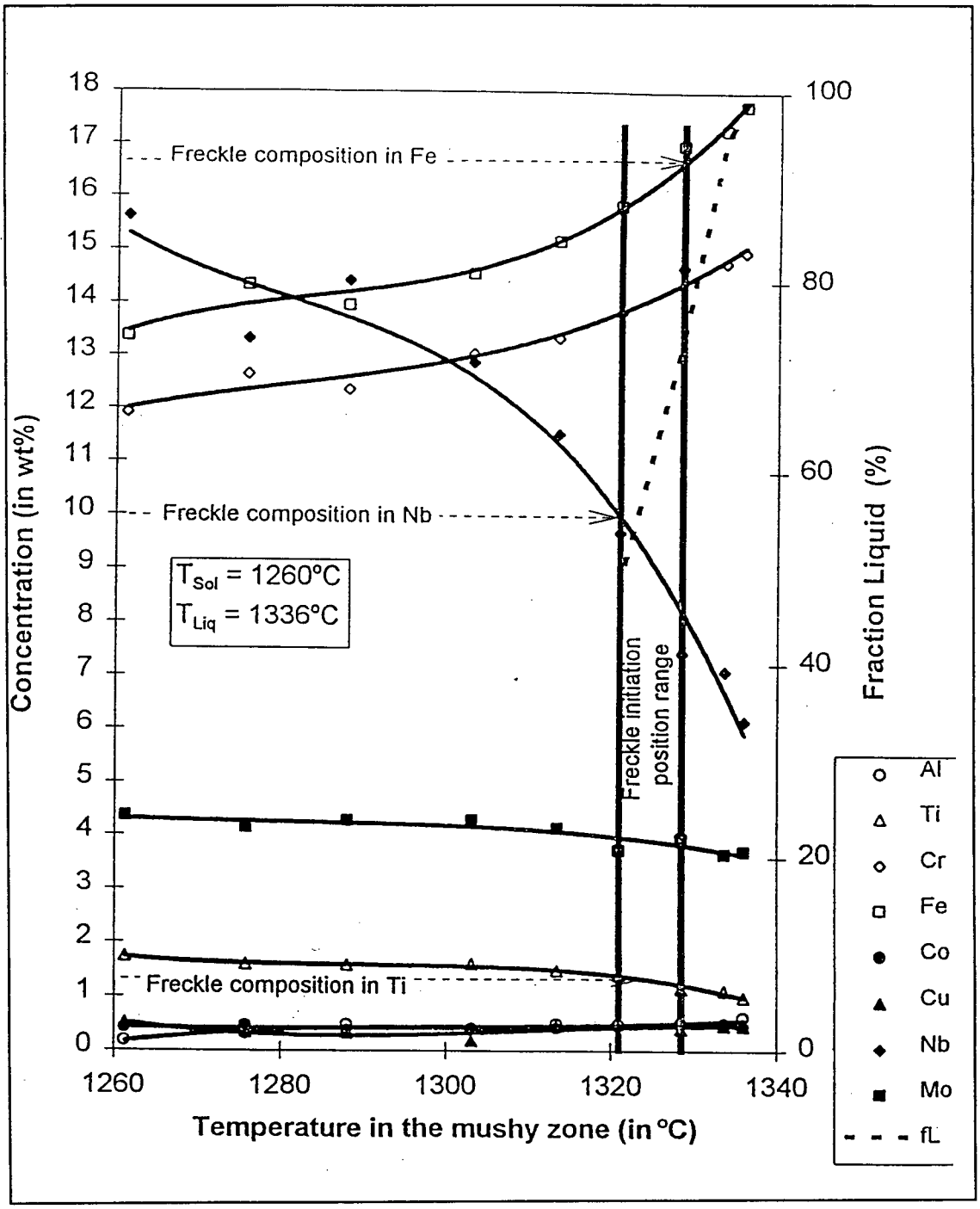

Figure 18. Segregation of Titanium in the mushy region in alloy IN718 (from [68]).

T °C	[wt. %Ti]	[N] ppm with Ti segregation	[N] ppm without Ti segregation
1340	1	39	39
1320	1.5	19	29
1300	1.6	14	22
1280	1.7	9	16
1240	2	4	9

Table 6. Effect of Ti segregation on the equilibrium nitrogen contents required for the formation of TiN below the T_{liq} in alloy IN718.

Chapter 5: Experimental Studies

SX/DS casting alloys are now extensively used for turbine blade materials (both aero and industrial turbine blades). In spite of the desirable mechanical properties, these materials are found to exhibit random grain formation during solidification. It is proposed in this thesis that the TiN inclusions may be a possible source for spurious nucleation in the SX/DS alloys. Since data for SX alloys such as: a) the saturation solubility of TiN, b) thermodynamic data pertaining to nitrogen solubility and TiN formation etc. are not available, alloy IN718 was selected as a model system. Other reasons for selecting alloy IN718 are: a) it is a very common Ni-based superalloy, and b). studies on alloy IN718 have been done earlier, which are relevant to the present studies. Hence, it makes IN718 alloy a convenient model system.

5.1 Alloy Compositions Used For experiments

Three different composition A (with 67 ppm [N]), B (with 64 ppm [N]) and C (with 4 ppm [N]) of the nickel-based alloy 718, as given in Table 6 were chosen for the present studies. The equilibrium freezing range for alloy IN718 is 1260 °C (solidus temperature) – 1340 °C (liquidus temperature).

5.2 Sample Preparation

The samples to be directionally solidified were machined to small rods of about 10-11 g in weight, 6-7 cm in length and 5.2 mm in diameter, in order to fit inside a high purity alumina crucible plugged with a high purity, low-porosity, non-reactive alumina cement. The samples were thoroughly cleaned and dried with alcohol to remove any machine debris on them before being placed in the crucible.

Elements (wt%) / IN718 Alloy	Ni	C	S	Mn	Si	Cr	Co	Fe	Mo	W	V	Nb	Ta	Ti	Al	B	Hf	Zr	P	Cu
A	53.16	0.034	.000	0.07	0.07	17.9	0.39	18.4	2.97	0.07	0.03	5.27	0.01	0.99	0.45	.002	0.01	.003	.000	.009
B	52.99	0.032	.000	.07	.06	18.0	.26	18.4	2.94	.06	.02	5.51	.007	.95	.57	.002	-	.002	.01	.04
C	54.03	.008	.006	.001	.007	17.9	.001	18.0	2.96	0.01	.004	5.03	.001	.96	.49	.001	-	.001	.001	.025

Elements (ppm) / IN718	O	N	Mg
A	11	67	22
B	5	64	31
C	9	4	10

Table 7. Alloy compositions used in the experiment

5.3 Apparatus and Procedure

The apparatus used is a variation of the classical Bridgeman furnace. It is a directional solidification and quench (DSQ) vacuum induction furnace. A photograph and a schematic of the furnace are shown in Figure 19 and Figure 20 respectively. The main chamber consists of an outer quartz tube and an inner susceptor tube (alumina tube surrounded by molybdenum foil) into which the crucible containing the sample can be freely lowered or pulled up by means of an A.C synchronous motor (30 rph) and a shaft arrangement. The inner susceptor tube is surrounded by a set of three outer alumina tubes for radiation shielding. The tubes rest on a flat water-cooled copper chill, with a provision at the center to effect the quenching process.

The sample was heated by means of an induction coil, which surrounds the outer quartz tube. The induction coil is a water-cooled copper coil, connected to a 5 kW, 450 kHz power supply. The top of the susceptor tube marks the beginning of the 'hot zone', which extends to about 140 mm. The temperature gradient, which is a very important parameter in the solidification process, was measured by a W-3%Re and W-25% Re thermocouple. Different runs were performed to measure the temperature gradient, as presented in Figure 21. The Temperature gradient at the lower portion of the coil from where the ingot will be withdrawn was found to be a constant for each run. The average temperature gradient (G) was found to be 8×10^3 °C/m. Another important parameter is the solidification rate (R) for the process. For the present experiments, the rate at which the sample moves thorough the zone is governed by the speed of the A.C synchronous motor. For the 30 rph motor used in the experiments, the withdrawal rate was found to be 8.1 μm/sec.

The entire chamber was maintained at a high vacuum of about 3.5×10^{-5} Torr using a diffusion pump and a mechanical pump. This vacuum was found to be very effective in producing samples with a very clean exterior, i.e., without any scale formation or contamination on the surface. The exterior of such a directionally solidified ingot directly taken out from the

furnace are presented in Figures 22 (a) and (b).

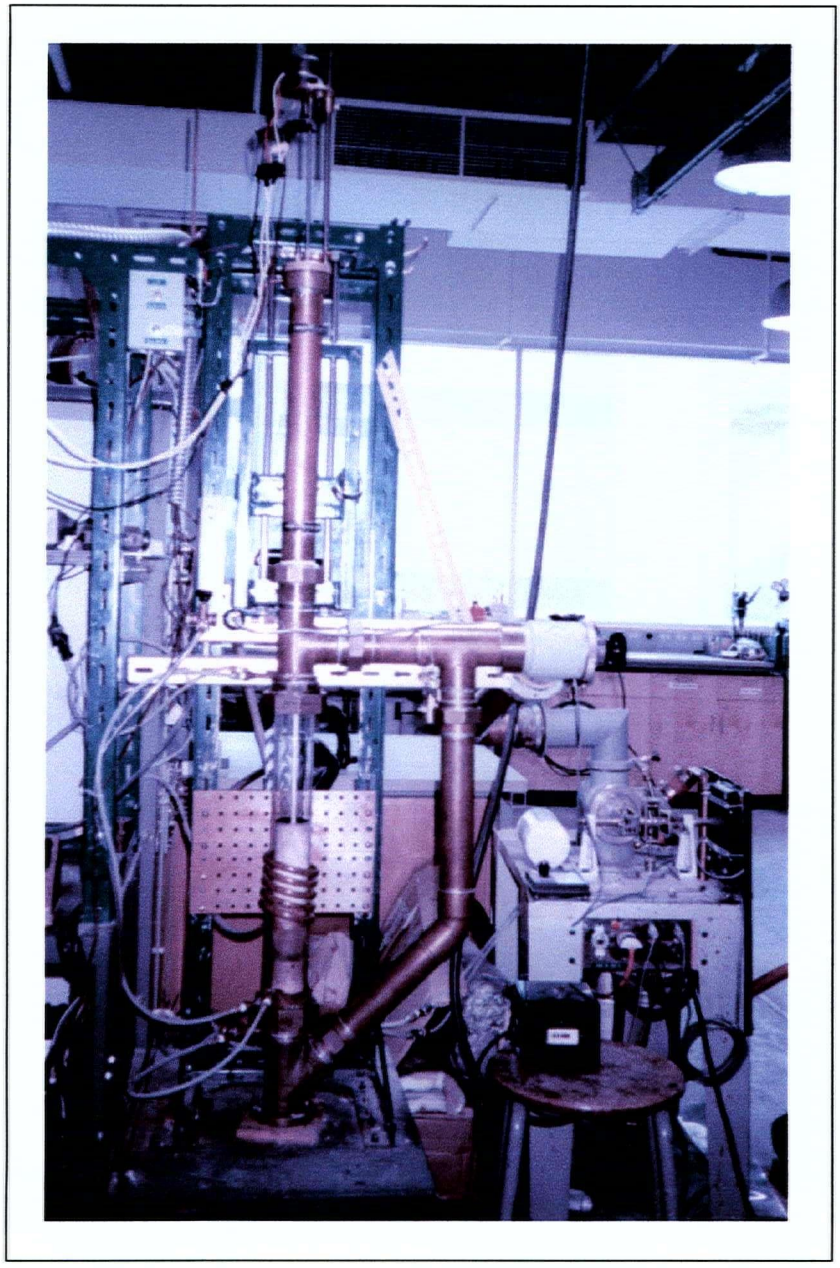

Figure 19. The DSQ apparatus

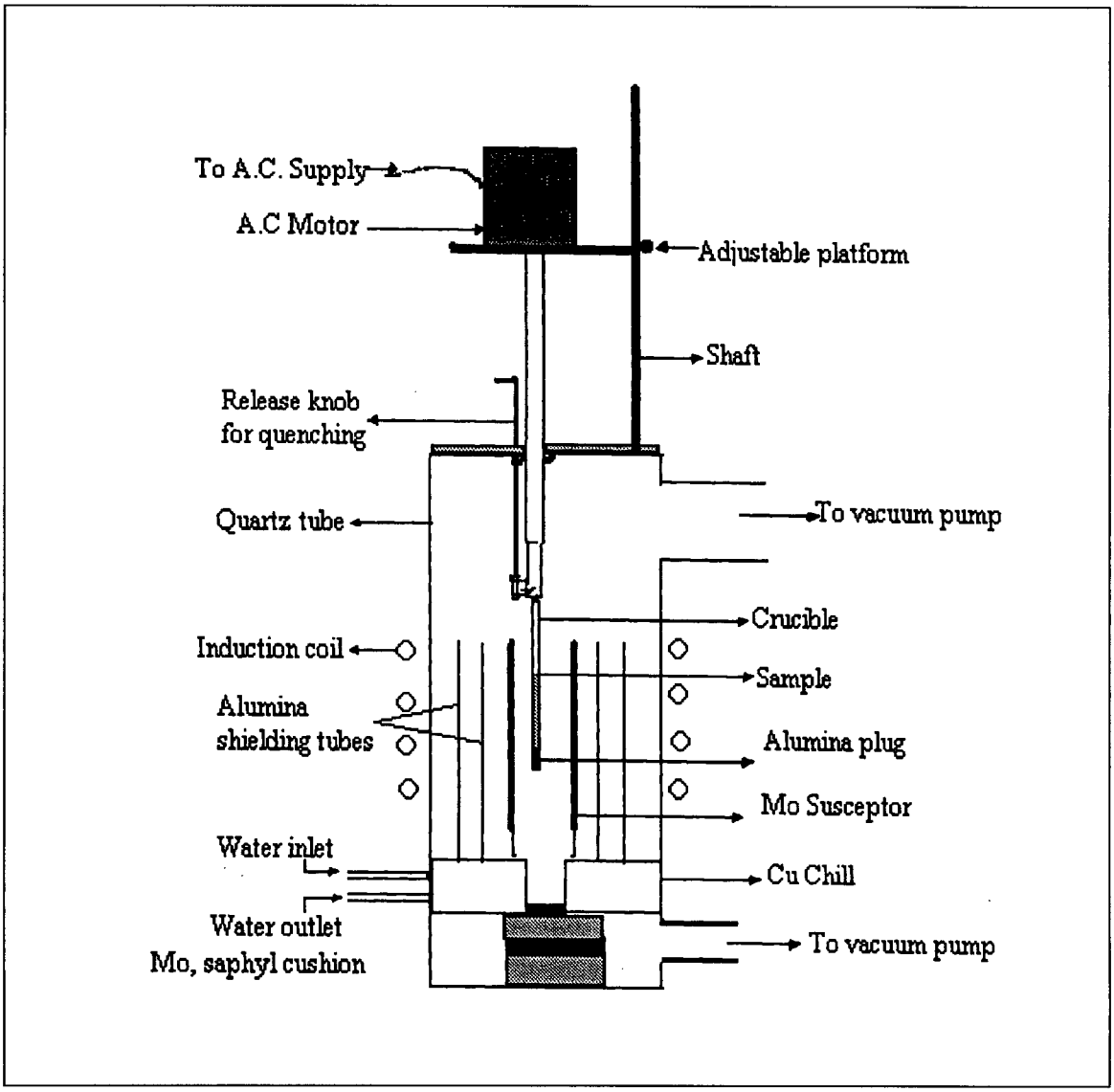

Figure 20. Schematic of the DSQ apparatus

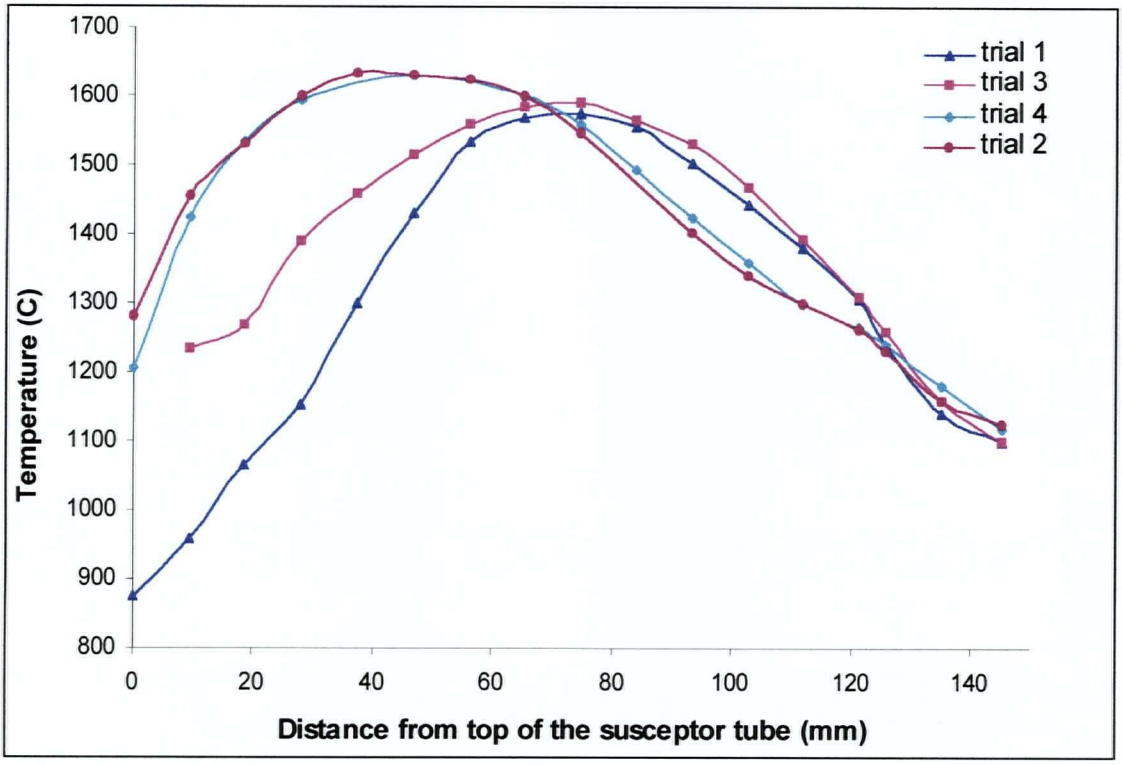

Figure 21. Temperature distribution along the induction coil in the DSQ at 2.5 kW.

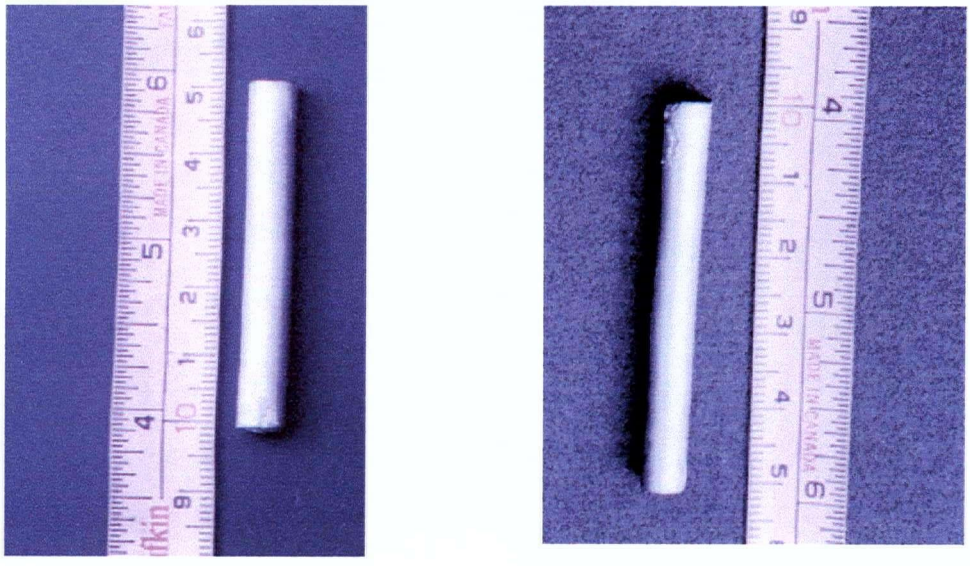

(a) (b)

Figure 22 (a) and (b) Exterior of some directionally solidified ingot (directly taken out from the DSQ).

The crucible was lowered into the susceptor tube to the required depth (at which the temperature is well above the liquidus temperature of the alloy) by mechanically moving the shaft. Then, the chamber was evacuated using the mechanical pump and then switching on to the diffusion pump once the pressure reaches below 200 μm (read from the vacuum gauge). When the chamber pressure reaches about 10^{-4} Torr, the power is switched on. After setting the desired power level of 2.5 kW, the sample is held for half an hour (by this time the sample is completely liquid) and the motor is switched on. The distance moved by the sample inside the hot zone is read by converting the number of turns the shaft makes, as read by the mechanical counter, into the corresponding linear distance.

For a complete directional solidification process, after the sample has completely exited the hot zone, the power is turned off and the sample is allowed to solidify (the only heat losses being that of radiation).

When a quenching process is desired, it was realized by turning a small lever from outside, which detaches a molybdenum wire connecting the crucible with the shaft, thus releasing the crucible. As the crucible drops down it enters the quench zone at the bottom of the chamber beneath the copper chill, which is filled with layers of saphyl and molybdenum sheet to provide cushioning effect for the crucible as it falls.

The final directionally solidified (DS) or directionally solidified and quenched (DSQ) ingots are metallographically prepared by the following method.

5.4 Metallographic Analysis

The samples were found to be very clean indicating a good vacuum through out the experiment. The ingot was mounted on a resin along the length, and ground to a width of about 5mm in grinding wheels of 60, 120, 180, 320 and 600 grits successively. It was then polished first in a 5 μm diamond and then in a 1 μm diamond cloth polishing wheels. If the sample was directionally

solidified and quenched, it was divided into equal areas 10mm in height, above and below the interface, along its entire length. The samples were etched with Kallings' II reagent (2g $CuCl_2$ + 40 ml HCl + 40 - 80 ml ethanol). After etching the interface, which is the transition from the coarse dendritic columnar region to a fine structure, in each sample can be clearly distinguished. In most of the samples, this interface is perpendicular to the growth direction as shown in Figure 23, and in some cases, it is at an angle to the growth direction as shown in Figure 24, depending upon the heat withdrawal characteristics.

If the sample was a completely directionally solidified one, it was again divided into equal areas of 10mm in height from the top (the final portion of the liquid to solidify) to the bottom, along its entire length. The number of titanium nitride inclusions in each region was physically counted while observing through an optical microscope at a magnification of 800x.

A schematic of the analysis in the case of a directional solidification and quenching and a complete directional solidification are presented in Figure 25(a) and (b) respectively.

The TiN particles are distinguished from other inclusions like carbides and carbo-nitrides and counted. Under an optical microscope, the nitrides can be distinguished from other precipitated phases by their color. The nitrides usually have a pinkish or yellow-orange color, often with a dark nucleus. A typical TiN particle as observed from a SEM (scanning electron microscope) is presented in Figure 26. An EDX microprobe analysis reveals that most of the TiN inclusions have an aluminum rich core. The carbides appear as grayish or bluish particles and the carbonitrides are found to have a very distinct pinkish core with a grayish outer region surrounding them. Other phases like the niobium rich Laves and needle shaped delta phase (Ni_3Nb) (which are unavoidable in nickel alloys containing Nb) were also observed which are described in detail in Appendix 6.

The samples are then observed under the scanning electron microscope (SEM) to measure the TiN particle sizes at different regions on the polished specimen.

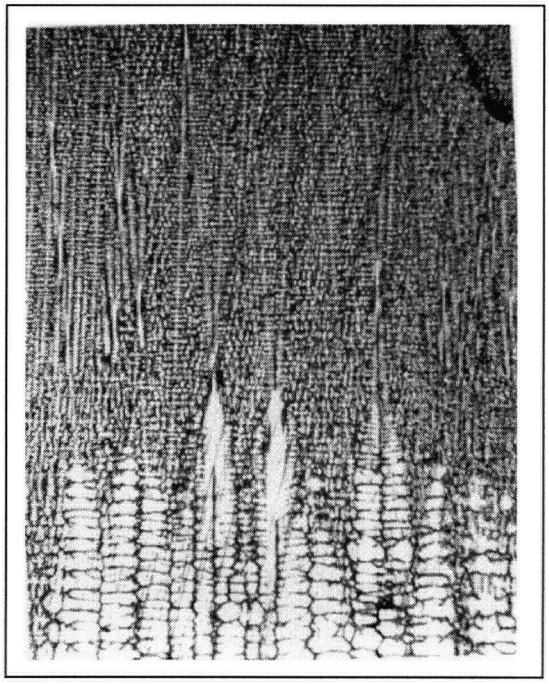

Figure 23. Quenched interface perpendicular to the direction of withdrawal.

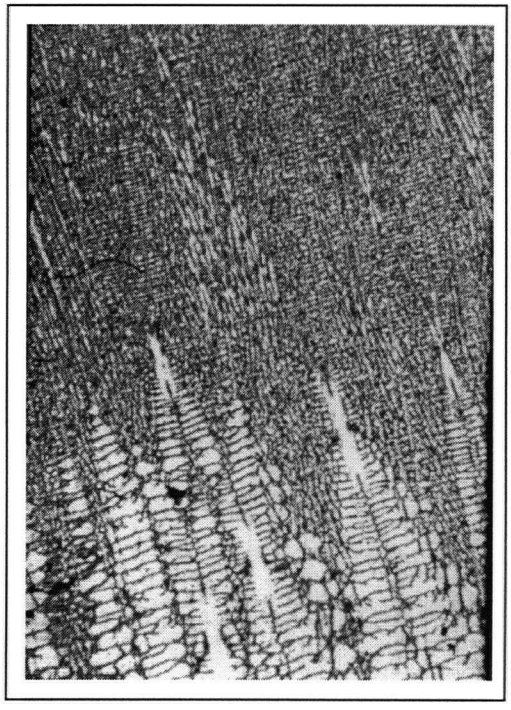

Figure 24. Quenched interface at an angle to the direction of withdrawal.

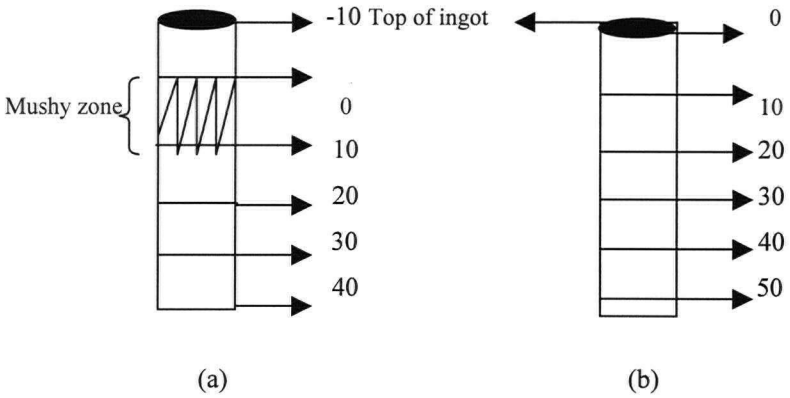

Figure 25. Schematic quantitative analysis of TiN in (a) DSQ samples, (b) DS samples.

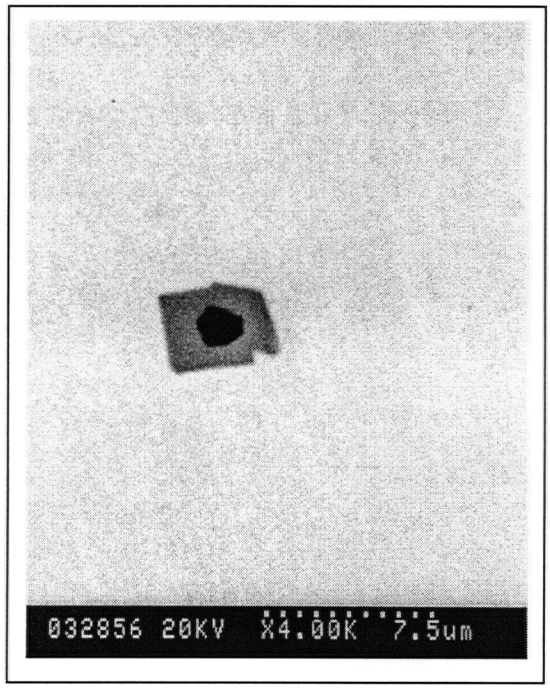

Figure 26. A typical TiN inclusion showing a prominent alumina core.

5.5 Primary Dendrite Arm Spacing

In the directional solidification process, the temperature gradient (G) and the solidification rate (R) are the two important solidification parameters. The relation between the cooling rate (G x R) and the dendrite arm spacing has been investigated for many superalloys [69] and this relation is presented in Figure 27.

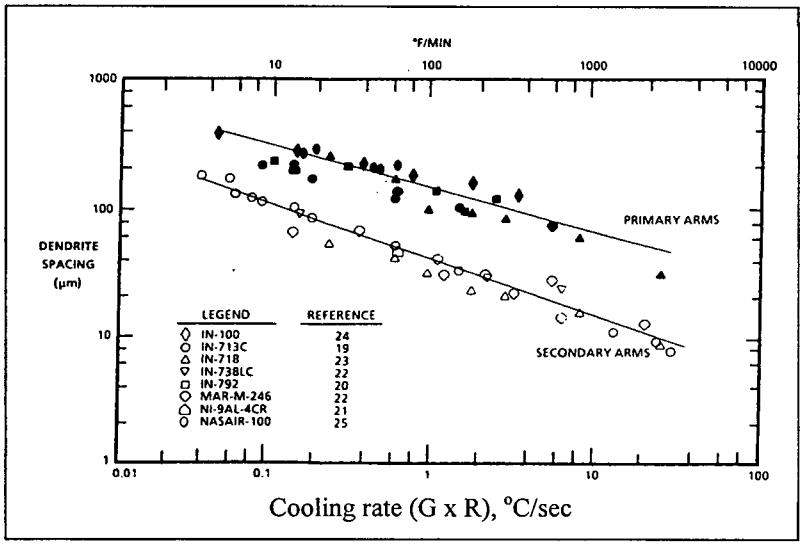

Figure 27. Dendrite arm spacings for several directionally solidified superalloys as a function of the cooling rate. (from [69]).

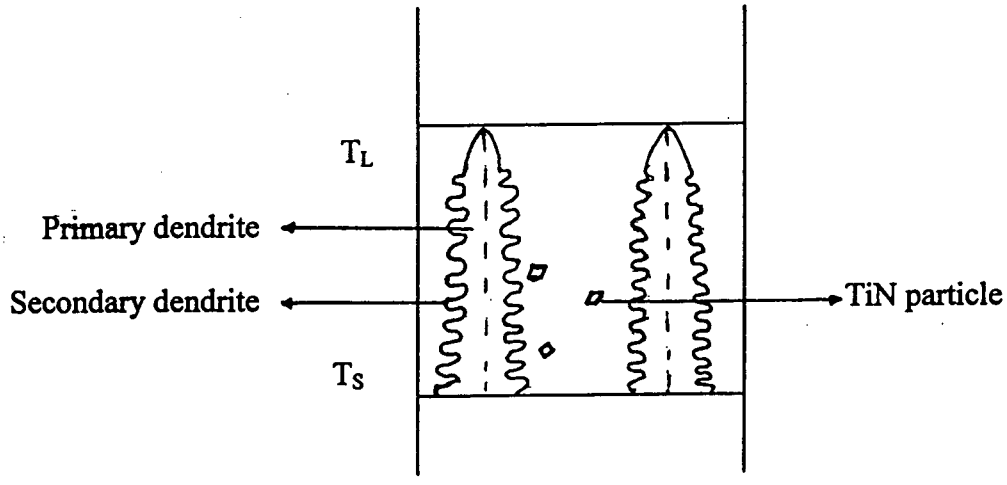

Figure (28). Schematic of the mushy interdendritic region in alloy IN718 with TiN precipitates.

The primary aim is to quantitatively verify whether the TiN particles can float out of the solidifying interface. The finer the dendrites, the greater is the chance that the TiN particles may be caught up between the dendrites. Therefore, for the present studies a coarse dendritic structure i.e. large primary dendrite arm spacing is desired in the ingots. The wide interdendritic spacing offers less resistance to fluid flow, hence could facilitate flotation. Figure 28 is a schematic of the mushy interdendritic region of alloy IN718 along with the precipitated TiN particles. Please note that the typical value for the primary dendrite arm spacing is about 400 microns and that for the TiN particles is about 6 microns. (The figure is magnified approximately 50 times).

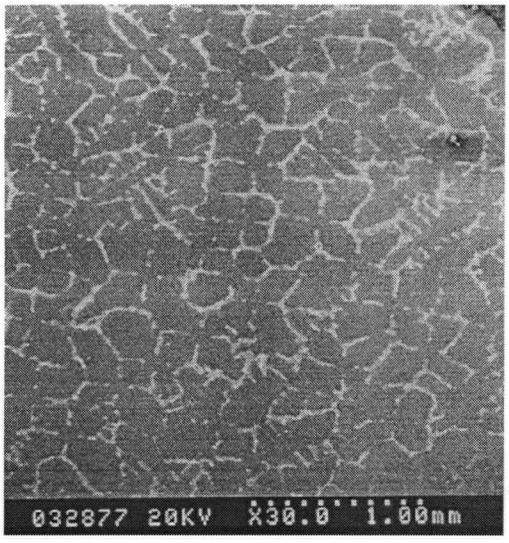

Figure 29. SEM picture of the PDS in sample 2 (64 ppm [N], DSQ sample).

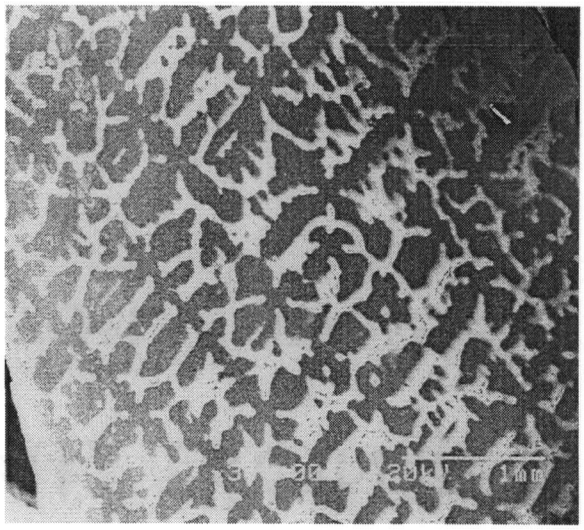

Figure 30. SEM picture of the PDS in sample 1 (68 ppm [N], DSQ sample).

The primary dendrite arm spacing was directly measured by observing the etched cross-sections of the sample in the SEM (Scanning electron microscope). Figure 29 and Figure 30 present such an SEM picture of the primary dendrite cross-sections observed in samples 2 and 1 respectively.

Table 8 gives the average primary dendrite arm spacing for Samples 1 and 2 as measured from the SEM pictures. Corresponding to the value of (G x R) used in the present study (0.065 °C/s), the primary dendrite arm spacing (PDS) is found to be about 400 μm from Figure 27, which agrees well with the values obtained here (Table 8).

Alloy	Sample 1 (68 ppm [N])	Sample 2 (64 ppm [N])
P.D.S (μm)	414	425

Table 8. Primary dendrite arm spacing of sample 1 and 2 as calculated from the SEM pictures.

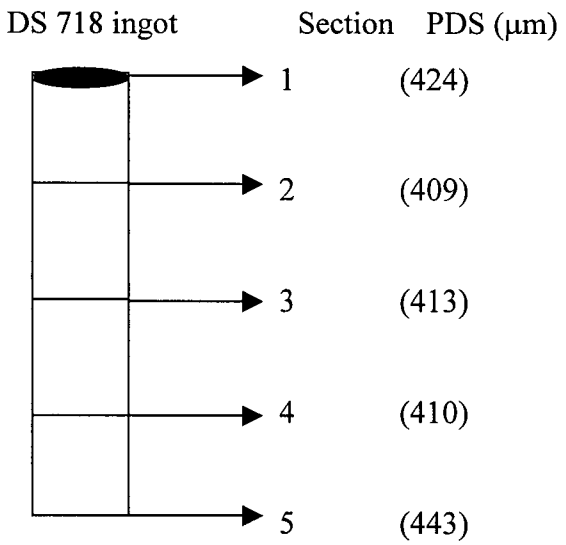

Figure 31. Schematic of PDS determination at different sections of the DS cast ingot (sample 5, 64 ppm [N]).

Also the DS cast sample 5 (64 ppm [N]) was sectioned horizontally at different portions along its length, and each portion was ground and polished at the flat surface. These polished surfaces were etched with Kallings' reagent to observe the transverse microstructure under the scanning

electron microscope. Figure 31 presents a schematic of this procedure and Table 9 presents the average PDS at each section, as measured from the SEM pictures. The PDS values at these sections were almost a constant.

Section	PDS (μm)
1	424
2	409
3	413
4	410
5	443

Table 9. Average primary dendrite arm spacing at different portions of the DS sample 5 (64 ppm [N]).

5.6 Buoyancy Effect on TiN

Alloy IN718 doesn't exhibit density changes due to solute segregation in the S/L mushy region, unlike the SX/DS alloys which freckle. Note that IN718 has a very low carbon content (0.008 wt%), which may contribute to the fact that the alloy does not exhibit freckling.

In the case of SX/DS alloys, freckling occurs by density inversion due to solute rejection in the segregation zone. There is fluid flow in this region and thus thermosolutal convection is established [70-72]. The maximum velocity at the center of a freckle plume was calculated in the NH_4Cl-H_2O castings and in using a modified Poiseuille equation [70,72]. This was later extended to lead alloy systems (Pb-Sn and Pb-Sb) by Sarazin et. al [70] and the freckle velocity was determined to be 100 mm/sec.

From a point of view of buoyancy, an inclusion like TiN is similar to a solid particle, which can either sink or float in the liquid depending upon whether its density is higher or lower relative to the density of the liquid alloy, and the viscous drag on it. Since, the density of TiN particles (5.2 g/cm^3) is lesser than the density of IN718 (7.6 g/cm^3) at the T_{liq}, in principle, buoyancy forces ought to be the driving force in causing the flotation of the TiN particles.

In general, the Stokes' principle can be applied to calculate the "velocity of rise" or "velocity of sink" of a spherical particle in a viscous liquid. For the purpose of the thesis, the Stokes' principle is modified to accommodate cubic TiN particles by replacing the volume of the spherical particles by the volume of the cubic particles (see equation 32-33 for details). Any discrepancy arising from the "shape effects" is assumed to be small and is ignored for the purpose of calculation. Using this modified Stokes' principle, the velocity of rise of cubic TiN particles in the liquid IN718 alloy may be calculated as follows:

The viscous drag on the particle of density ρ, and volume d^3 (assuming that the TiN particles are cubic with each side = d units) in a liquid alloy of density σ, and coefficient of viscosity η, is given by:

$$6\pi\eta dV_s = (\text{mass of [TiN]s}) \times g - (\text{mass of equal volume of } [IN718]_{liq}) \times g \quad (32)$$

$$6\pi\eta dV_s = (d^3\rho)g - (d^3\sigma)g \quad (33)$$

$$V_s = \frac{d^2(\rho-\sigma)g}{6\pi\eta} \quad (34)$$

where, g is the acceleration due to gravity (9.8 m/s^2) .

Equation 34 is the Stokes' relation. This indicates that the TiN particle floats up with a velocity V_s. Also, it can be inferred that due to the buoyancy effect, the larger the particle the higher is the rise velocity.

As an example, substituting the corresponding values of π, ρ, σ, and η the velocity of flotation of a typical TiN particle of size d = 6 μm in equation 34 gives:

$$V_s = - \frac{(6x10^{-6})^2(5200-7632)}{6x3.14x0.0045} x9.8 \quad (35)$$

$$V_s = - 10 \text{ μm/sec} \quad (36)$$

Using a similar calculation, the velocity of rise of TiN particles of various sizes are tabulated and presented in Table 10.

TiN particle size (μm)	Stokes' velocity of rise (μm/sec)
4	4.5
5	7
6	10
8	18
10	28

Table 10. Velocity of rise (V_s) of TiN particles of various sizes.

From Table 10, using the present withdrawal rate of 8.1 μm/sec, it is reasonable to expect that in principle TiN particles of size ≥ 6 μm should be able float out of the solidifying front of the ingot.

In the case of lead alloys systems (Pb-Sn and Pb-Sb) that exhibit freckling, the velocity at the center of the freckle plume is about 100 mm/sec [70]. Assuming a similar value for freckle rise velocity in the case of DS/SX Ni-based alloy systems, there is a high possibility that at such low withdrawal rates, the smaller TiN particles might be carried by the freckle plumes from the mushy zone and thus might be able to "escape" out of the solidifying interface.

5.7 Experiments

Basically, the experiments conducted consist of two steps. In the first step, the samples were directionally solidified and quenched (DSQ) in an induction furnace, under vacuum. The quenched samples were then metallographically prepared and a quantitative assessment of the distribution of nitrides in various regions above and below the liquidus was made. This helps in understanding the chemistry of TiN at the interface (in the solid/liquid mushy region, and above the liquidus).

The second step consists of a complete directional solidification of the samples (the same IN718 ingots with various nitrogen contents) in the furnace, under different conditions of pressures and withdrawal rates, and assessment of the final DS ingots to see whether the nitrides are collected at the top of the ingot. This step helps to determine what are the conditions that can or cannot lead to the TiN precipitation and their flotation above the solidification front, thus verifying or disproving the assumed hypothesis.

Table 11 presents the different samples were used for the DSQ (directional solidification and quenching) and DS (directional solidification), and the conditions under which these experiments were conducted.

Sample	Alloy	[N] content (ppm)	Experiment Conducted	Pressure	Withdrawal rate (μm/sec)
1	A	67	DSQ	3.5×10^{-5} Torr	8.1
2	B	64	DSQ	"	"
3	C + Cr_2N	48	DSQ	"	"
4	C+ Cr_2N	90	DS	"	"
5,6	B	64	DS	"	"
7	" (homogenized)	90	DS	"	"
8	"	90	DS	"	2.4
9, 10	"	90	DS	100 μm nitrogen pressure	8.1
11, 12	"	90	DS	"	2.4
13	"	90	DS	400 μm nitrogen pressure	8.1
14, 15	"	20	DS	40 μm nitrogen pressure	2.4
16, 17	"	20	DS	10 μm nitrogen pressure	2.4

Table 11. IN718 Samples used for different experiments

Sample 3 (48 ppm [N]) and sample 4 (90 ppm [N]) were prepared from the same IN718 alloy C by adding appropriate amounts of Cr_2N. A schematic of this procedure is presented in Figure 32. The ingot was cut in half and Cr_2N was placed on top of the bottom half of the sample. The upper half was then placed over the lower half and the whole ingot was carefully slipped into the alumina crucible.

Samples 5, and 6 were prepared by melting the alloy C with appropriate amounts of chromium nitride in a separate induction furnace (in order to obtain homogeneous nitrogen composition in the ingot) and were cast into long cylindrical bars of about 5 mm in diameter.

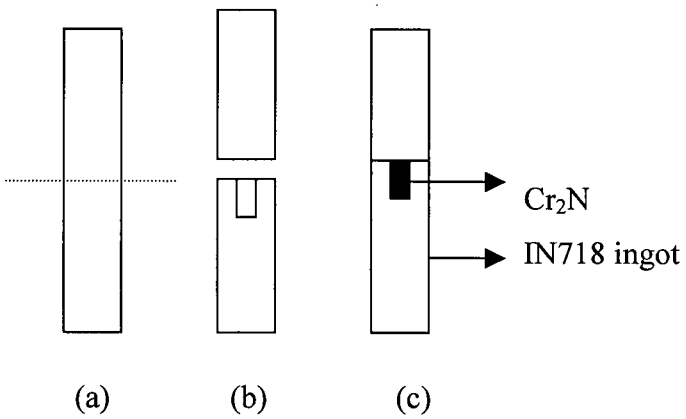

Figure 32. Schematic of the stages involved in preparing samples 3 (48 ppm [N]) and 4 (90 ppm [N]). (a) severing the sample in half (b). drilling a hole at the top of the bottom half and, (c). filling the hole with Cr_2N and closing it with the upper half.

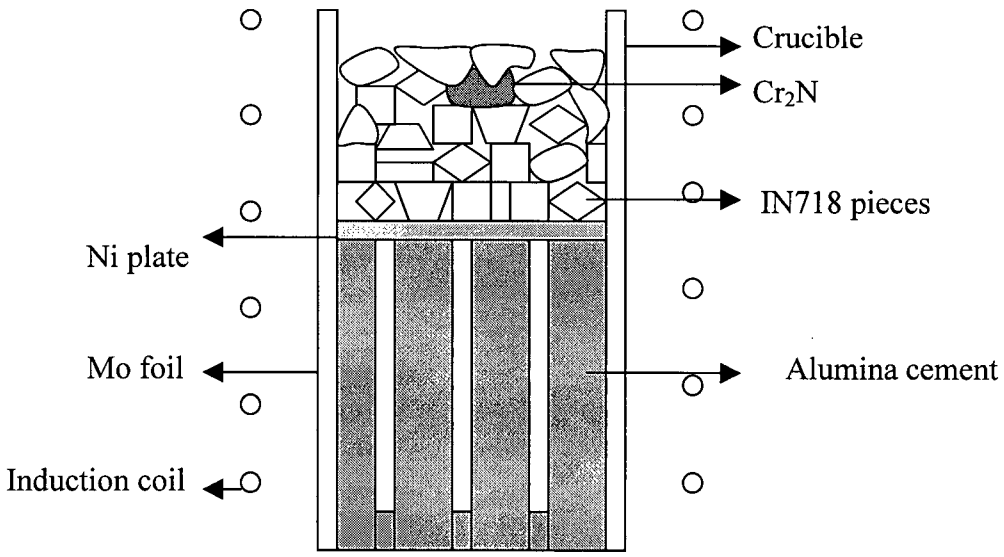

Figure 33. Schematic of the procedure to prepare homogeneous IN718 samples.

A schematic of this procedure is presented in Figure 33. These bars were cut to lengths of about 5 – 6 cms and used as individual samples to be directionally solidified in the DSQ furnace.

All the samples were metallographically prepared and examined for TiN precipitates, as discussed in section 5.4.

5.7.1 Nitrogen Analysis Of The DS Cast Samples

A higher concentration of TiN particles in the ingot would produce a higher nitrogen concentration in that area. Hence, if there is flotation of TiN particles and if the TiN particles collected on top of the ingot, the upper portion of the ingot should register a higher nitrogen content. Hence, the different portions of the DS cast samples were cut and the individual pieces were sent out to Special Metals Corporation for nitrogen analysis by a conventional gas analysis technique.

Chapter 6: Results

6.1 Directional Solidification And Quenching Experiments

A set of directional solidification and quenching (DSQ) experiments were performed on samples 1(67 ppm [N]), 2(64 ppm [N]), 3(48 ppm [N]). After the ingots were taken out of the furnace, they were prepared and polished (as discussed in section 4.6) for quantitative analysis of TiN particles. The number of TiN particles per sq. mm in each region above and below the quenched interface were calculated. From the experimental data, graphs were plotted between the density of TiN (number of nitrides per mm^2 area) and the distance along the length of the sample (with respect to the liquidus in the case of DSQ samples. This is presented in Figure 34. The number of nitrides is averaged over each of the regions i.e. from 0- (-10), 0-10, 10-20, 20-30 mm etc. and

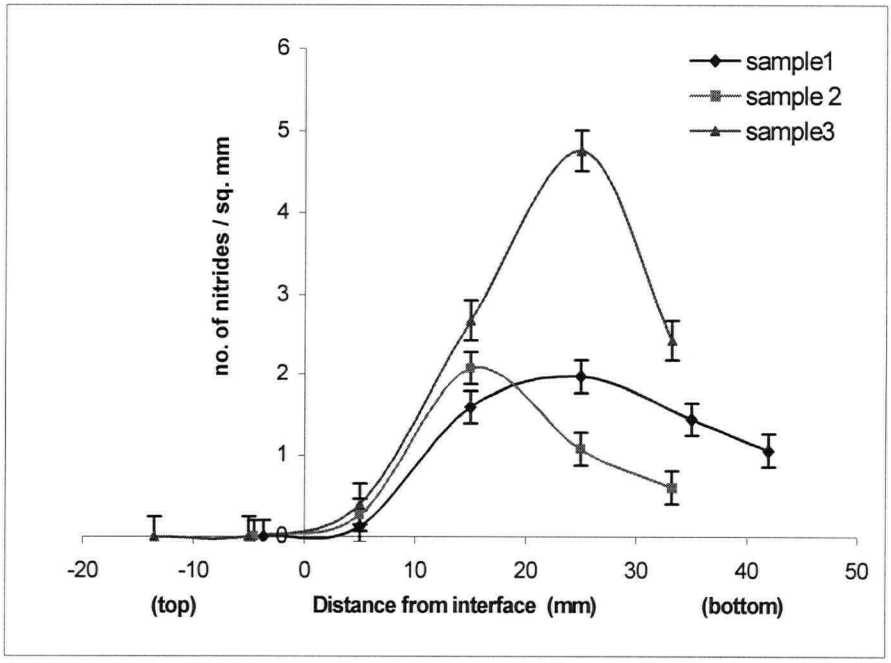

Figure 34. TiN distribution in the directionally solidified and quenched samples 1(68 ppm [N], 2 (64 ppm [N]), and 3 (48 ppm [N]) at a withdrawal rate (R) = 8.1 μm/sec.

plotted at distances of ... -15,–5, 5, 15, 25 mm etc. from the interface (refer to Figure 25). The y-error bars in the graphs are about ± 10-15% .

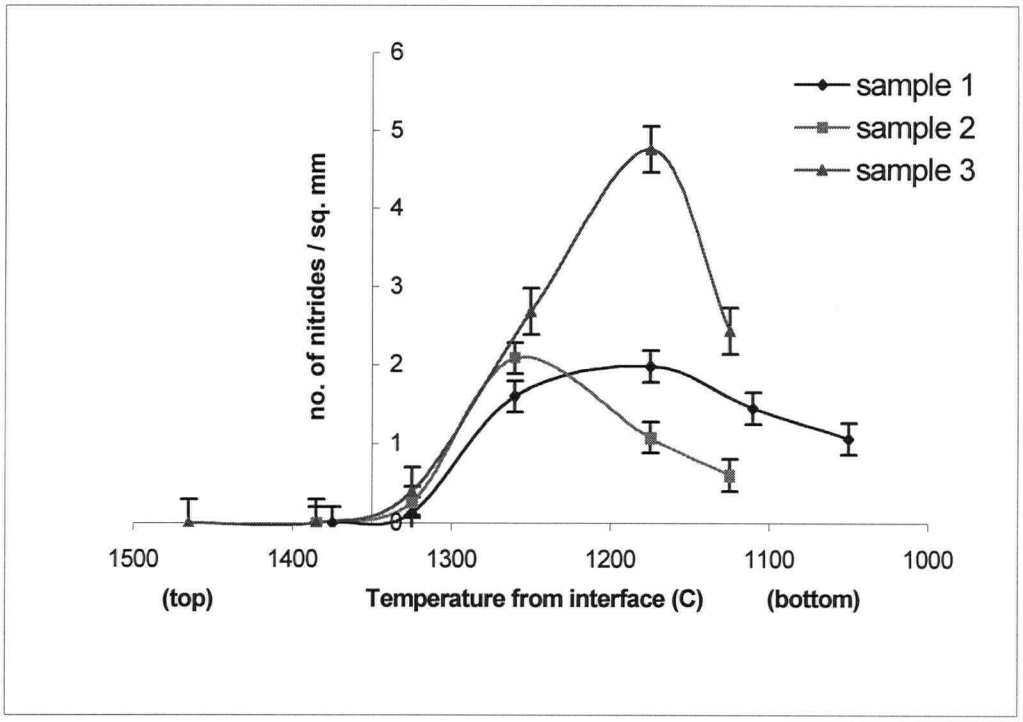

Figure 35. Temperature distribution of TiN particles in the directionally solidified and quenched samples 1(68 ppm [N], 2 (64 ppm [N]), and 3 (48 ppm [N]) at a withdrawal rate (R) = 8.1 μm/sec.

Figure 35 shows the relation between the temperature distribution and the density of TiN found in the various regions of the ingot. The temperature vs. nitrides graph 35 is plotted by converting the distances in graph 34 to the corresponding temperatures (in ^{o}C) from the temperature profile (Figure 21).

- In the quenched samples, Figure 34-35, it was found that the number of TiN particles above the T_{liq} is zero and the nitrides are found only below the T_{liq} up to a temperature of about 1340 ^{o}C.

- From Figure 34 it can be seen that sample 3 (48 ppm [N]) shows a large number of TiN particles compared to sample 1 (67 ppm [N]) and sample 2 (64 ppm [N]).

6.2 Directional Solidification (DS) Experiments

6.2.1 Samples 90 ppm [N], and 64 ppm [N]

A high nitrogen content sample with about 90 ppm nitrogen was prepared in a manner described in section 5.7 (Figure 32), and a complete directional solidification was carried out on it. Also, a complete DS was carried out on samples 5 and 6 (64 ppm [N], each from alloy B).

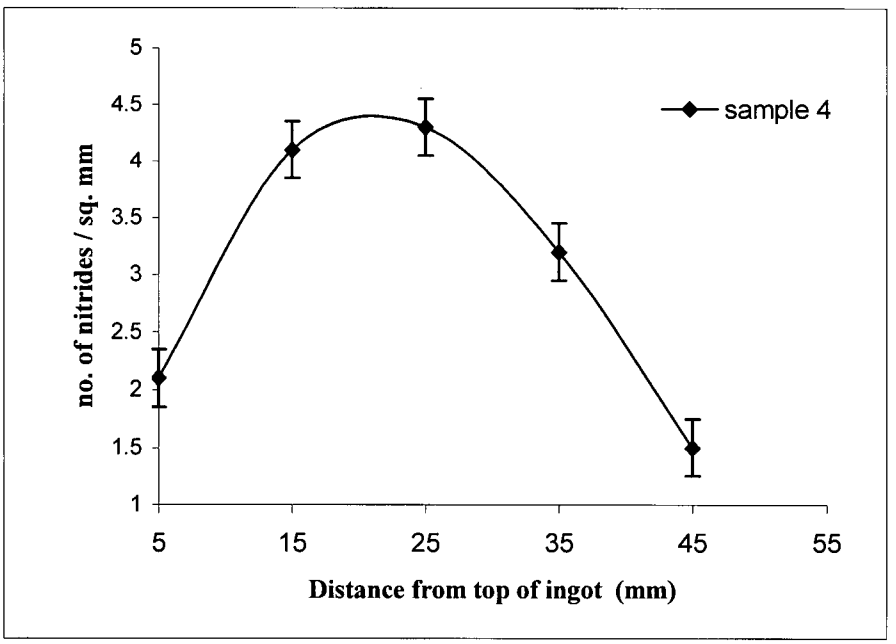

Figure 36. TiN distribution in the directionally solidified sample 4 (90 ppm[N]) at R=8.1 μm/sec.

The ingots were metallographically prepared and the density of TiN particles in each region was calculated. From the experimental data graphs were plotted between the density of TiN particles

and the distance from the top of the ingot (taken as the reference). These are presented in Figures 36 and 37 for the 90 ppm (sample 4) and the 64 ppm (samples 5,6) respectively.

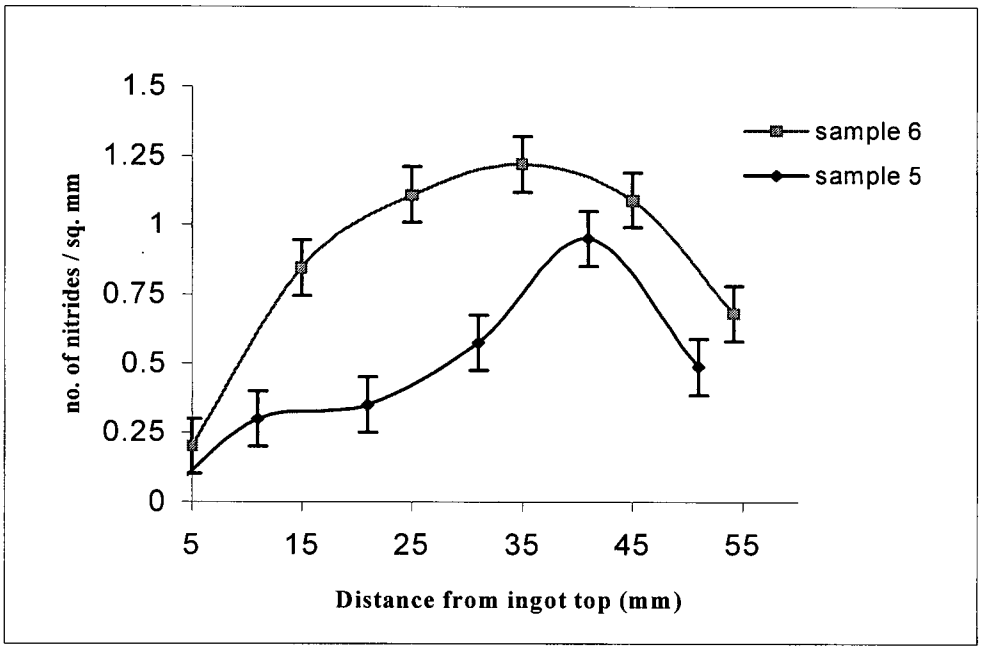

Figure 37. TiN distribution in the DS samples 5 and 6 (64 ppm [N], from the same alloy B) at R = 8.1 μm/sec.

- In the DSQ Sample 3 (48 ppm [N]) and the DS sample 4 (90 ppm [N]), Figure 34 and 36 respectively, most of the nitrides are found to be concentrated around the central portion of the ingot.

- A complete DS on samples 5 and 6, Figure 37 shows that very few nitrides are formed at the top section and virtually no TiN particles are found in the top most portion of the ingot, where the final liquid has solidified. Most of the nitrides are found at a much lower level in the ingot.

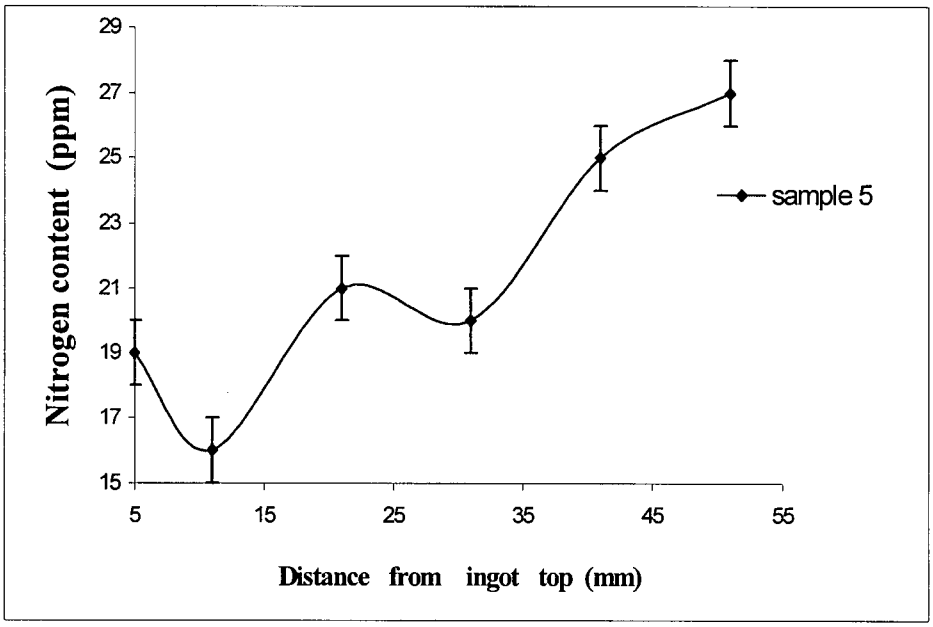

Figure 38. Nitrogen analysis for the DS cast sample 5 (64 ppm [N] at R = 8.1 μm/sec).

- The nitrogen analysis of the DS cast sample 5 (obtained from Special Metals Corp.) is presented in Figure 38. The Y-error bars are about ± 1-2 ppm. It can be seen from the nitrogen analysis graph that there is high nitrogen content at the bottom of the sample rather than the upper portions.

Following these experiments, homogeneous IN718 samples were prepared in order to have a uniform [N] distribution through out the sample. These homogenized samples were subsequently used for further directional solidification experiments.

6.2.2 Homogeneous Sample Preparation

From the earlier results obtained, homogeneous IN718 samples of various nitrogen concentration were prepared in a separate low frequency induction furnace. A schematic of this set up is shown in Figure 33 in section 5.7. The sample is cast into long bars of about 5mm in diameter. A set of high nitrogen content samples (90 ppm [N]) and low nitrogen content samples (20 ppm [N]) were separately cast in the induction furnace. Further DS experiments were carried on these samples at various conditions of pressure and withdrawal rates, as described in the following sub-sections. All the directionally solidified samples were metallographically prepared and the TiN particles were quantitatively assessed.

6.2.3 90 ppm[N] sample DS at 3.5 x 10^{-5} Torr

The 90 ppm [N] content homogeneous samples 7 and 8 were then directionally solidified in the DSQ apparatus at a vacuum of 3.5 x 10^{-5} Torr at two different withdrawal rates of 8.1 μm/sec and 2.4 μm/sec respectively.

a. At a withdrawal rate of 2.4 μm/sec

A metallographic examination of the polished ingot surface indicates a higher TiN concentration at the lower portion of the ingot and a lower TiN concentration at the ingot top. This is presented in Figure 39. There is a corresponding increase in the nitrogen concentration at the bottom of the ingot as presented in Figure 40.

b. At a withdrawal rate of 8.1 μm/sec:

The TiN distribution graphs and the nitrogen distribution graphs are presented in Figure 38 and Figure 40 respectively.

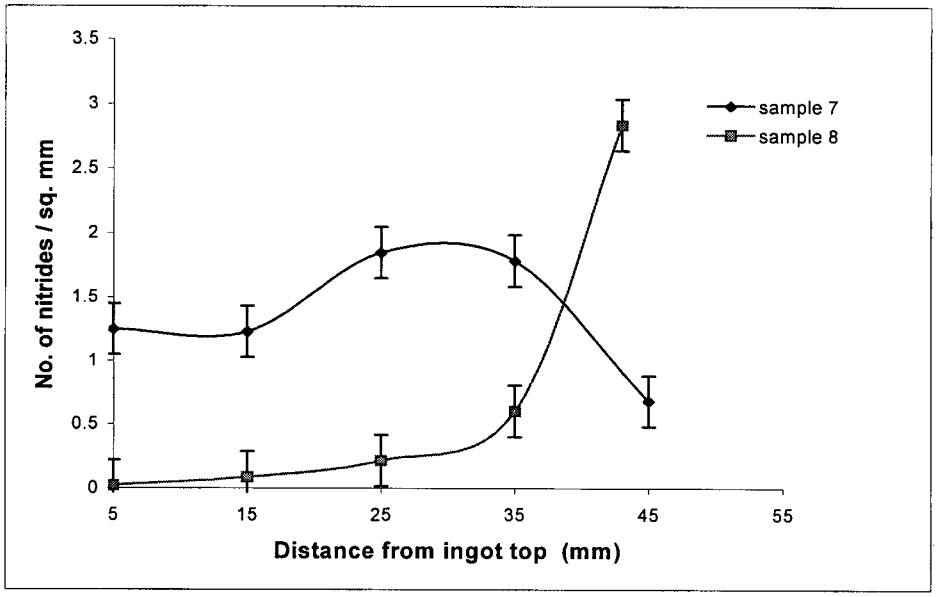

Figure 39. TiN distribution in the 90 ppm [N] content DS cast IN718 ingots. Sample 7 at R = 8.1 μm/sec and sample 8 at R = 2.4 μm/sec.

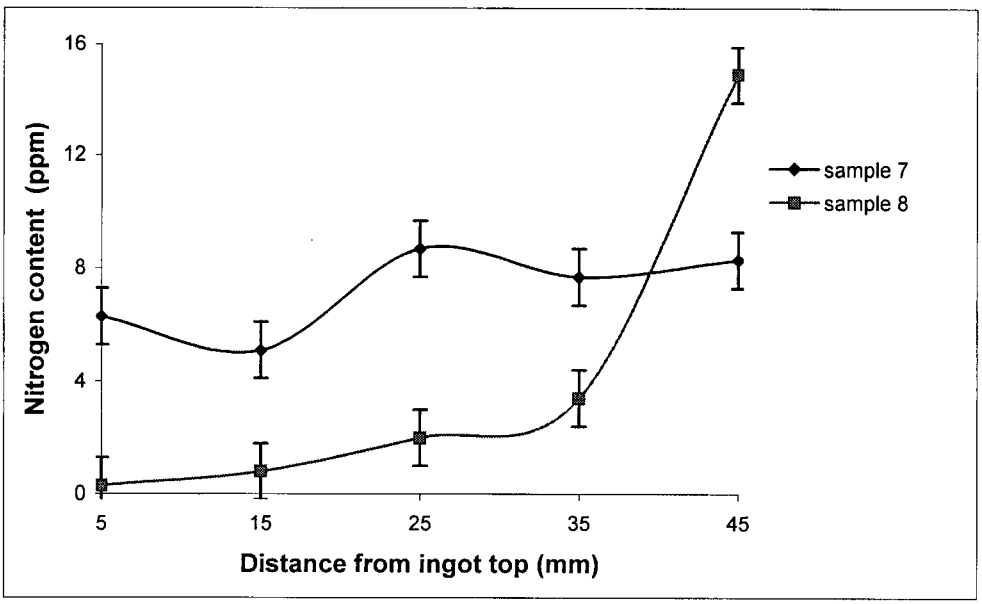

Figure 40. Nitrogen distribution in 90 ppm [N] content IN718 ingots. Sample 7 at R = 8.1 μm/sec and sample 8 at R = 2.4 μm/sec.

From the figures it can be seen that at the lower withdrawal rate (R=2.4 μm/sec), nitrogen content as well as the TiN distribution is very low at the top of the ingot when compared to the bottom. At the higher withdrawal rate (8.1 μm/sec), the nitrogen distribution is almost a constant and there is a slight increase in the TiN density at about 10 to 25 mm from the bottom of the ingot.

6.2.4 90 ppm [N] DS at 100 microns Nitrogen Pressure

To study the TiN precipitation and flotation behavior in a high nitrogen content IN718 alloy, homogeneous 90 ppm [N] content samples were selected. Two sets of experiments were conducted at 100 microns nitrogen pressure at two different withdrawal rates (2.4 μm/sec and 8.1 μm/sec). At a high nitrogen pressure of about 100 microns, the equilibrium nitrogen content was calculated to be 78 ppm (Table 4), which is much higher than the equilibrium nitrogen content for TiN formation (which is 39 ppm).

C. At a withdrawal rate of 2.4 μm/sec :

Samples 11 and 12 were directionally solidified at a withdrawal rate (R) of 2.4 μm/sec. The nitrogen analysis data is presented in Figure 41. It can be seen that there is a high nitrogen concentration in the upper portions of the ingot. The TiN distribution along the ingot is presented in Figure 42. Though the metallographic examination of the ingot reveals a higher TiN concentration at the center of the ingot, large TiN particles > 10 microns in size were found clustered at the very top of the ingot, where the final liquid has solidified. This is presented in Figure 43 (a) and (b). Also, the upper outer surface of the ingot reveals large TiN particles (> 10 microns in size) and clusters of TiN particles sticking to it, as presented in Figure 44 (a), (b) and (c).

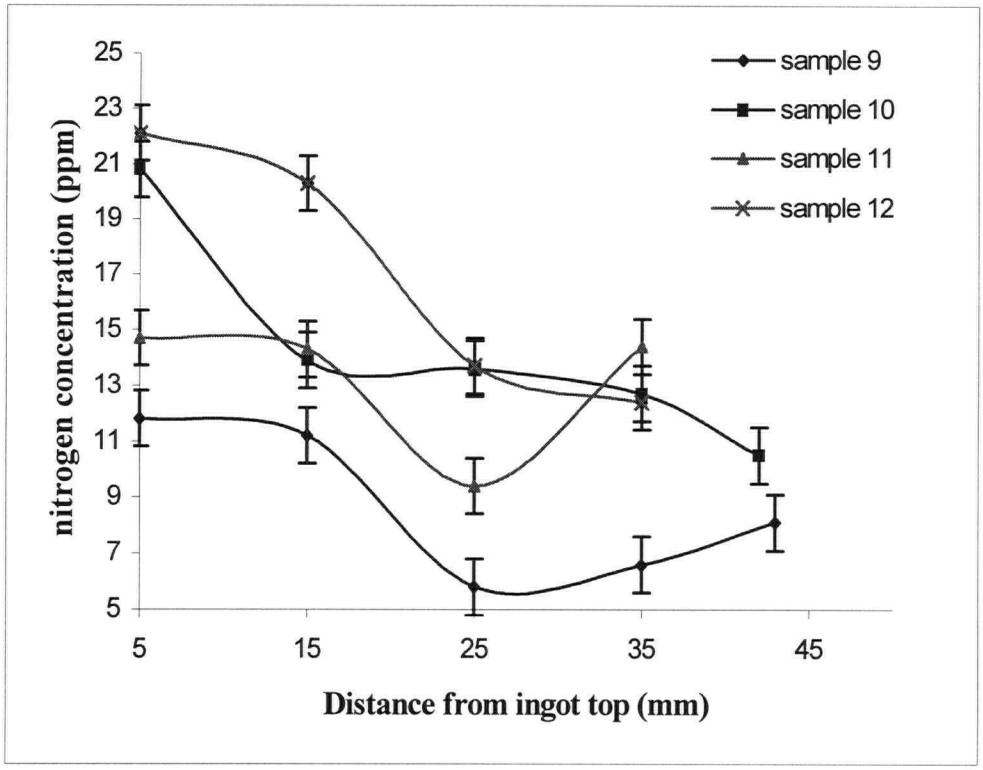

Figure 41. Nitrogen distribution in the 90 ppm [N] content IN718 ingots directionally solidified at 100 microns nitrogen pressure. Sample 9 and 10 at R = 8.1 μm/sec and sample 11 and 12 at R = 2.4 μm/sec.

D. At a withdrawal rate of 8.1 μm/sec :

The TiN distribution along the ingot is presented in Figure 42. A similar observation in the TiN distribution was made here as in the case (c). Large TiN particles were found at the very top of the ingot as presented in Figure 43 (a) and (b). The nitrogen distribution along the ingot is presented in Figure 41. From the graph it can be seen that the nitrogen concentration at the upper portions of the ingots is higher than that in the lower portions.

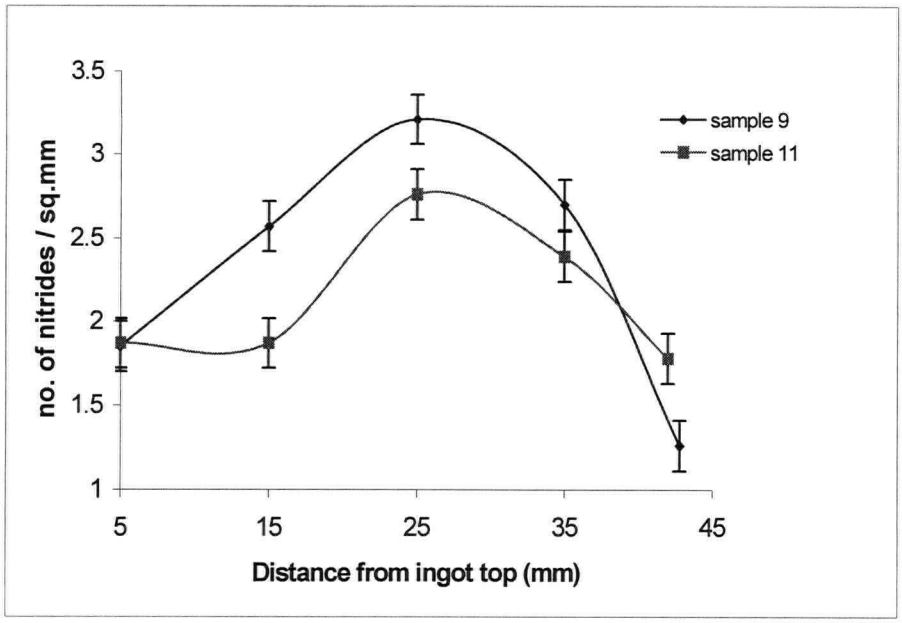

Figure 42. TiN distribution in the 90 ppm [N] content IN718 samples directionally solidified at 100 microns nitrogen pressure. Sample 9 at R = 8.1 μm/sec and sample 11 at R = 2.4 μm/sec.

(a)

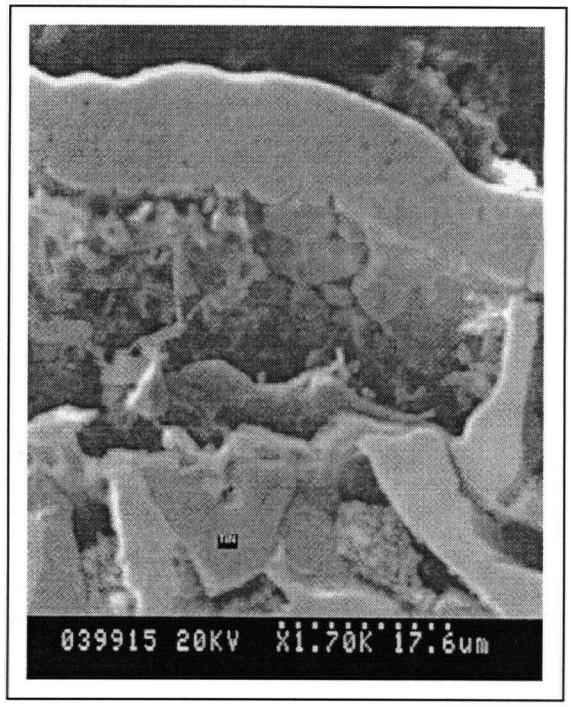

(b)

Figure 43 (a) and (b) Etched sections from DS samples (90 ppm [N]) showing TiN particles of the very top of the ingot

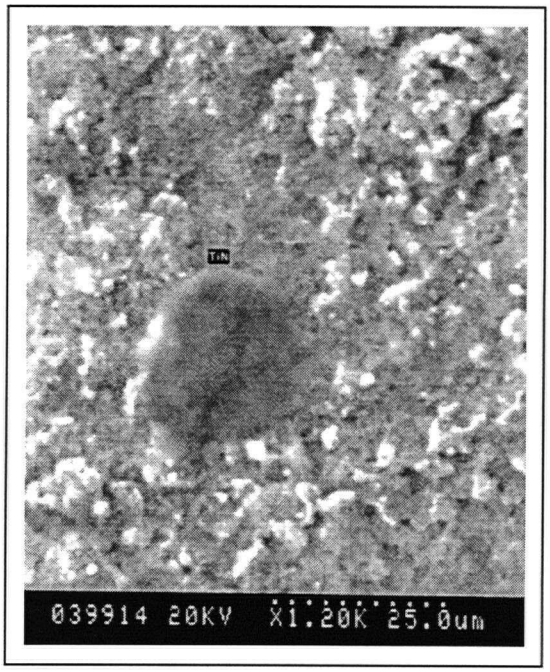

(a)

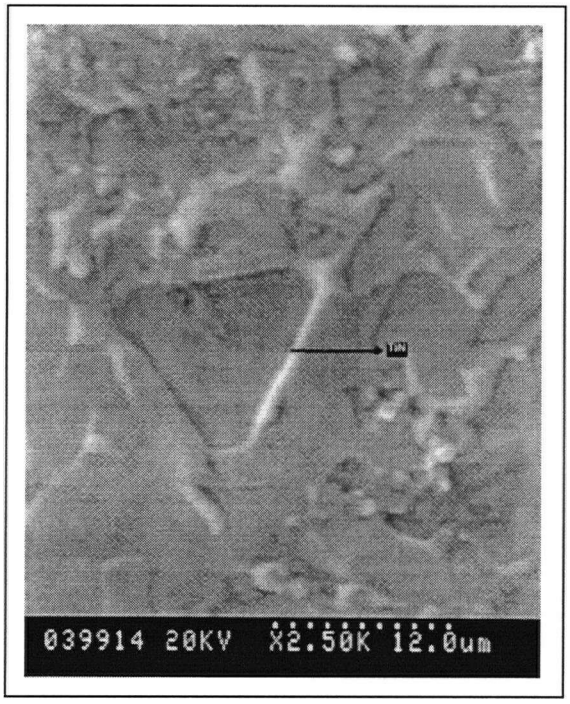

(b)

(c)

Figure 44. (a), (b), and (c) TiN particles on the upper outer surface of the ingot.

6.2.5 90 ppm [N] Sample DS at 400 microns Nitrogen Pressure

Directional solidification experiments were conducted with sample 13 (90 ppm [N] content) at a withdrawal rate of 8.1 μm/sec. under a nitrogen pressure of 400 microns. After metallographic analysis of TiN distribution in the sample, it was sent out for nitrogen analysis.

At a nitrogen pressure of 400 microns, the equilibrium nitrogen concentration was found to be 156 ppm (Table 4). The nitrogen analysis for the ingot is presented in Figure 45. This figure indicates a high nitrogen concentration at the upper portion and a low nitrogen concentration at the bottom of the ingot. The TiN distribution (presented in Figure 46) is consistent with the nitrogen analysis result. Also, large number of TiN particles of size > 10 microns were found at the very top of the ingot where the final liquid had solidified.

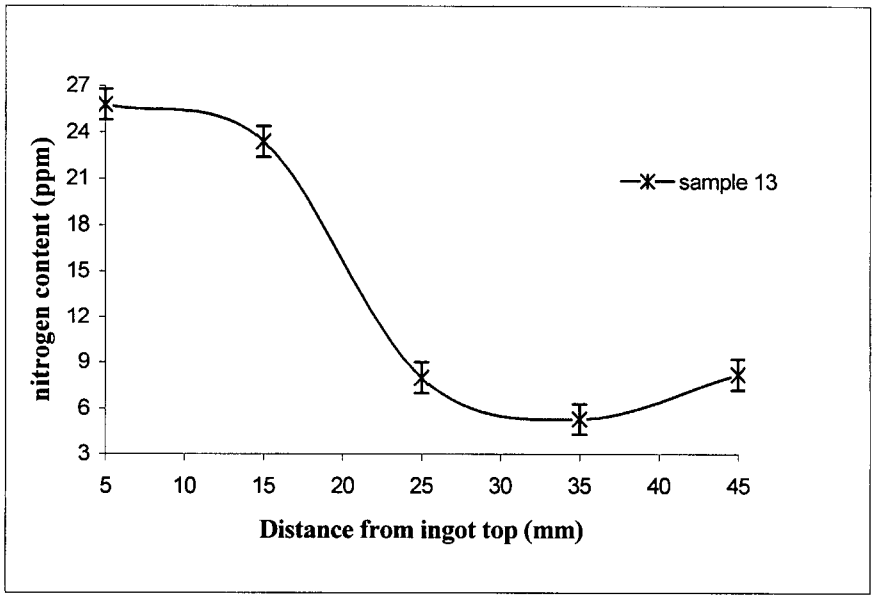

Figure 45. Nitrogen distribution along sample 13 (90 ppm [N] content) directionally solidified at 400 microns nitrogen pressure at a withdrawal rate of 8.1 μm/sec.

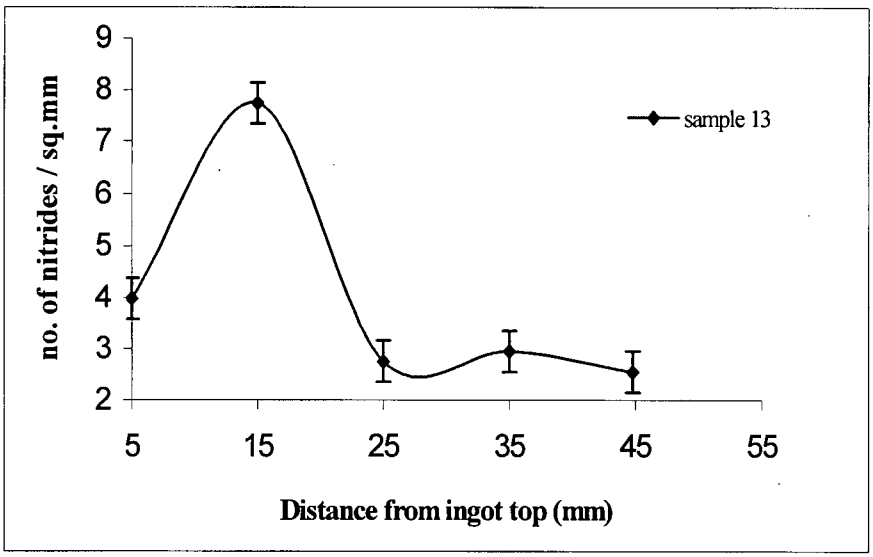

Figure 46. TiN distribution along sample 13 (90 ppm [N] content) directionally solidified at 400 microns nitrogen pressure at a withdrawal rate of 8.1 μm/sec.

(a)

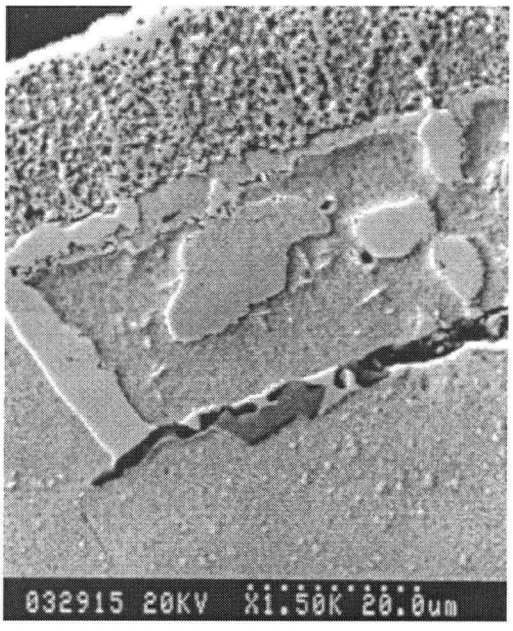

(b)

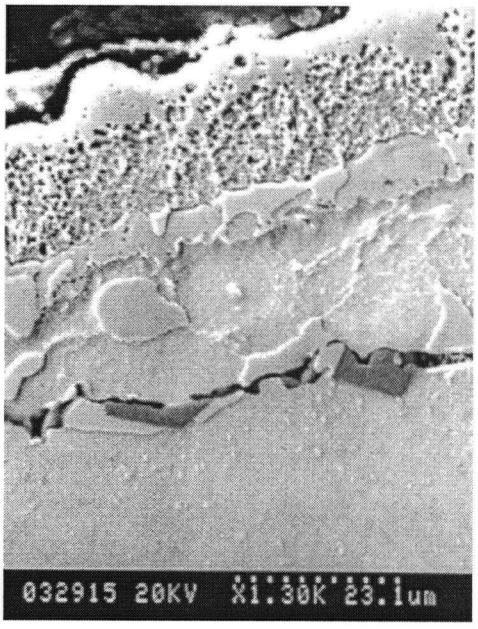

(c)

Figure 47. (a), (b), and (c) SEM pictures of the top section of sample 13 showing large TiN particles.

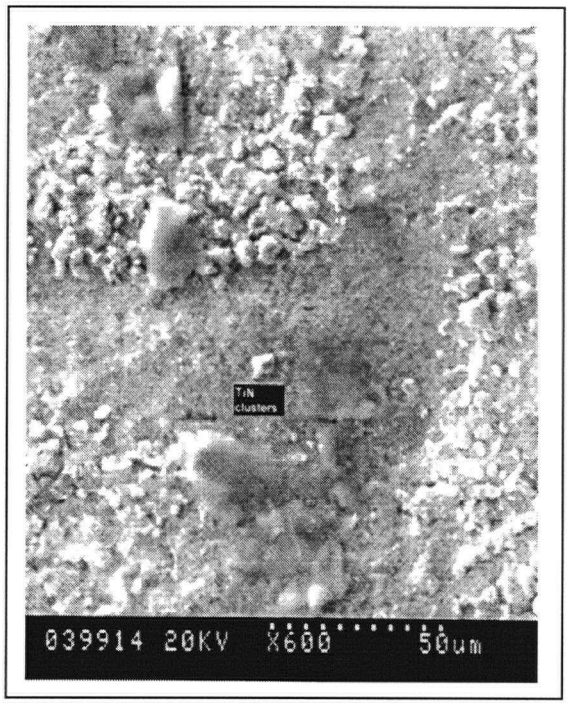

(a)

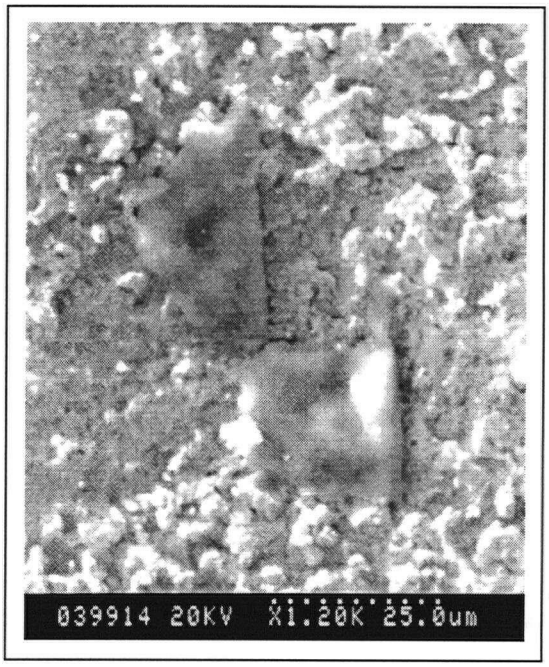

(b)

Figure 48. (a) and (b) TiN clusters on the outer surface of the DS cast sample 13 (90 ppm [N]).

This is shown in Figure 47 (a), (b) and (c). An examination of the outer upper surface of the ingot indicates large TiN particles and TiN clusters sticking to it. Figure 48 (a) and (b) are some SEM pictures of the TiN clusters adhering to the outer wall of the DS cast ingot.

6.2.6 DS Experiments With 20 ppm [N] Samples

The 20 ppm sample was selected to understand the TiN precipitation behavior in a low nitrogen content sample. Two arbitrary values for nitrogen pressure were selected 40 microns and 10 microns. The two conditions were selected such that the equilibrium nitrogen contents at these pressures are above and below the equilibrium nitrogen content for TiN formation i.e. 39 ppm. The equilibrium nitrogen concentration at a nitrogen pressure of 40 microns was calculated to be 49 ppm and the equilibrium nitrogen concentration at the nitrogen pressure of 10 microns was calculated to be 24 ppm. (please refer to Table 4).

E. At a withdrawal rate of 2.4 μm/sec, and at 40 microns nitrogen pressure:

Two separate experiments were conducted on IN718 ingots with 20 ppm [N] content. Samples 14 and 15 were directionally solidified at a nitrogen pressure of 40 microns and at a withdrawal rate of 2.4 μm/sec. After metallographic observations, the samples were sent out for nitrogen analysis. Figures 49 and 50 present the nitrogen concentration and the TiN distribution in the ingots. The nitrogen analysis, as well as the TiN distribution indicate a higher concentration at the upper portions of the ingot. Large TiN particles (> about 10 microns) were found at the very top of the ingot as presented in Figure 51 (a), (b), (c) and also on the outer walls of the ingot.

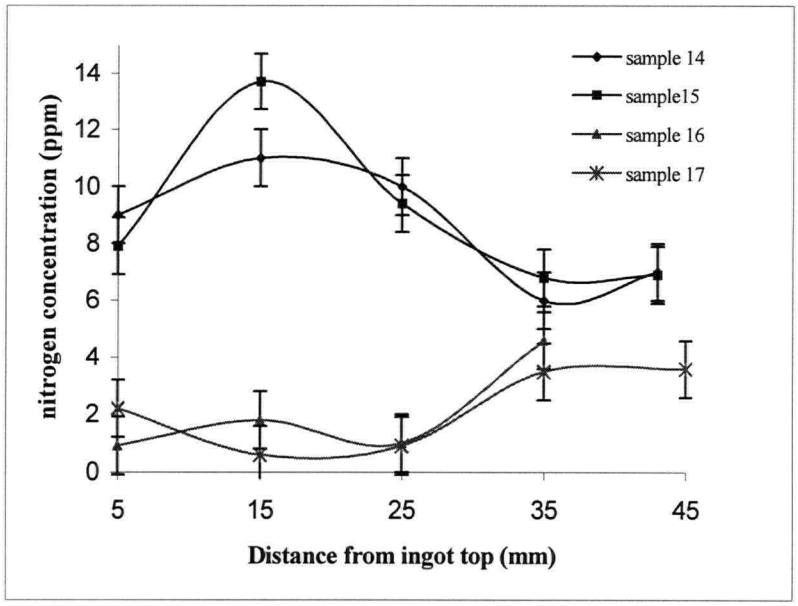

Figure 49. Nitrogen distribution along the 20 ppm [N] directionally solidified ingots at a withdrawal rate of 2.4 μm/sec. Sample 14 and 15 were DS at a nitrogen pressure of 40 microns and samples 16 and 17 were DS at a nitrogen pressure of 10 microns.

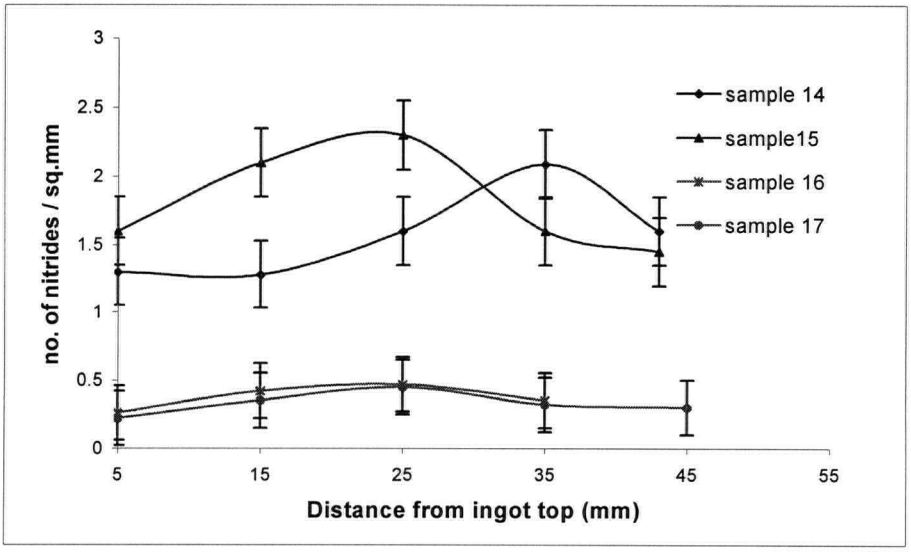

Figure 50. TiN distribution along the 20 ppm [N] directionally solidified ingots at a withdrawal rate of 2.4 μm/sec. Sample 14 and 15 were DS at a nitrogen pressure of 40 microns and samples 16 and 17 were DS at a nitrogen pressure of 10 microns.

F. At a withdrawal rate of 2.4 μm/sec at a nitrogen pressure of 10 microns:

The overall nitrogen concentration and TiN distribution is more or less a constant through out the DS ingot as presented in Figures 49 and 50. No TiN inclusions were found at the top most portions of the sample and on the outer walls.

(a)

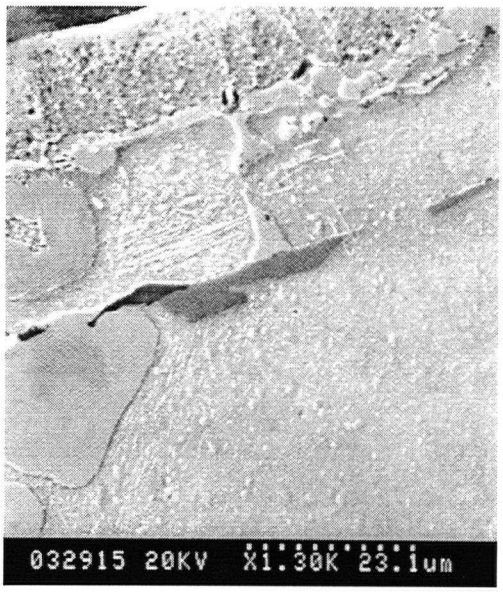

(b)

(c)

Figure 51. (a), (b), and (c) TiN particles found at the very top of the DS ingot (20 ppm [N], at 40 microns nitrogen pressure).

Chapter 7: Discussions

7.1 Directional Solidification And Quenching Experiments

The results from the directional solidification and quenching (DSQ) experiments performed on samples 1(67 ppm [N]), 2(64 ppm [N]), 3(48 ppm [N]) indicate there is a high probability that a combination of such low pressures and high temperature causes severe degassing of the nitrogen from the ingot. Hence, the upper portions of the ingot are depleted of the nitrogen content. Consequently, there is no TiN formation in these regions.

There is also a possibility that the TiN particles dissolve (undergo re-solutioning) at such high temperatures above the liquidus and precipitate at lower temperatures during solidification.

The carbon content in the solidifying ingot is found to affect TiN precipitation. While a lower carbon content (.008 wt % in sample 3 (48 ppm [N])) promotes the precipitation of TiN particles, a higher carbon content (.03 wt% in sample 1 (67 ppm [N]) and sample 2 (64 ppm [N])) favors carbonitride formation. In the case of single crystal alloys, since they have very low carbon content one would anticipate the same "pure" nitride formation effect.

7.2 Directional Solidification (DS) Experiments

Directional solidification experiments carried out on sample 3(48 ppm [N]) and sample 4 (90 ppm [N]), indicate a higher TiN concentration at the center of the ingot. This is probably due to an experimental artifact that there is a high probability that the Cr_2N had not homogenized (due to a lack of a stirring action in the induction furnace) and had remained around the central region of the ingot where it was placed.

From the DS experiments on samples 5 and 6 (64 ppm [N]) content, it is clear that flotation is not affected. If the buoyancy effects did affect TiN flotation as assumed, then in

principle TiN particles (at least those > 6μm) should have been found at the top of the ingot, where the final liquid has solidified. Since the samples have a high nitrogen content (about 64 ppm), it needs to be established experimentally that either the TiN are not all at the top, or stuck on the outer surfaces of the sample. Also, if the TiN particles are indeed influenced by buoyancy forces and obey Stokes' law, a lower withdrawal rate (< 6 μm/sec, as determined for a typical TiN particle with a size of about 6 microns) should be able to affect such a flotation.

DS Experiments at 3.5 x 10^{-5} Torr

Directional solidification experiments on homogeneous 90 ppm [N] content samples 7 and 8, conducted in a high vacuum, indicate that during solidification a combination of high temperature and low pressure leads to heavy degassing of nitrogen from the upper portions of the ingot. Hence, there is a low nitrogen concentration and a corresponding lower TiN concentration in the upper portions of the ingot.

The importance of nitrogen gas in promoting the formation of TiN inclusions is evident from the above results. The theoretical calculation for the equilibrium nitrogen content required for the formation of TiN particles in alloy IN718 (as discussed in chapter 4) has claimed a value of 39 ppm [N] content at the liquidus temperature. At a pressure of 3.5 x 10^{-5} Torr(4.5 x 10^{-8}atm) and at the liquidus temperature of 1340 ^{0}C, the $[N]_{eqm}$ falls to a very low value of 1.4 ppm (Table 4).

DS Experiments under Nitrogen Pressure

In the DS experiments on the 90 ppm [N] content samples 9-12, conducted under a nitrogen pressure of 100 microns nitrogen pressure, the calculated equilibrium nitrogen concentration is about 78 ppm at T_{liq}. Hence, there is a heavy TiN precipitation. There is flotation of TiN particles that were precipitated in the liquid alloy, as can be seen from Figure 41. Larger TiN particles > 10 microns in size are able to float out and get accumulated on the top of the ingot. This is

because, they have a velocity of rise > about 28 μm/sec (calculated using the Stokes principle), which is an order higher than the withdrawal rate (2.4 μm/sec) used in the experiments. Though the nitrogen content at the very bottom of the samples 9 and 11 is high, the corresponding TiN distribution (from Figure 42) is low. If there were smaller TiN particles (<about 3 microns in size) sticking to the outer walls of the ingot at the bottom, it was not possible to observe them under the SEM. There may be a possibility that very small TiN particles could be sticking to the outer wall of the ingot at the bottom, which could have contributed to the increase in the [N] content.

At a nitrogen pressure of 400 microns, the equilibrium nitrogen concentration was found to be 156 ppm (Table 4). Figures 45 and 46, indicate a flotation of TiN particles precipitated in the liquid. Also, at such high nitrogen pressure there is a possibility of nitrogen pick-up from the atmosphere, which could have partially contributed to an increase in the nitrogen content at the very top of the ingot.

The 20 ppm sample was selected to understand the TiN precipitation behavior in a low nitrogen content sample. At a nitrogen pressure of 40 microns, the equilibrium nitrogen content is determined to be 49 ppm (at T_{liq}). In the segregation zone, due to the combined effects of temperature, segregation of Ti and nitrogen, TiN solubility decreases. The observed flotation is due to the precipitated equilibrium titanium nitrides in the liquid. As seen from the Figures 49, and 50 none of the TiN particles precipitated in the solid/liquid mushy region exhibit flotation.

At a nitrogen pressure of 10 microns, the calculated equilibrium nitrogen content is 24 ppm. This value is below the equilibrium nitrogen content required for the formation of TiN particles, which is about 39 ppm. Hence, the overall nitrogen concentration and TiN distribution is very low and more or less constant through out the DS ingot as presented in Figures 49 and 50. Due to a decrease in the nitrogen content, there is a corresponding reduction in the TiN precipitation.

7.3 Summary of TiN distribution and Nitrogen analysis

The nitrogen analysis and TiN distribution for samples 7 through 17 are presented in the following graphs. Figures 52, and 53 present the TiN distribution and nitrogen distribution along the DS cast 718 samples 7 through 17 at withdrawal rate of 2.4 μm/sec respectively. The TiN distribution and nitrogen distribution along these samples at a withdrawal rate of 8.1 μm/sec are presented in Figures 54 and 55.

Figures 52 and 53 indicate that in samples 11, and 12 (which are 90 ppm [N] content samples, DS at 100 microns nitrogen pressure) there is some flotation of TiN particles precipitated in the liquid. The equilibrium nitrogen content at this pressure is determined to be about 78 ppm at T_{liq}. Where as, in Figure 53, samples 14 and 15 (which are 20 ppm [N] content samples DS at 40 microns nitrogen pressure), indicate no such flotation exhibited by TiN particles precipitated in the solid/liquid mushy region.

A similar TiN flotation effect can be observed in sample 13 (90 ppm [N], DS at 400 microns nitrogen pressure), as presented in Figure 55. The equilibrium nitrogen content at this pressure is determined to be about 156 ppm at T_{liq}. Though it is evident that there is flotation of TiN particles precipitated in the liquid, there is a high probability that there may be some nitrogen pick-up from the atmosphere at such high nitrogen pressures.

Nitrogen Distribution:

An interesting observation from the nitrogen analysis graphs 53 and 55 is that, although the equilibrium nitrogen contents of the samples 11-15 are high, the final nitrogen content is much reduced. The final ingots invariably exhibit a net reduction in nitrogen content. A possible explanation is as follows: There are two significant processes taking place during solidification

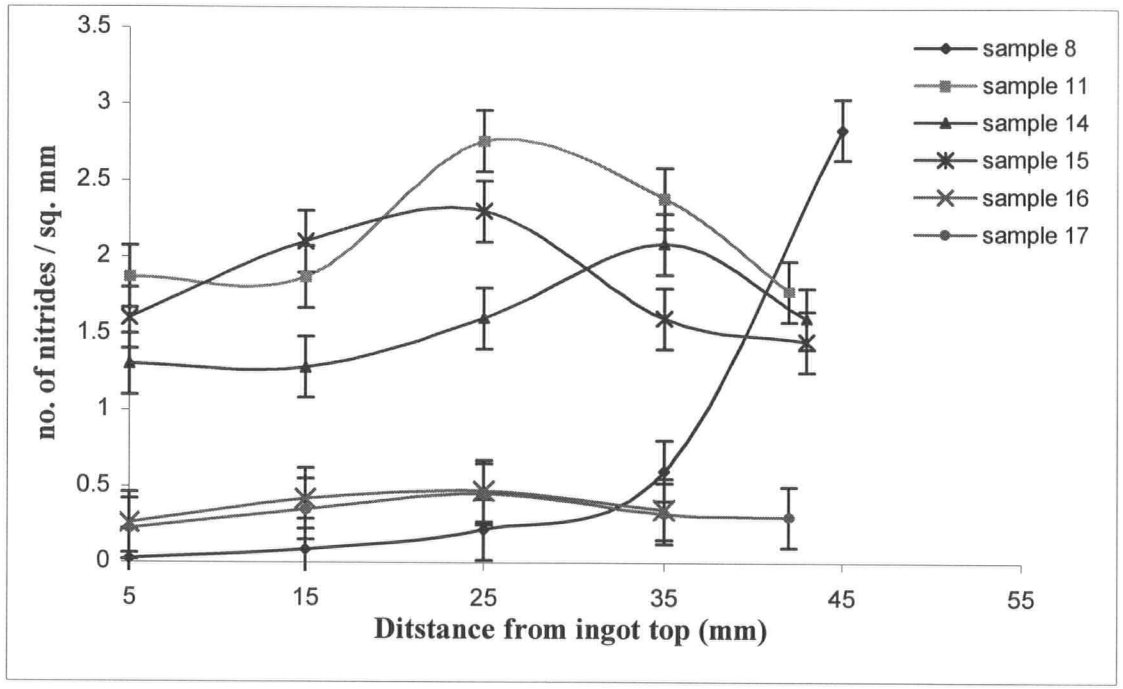

Figure 52. Distribution of TiN along the DS cast IN718 ingots at a withdrawal rate of 2.4 μm/sec.

Sample 8 : 90 ppm [N], at 3.5 x 10^{-5} Torr

Sample 11: 90 ppm [N], at 100 microns nitrogen pressure

Sample 14: 20 ppm [N], at 40 microns nitrogen pressure

Sample 15: "

Sample 16: 20 ppm [N], at 10 microns nitrogen pressure

Sample 17: "

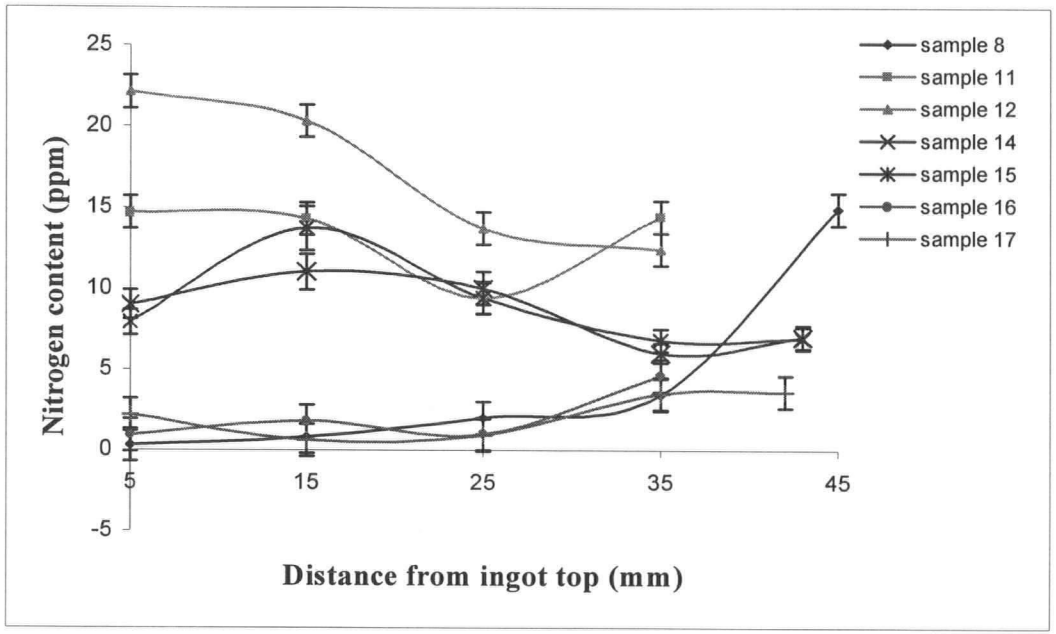

Figure 53. Distribution of nitrogen along the DS cast IN718 ingots at a withdrawal rate of 2.4 μm/sec.

Sample 8 : 90 ppm [N], at 3.5 x 10^{-5} Torr

Sample 11: 90 ppm [N], at 100 microns nitrogen pressure

Sample 12: "

Sample 14: 20 ppm [N], at 40 microns nitrogen pressure

Sample 15: "

Sample 16: 20 ppm [N], at 10 microns nitrogen pressure

Sample 17: "

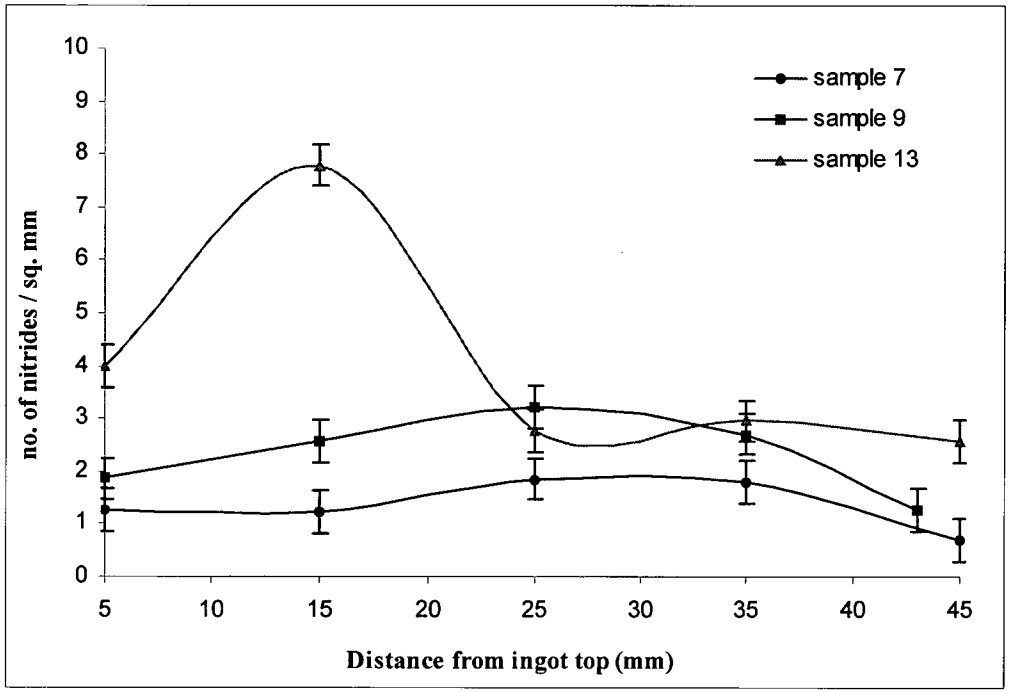

Figure 54. Distribution of TiN along the DS cast IN718 ingots at a withdrawal rate of 8.1 μm/sec.

Sample 7 : 90 ppm [N], at 3.5 x 10^{-5} Torr

Sample 9 : 90 ppm [N], at 100 μ nitrogen pressure

Sample 13: 90 ppm [N], at 400 μ nitrogen pressure

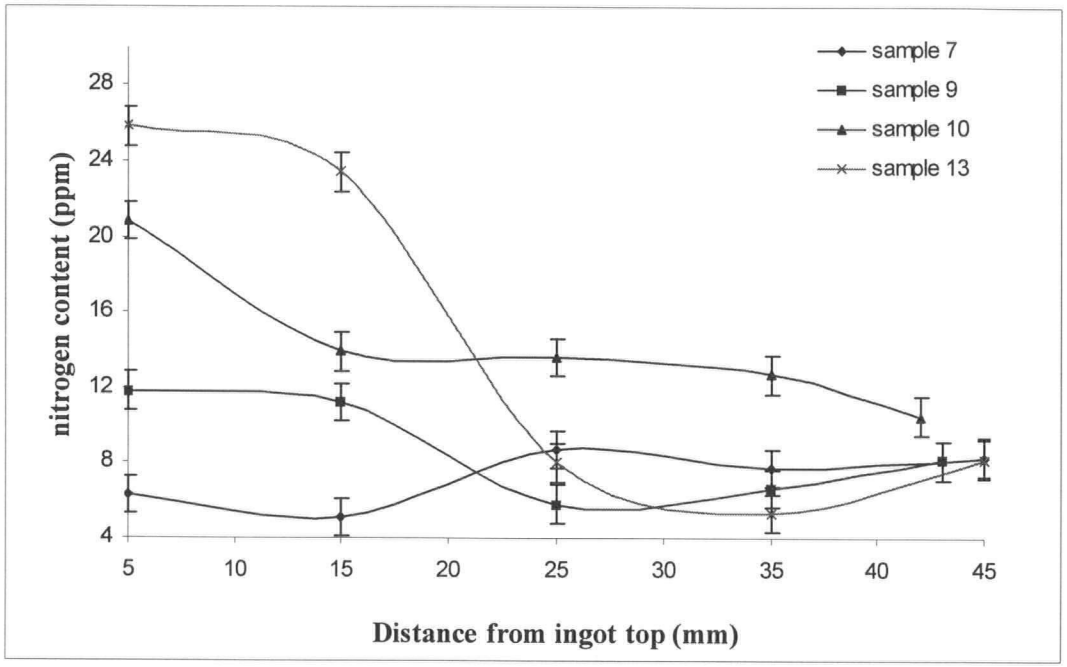

Figure 55. Distribution of nitrogen along the DS cast IN718 ingots at a withdrawal rate of 8.1 μm/sec.

Sample 7 : 90 ppm [N], at 3.5×10^{-5} Torr

Sample 9 : 90 ppm [N], at 100 μ nitrogen pressure

Sample 10: 90 ppm [N], at 100 μ nitrogen pressure

Sample 13: 90 ppm [N], at 400 μ nitrogen pressure

namely, a). segregation of Ti and nitrogen (in the solid/liquid mushy region) and b) rejection of nitrogen into the bulk liquid.

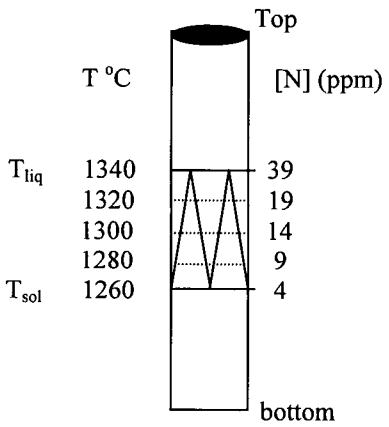

Figure 56. Equilibrium nitrogen contents required for the formation of TiN in the l/s mushy region at different temperatures, accounting for Ti segregation.

Figure 56 presents a schematic of IN718 ingot during directional solidification with the corresponding equilibrium nitrogen contents required for the formation of TiN, in the solid/liquid region of the DS ingot. Below the liquidus, the TiN solubility decreases as presented in Table 6 and Figure 56 (due to temperature effects as well as segregation of Ti and nitrogen). Above the liquidus temperature, the solubility of TiN increases as presented in Table 5.

Assuming that the liquid alloy is stationary (no liquid flow), the diffusion of nitrogen can be given by the equation:

$$\Delta z = \sqrt{Dt} \tag{37}$$

Where, D = Diffusion coefficient ($\approx 10^{-5}$ cm^2/sec). Substituting the value of D in the above equation, the diffusion rate was found to be about 31.6 μm/sec. This value is considerably higher than the present withdrawal rates (2.4 μm/sec and 8.1 μm/sec). Therefore, nitrogen is rejected

into the bulk liquid during solidification. As solidification proceeds, the bulk liquid becomes richer in nitrogen and there is heavy TiN precipitation just above the liquidus. A schematic of this process is presented in Figure 57 (a).

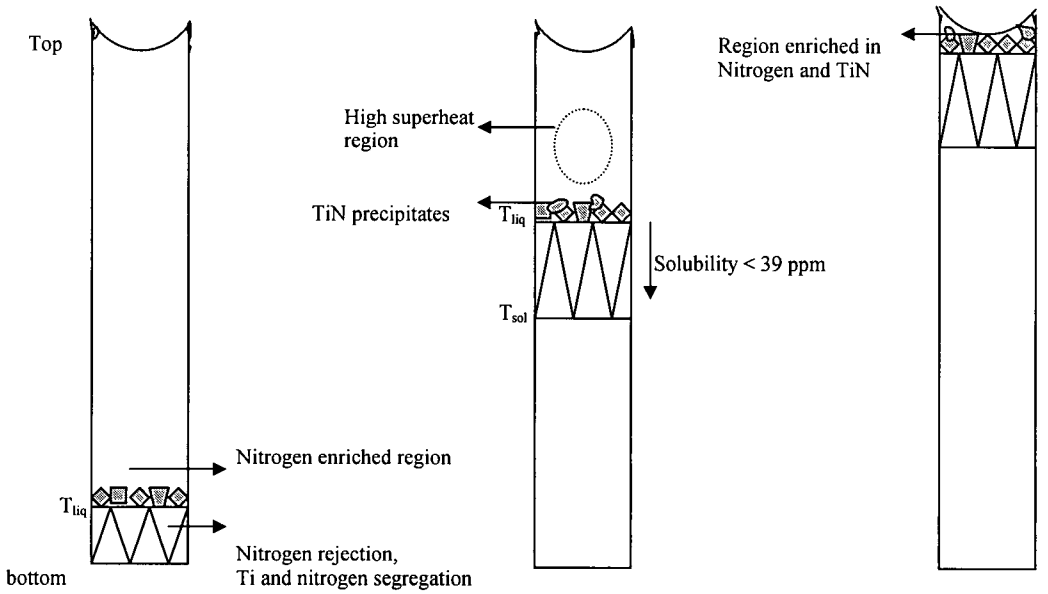

Figure 57 (a) Initial stage during D.S (dendrites are beginning to form) (b) intermediate stage, and (c) final stage of D.S.

Figure 57 (b) presents a schematic of the solidification process in the intermediate stage, where the dendrites are fully grown. Due to a combination of a) Ti and nitrogen segregation and b) rejection of nitrogen, there is a decrease in TiN saturation solubility from the tip to the base of the dendrites in the solid/liquid mushy region. This facilitates TiN precipitation in the mushy region. Above the liquidus, there is TiN precipitation. These particles have sufficient time to grow into larger particles and float. Well above the liquidus, there is dissolution of the TiN particles due to the high superheat in these regions. The TiN particles are re-precipitated later during solidification (at lower temperatures).

As solidification progresses, the bulk liquid is continuously enriched in nitrogen. There is continuous rejection of nitrogen into the atmosphere. Hence, there is a nitrogen "sink" established above the solidifying ingot. The final portion to solidify is enriched in nitrogen and TiN precipitates, as presented in Figure 57 (c). These are the TiN particles that were precipitated above the liquidus during solidification, which had sufficient time to grow into large particles. Below the final portion to solidify, the nitrogen concentration is well below the solubility limit at T_{liq} (i.e. < 39 ppm). In the process of nitrogen analysis, each portion was ground on all sides and the top in order to determine the nitrogen concentration. There is a high possibility that if the final portion of the ingot is lopped off, the nitrogen-enriched portion may be lost and the analysis shows the nitrogen distribution below the final portion to solidify, which has a lower nitrogen distribution.

In this study, the thermodynamic equations describing the solubility of nitrogen, and formation of TiN in iron alloys have been applied to IN718 alloy system. The available data for the first order interaction parameters for nitrogen and titanium with various elements in steel were directly applied to alloy IN718. This data was then used to calculate critical values like the activity coefficient of nitrogen and that of titanium in alloy IN718. Hence, there is a possibility that the initial value for the equilibrium nitrogen content for the formation of TiN thus calculated might be incorrect, which could account for the apparent reduction in nitrogen content observed in the final DS IN718 ingots.

The nitrogen concentration at various portions of the ingot during solidification can be calculate using the Scheil equation:

$$C_s = kC_0 (1-f_s)^{k-1} \tag{38}$$

At this point, the phase diagram for nickel-nitrogen is not available in literature and hence the value for the partition coefficient is unknown. To roughly understand the nitrogen distribution along the ingot, the value of partition coefficient for nitrogen was calculated using the physical

data from the present experiments. Using the data from sample 11 (90 ppm [N] content sample DS at 100 microns nitrogen pressure),

$$k = C_s/C_l \tag{39}$$

where, C_s = the solute concentration in the solid (10 ppm [N]), C_l = solute concentration in the liquid (80 ppm [N]). Hence, the partition coefficient was found to be about 0.125. This value for k was substituted in equation 38.

Figure 58 presents the distribution of nitrogen along the ingot. This graph is superimposed on the nitrogen distribution graphs for samples 11 and 12. As the value of k is decreased, the Scheil equation is found to fit the nitrogen curves determined by the present experiments. Hence, it can be speculated that the partition coefficient of nitrogen in alloy IN718 would be less than 0.1.

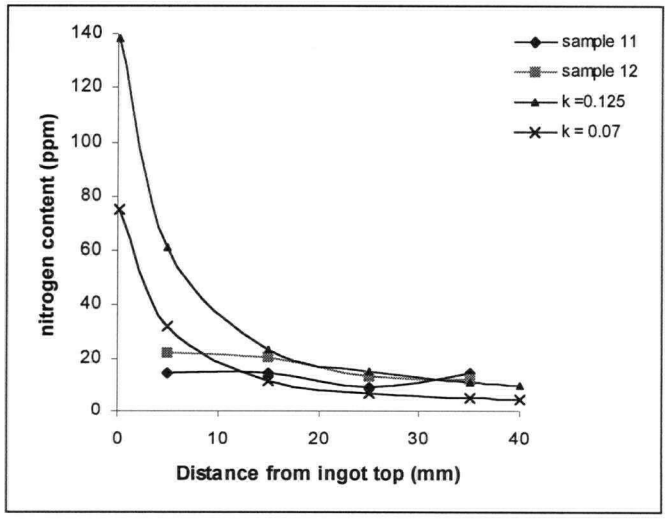

Figure 58. Nitrogen distribution along the DS samples at various k values for nitrogen.

It is to be noted that studies by Bower et. al. [73] on Al-4.5%Cu alloys have revealed that at sufficiently high thermal gradients and low withdrawal rates (which are similar to the casting

conditions used in the present studies) there is significant bulk diffusion of the solute. In this case, the composition vs. fraction solidified is given by the modified Scheil expression :

$$C_s^* = kC_o\left[\frac{a}{k-1}+\left(1-\frac{ak}{k-1}\right)(1-f_s)^{k-1}\right] \quad (40)$$

Where

$a = G_l D_l / C_o R m_l$

D_l = diffusion coefficient in liquid

G_l = thermal gradient

R = withdrawal rate

m_l = slope of the liquidus (from the phase diagram)

Hence, by substituting the casting parameters from the present experiments and the appropriate values for parameters 'a' and 'k'(which at this point are not available), a better fit for nitrogen distribution along the DS ingot could be obtained.

To summarize, in-spite of a high equilibrium nitrogen content in samples 11 - 15 the net reduction in the nitrogen content of the final DS ingots may be due to the following reasons: a) segregation of Ti and nitrogen in the solid/liquid mushy region, b). rejection of nitrogen into the bulk liquid, c). grinding off the final portion of the ingot, which is enriched in nitrogen and TiN during nitrogen detection, and d). a possible error (if any) in determining the equilibrium nitrogen content required for the formation of TiN in alloy IN718, since the thermodynamic data for nitrogen solubility and TiN formation in iron alloys have been directly applied to IN718 alloy system.

7.4 TiN Particle Distribution

From Experiments (c) sample 11 (90 ppm sample, at 2.4 μm/sec and 100 microns nitrogen pressure), and (f) sample 14 (20 ppm sample at 2.4 μm/sec and 40 microns nitrogen pressure), the TiN particle size distribution were studied along the DS ingots. At various distances from the top of the ingot, the largest TiN particles were selected and their size were measured in the SEM. Figure 59 is a graphical presentation of the TiN particle distribution along the DS ingots.

The following observations are made from Figure 59:

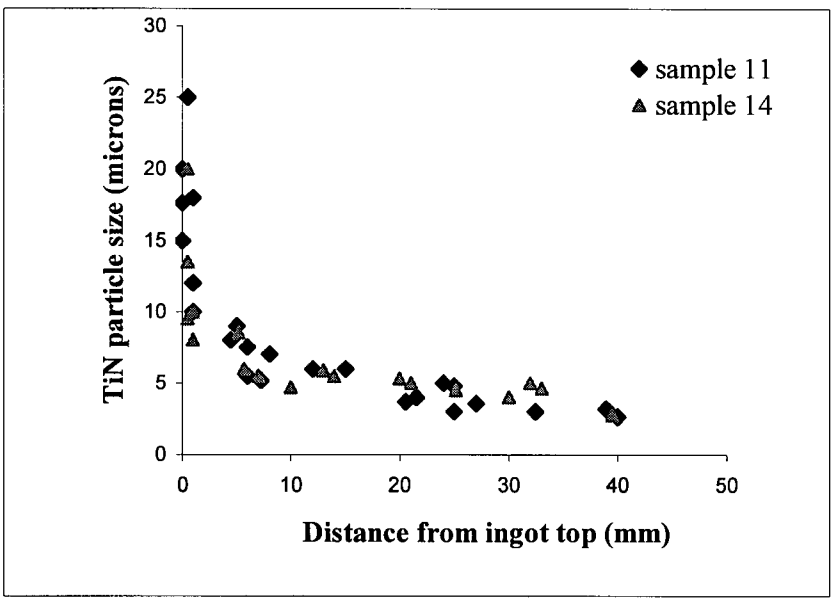

Figure 59. TiN particle distribution along the directionally solidified IN718 ingots. Data are from the following samples: 90 ppm [N] samples DS cast at 100 microns nitrogen pressure - sample 11 (at R = 2.4 μm/sec) and 20 ppm [N] content sample 14 directionally solidified at a nitrogen pressure of 40 microns, at R = 2.4 μm/sec.

- TiN particles larger than about 9 microns are found at the very top of the ingot. Particles as big as 25 microns were observed in this region. The velocity of rise of the particles is > 28 μm/sec, which is much higher than the withdrawal rates of 8.1 μm/sec or 2.4 μm/sec. Hence

it can be concluded that the buoyancy effect does cause flotation of TiN particles greater than at least 10 microns. These large TiN particles are the ones precipitated in the liquid that had sufficient time to grow and which exhibit flotation.

- From about 5 to 35 mm from the top, the TiN particle size varies from 8 microns to 4 microns such that, the bigger particles are found towards the upper portions and the smaller particles are more towards the lower end. The velocity of rise of these particles ranges from 18 μm/sec to 4.5 μm/sec respectively (From Table 10). Though there is indication of flotation, it is not much pronounced in this case. At this point it appears that this withdrawal rate is still insufficient to cause a complete flotation of particles < about 8 microns.

- Below about 35 mm from the top of the ingot, TiN particles < 4 microns are predominant. The velocity of rise of these particles is < 4μm/sec, which is very close to the withdrawal rates used in the experiments. Also, the viscous drag on these particles is large and this may be responsible in causing this "sinking" effect. These TiN particles may be the ones that are precipitated later during solidification in the solid/liquid mushy region.

Chapter 8: Conclusions and Recommendations

8.1 Summary

The principal aim of this work was to study the behavior of TiN particles during the directional solidification in alloy IN718 and establish whether the TiN particles could have any influence on random grain formation. The literature review indicate that random grain formation in many single crystal turbine blades is found to occur even without any drastic changes in the casting conditions, which were earlier determined to be the principal contributing factors towards random grain formation. No quantitative work has been done in this problem and the relative importance of the source for secondary grains is yet to be established.

In casting single crystal superalloy turbine blades, it is found that the platform supercools by several degrees. Experiments conducted on SC-16 turbine blades have indicated that the mold withdrawal rate directly affects the undercooling produced. Undercoolings of up to 40K have been produced in these experiments [38]. According to the Turnbull-Vonnegut theory, a lattice disregistry of $< 20\%$ between the matrix and the precipitate is then required for the precipitate to act as a stable heterogeneous nuclei. Taking into account the lattice disregistry between the FCC nickel matrix (in Ni-based superalloys) and the different inclusions, it has been established that the TiN inclusions have a lattice disregistry of about 16.8% and would act as a nuclei at an undercooling of about 19 ^{0}C. Hence, TiN particles can be potential heterogeneous nuclei in Ni-based superalloys.

The DS experiments have concluded that under certain conditions the TiN particles are stable in the liquid alloy ahead of the solidification front (above the liquidus). Therefore, there is a high possibility that the TiN particles can act as potential heterogeneous nuclei for random grain formation in these alloys.

1. Conditions Required for the Formation of TiN

The equilibrium nitrogen concentration required for the formation of TiN particles in alloy IN718 was calculated to be 39 ppm (at 1340 °C) using the available thermodynamic data. Figure 60 is a graphical presentation of TiN saturation solubility ahead of the liquidus in the present studies and a typical casting liquidus [63].

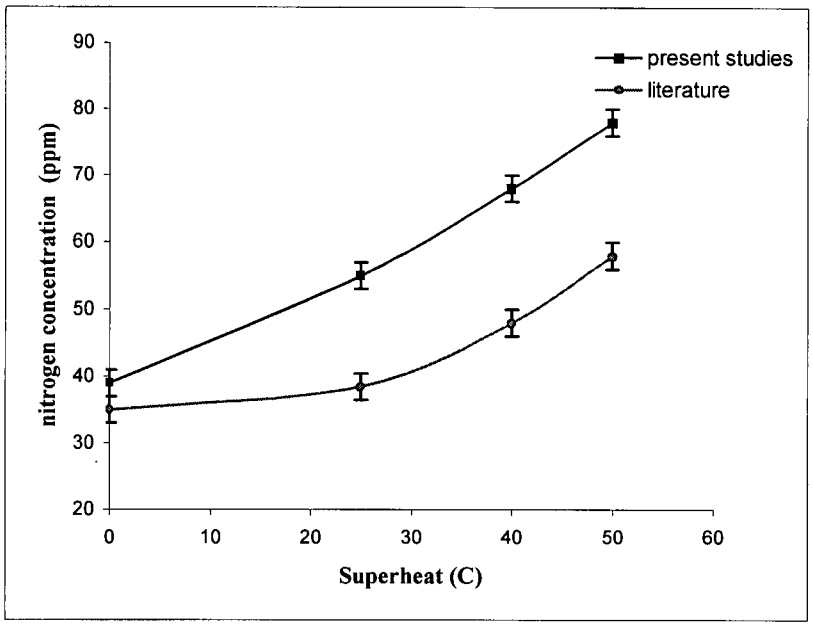

Figure 60. Variation of the equilibrium nitrogen content required for the formation of TiN with superheat, from the present studies and a typical casting liquidus [63].

Results from the present studies indicate that TiN precipitation will not take place once the equilibrium nitrogen content is below this value of 39 ppm (at T_{liq}). To provide nuclei, the nitrogen content must exceed the saturation solubility of TiN at T_{liq}, since we have established that TiN particles precipitated in the solid/liquid mushy zone will not float out of the interface.

The nitrogen partial pressure is an important variable in TiN precipitation. Higher P_{N2} can increase the equilibrium nitrogen content of the alloy to a value adequate in causing TiN

precipitation. The required nitrogen partial pressure levels for precipitation of TiN particles in typical castings of alloys is comparable to that of ambient vacuum pressures commonly used. Hence, pressure in the DS furnace is an important industrial variable.

TiN precipitation is greatly reduced when the DS experiments are conducted in a vacuum of $< 3 \times 10^{-5}$ Torr. This condition causes nitrogen degassing from the upper portions of the ingot, which in turn reduces the equilibrium nitrogen content for the formation of TiN in these regions. Consequently, TiN precipitation is restricted only to the lower portions of the ingot. This effect may also play a role in the industrial observations of random grain formation.

TiN precipitation can be minimized by conducting the DS experiments at a pressure less than 3×10^{-5} Torr or by using a very low nitrogen content sample (< 4ppm). This would ensure that the equilibrium nitrogen content for TiN formation is below the critical value and hence TiN precipitation could be eliminated above T_{liq}.

2. Segregation and nitrogen rejection:

During solidification, two important phenomenon takes place namely, a). segregation of Ti and nitrogen in the liquid/solid mushy region, and b). rejection of nitrogen into the bulk liquid.

In the solid/liquid mushy zone (the region in between the $T_{solidus}$ and $T_{liquidus}$ of the alloy), there is segregation of titanium and nitrogen. The segregation of Ti is known, as presented in Table 6. Where as, the segregation of nitrogen is yet to be determined. The segregation effects, combined with the temperature gradient in this zone causes a reduction in the saturation solubility value. Due to a decrease in the saturation solubility, there is TiN precipitation in this region. Along with the segregation effects, there is also nitrogen rejection into the bulk liquid, which increases the nitrogen concentration in the liquid above T_{liq}.

The nitrogen diffusion rate was calculated to be about 31 μm/sec, which is greater than the present withdrawal rates of 2.4 and 8.1 μm/sec. Due to nitrogen enrichment in the bulk liquid, there is TiN precipitation in the region above T_{liq}. The TiN particles thus precipitated can undergo flotation into the regions well above T_{liq}. Due to a high superheat in these regions, they get dissolved and may be re-precipitated later as solidification progresses. As solidification proceeds, the bulk liquid becomes more and more enriched in nitrogen and TiN precipitates, finally becoming accumulated at the top, which is the final portion of the ingot to solidify. The TiN particles found at the top of the final ingot, are the ones that were precipitated above the T_{liq} during solidification and which had sufficient time to grow into large particles (>10 microns in size). The rest of the ingot below this nitrogen rich portion has a nitrogen content less than the saturation solubility value of 39 ppm. A combination of the following factors such as: a). Ti and nitrogen segregation in the liquid/solid mushy region and b). nitrogen rejection into the bulk liquid, c). the grinding up of the top portion of the ingot (about 2mm from the top) and the sides, and d). a possible error (if any) in determining the equilibrium nitrogen content required for the formation of TiN in alloy IN718 (since the thermodynamic data for nitrogen solubility and TiN formation in iron alloys have been directly applied to IN718 alloy system, assuming a similar behavior), might have contributed towards the apparent reduction in nitrogen contents (to values < 25 ppm) found in all the DS samples 11-15, irrespective of their initial high equilibrium nitrogen contents.

At this point, due to the unavailability of thermodynamic data pertaining to IN718-nitrogen phase diagram, partition coefficient of nitrogen etc, the Scheil equation could not be applied to calculate the nitrogen distribution along the DS ingot. In order to get a rough estimation of the nitrogen distribution, data from the present experiments were used for k (the partition coefficient for nitrogen) and also, different partition coefficient (k) values for nitrogen were employed in order to fit the graphs obtained from Scheil equation to the experimental

graphs. A value of 0.07 for k was found to be a reasonable fit. Hence, it is speculated that the partition coefficient for nitrogen may be a value < 0.1.

3. Flotation of TiN particles

The experiments conducted with alloy IN718 indicate that the buoyancy effects in the liquid alloy do influence the flotation of TiN particles. Theoretical studies (Section 5.6) on TiN particles have revealed that since the density of TiN particles is lower than the density of the liquid alloy, the TiN particles can float in the liquid alloy depending on the viscous drag on them. For the purpose of this thesis the Stokes' principle, originally applied to spherical particle-viscous liquid system, has been extended to cubic TiN particle-liquid IN718 alloy system to calculate the velocity of rise of the TiN particles. Any discrepancy arising from the "shape effects" is assumed to be small and hence neglected.

Present experiments with 718 alloys indicate that using the withdrawal rate of 2.4μm/sec, TiN particles of size ≥ 10 microns (which have a rise velocity ≥ 28 μm/sec) are able to float and eventually get collected at the top of the ingot. These are the particles that were precipitated above the solidification front (T_{liq}) during DS. Also, at the low withdrawal rates employed (8.1 and 2.4 μm/sec), these TiN precipitates had sufficient time to grow into larger particles and hence undergo flotation.

On the other hand, particles of size between 8 and 4 microns are found throughout the ingot with a distribution such that the bigger particles are towards the upper portions and the smaller particles are towards the lower portions. This effect again substantiates the fact that the buoyancy forces do influence TiN flotation, but the effect is more pronounced when the relative difference between the velocity of rise of TiN particles and the withdrawal rate is substantial. These are the TiN particles precipitated in the solid/liquid mushy region.

The smaller TiN particles < 4 microns are found at the bottom portions of the ingot which indicates that these particles may be precipitated later during solidification in the solid/liquid mushy zone and thus didn't "escape". Hence, for substantial flotation to occur the withdrawal rate should be at least an order lesser than the velocity of rise of the TiN particles.

4. Low Nitrogen Sample:

When the sample has a very low nitrogen content, by directionally solidifying the sample in a nitrogen atmosphere the nitrogen content of the liquid alloy can be increased such that it exceeds the equilibrium nitrogen content required for TiN precipitation. Hence, under such condition, it is possible to have TiN precipitation as well as flotation of bigger TiN particles (>10 microns in size).

8.2 Recommendations For Future Work

- The ingots used for the present experiments are about 5 mm in diameter and 50 mm in length, which is very small, compared to the ingots used in practice. Hence, a similar investigation could be carried out by redesigning the DSQ furnace to accommodate a larger ingot. Also, the induction coil design can be manipulated in order to give a shallow temperature gradient with a longer plateau region, to achieve a lesser superheat in the alloy and yet maintain a fairly constant temperature above the liquidus temperature of the alloy.

- Since in practice random grain formation has been observed in single crystal turbine blades like in alloy CMSX-4 and alloy SC-16, it would be beneficial to study the inclusion behavior in these alloys rather than in alloy IN718 (a preliminary theoretical study is presented in Appendix 5. Hence, the present work can be extended to these single crystal alloys.

- A preliminary theoretical study on HfN formation in superalloys and the effect of Hf addition in alloy IN718 has been done in the present studies (presented in Appendix 4). Since HfN is found to be the chief nitride inclusion in single crystal superalloys containing Hf, similar experimental studies can be carried out in alloys containing hafnium. Note that HfN is denser than liquid superalloys and so should not exhibit any flotation effects.

References:

1. Mitchell. A, Cockroft. S.L, Schvezov. C.E, Schmalz. A.J, Loquet. J.N, and Fernihough. J, "Primary Carbide And Nitride Precipitation In Superalloys Containing Niobium", High temperature materials and processes, Vol.15, no. 1-2, pp. 27-40, 1996.

2. Rupp. S, Bienvenue. Y, and Massol. J, "High Temperature Alloys For Gas Turbines And Other Applications 1986", Eds. D. Coutsouradis et al, publ. D. Reidel publishing Co. 1986, Part 2, 1986.

3. Mitchell. A, "The Present Status of Melting Technology for Alloy 718", Superalloy 718-Metallurgy and Applications, Eds. E.A. Loria, The Min. Met. and Materials Soc., pp. 1-15, 1989.

4. Pollock. T.M, Murphy. W.H, Goldman. E.H, Uram. D.L, and Tu. T.S, "Grain Defect Formation During Directional Solidification of Nickel Base Single Crystals", Superalloys 1992, TMS Warrendale, PA, pp. 125-134, 1992.

5. Pollock. T.M, and Murphy. W.H, "The Breakdown of Single Crystal Solidification in High Refractory Nickel-Base Alloys", Met. and Mat. Trans. A, Vol. 27A, pp. 1081-1094, 1996.

6. Cockroft. S.L, Rappaz. M, Mitchell. A, Ferniough. J, and Schmaltz. A.J, "An Examination of the Manufacturing Problems of Large Single-Crystal Turbine Blades For Use in Land-Based Gas Turbines", Materials for Advanced Power Engineering, Part II, pp. 1145-1154, 1994.

7. Turnbull. D, and Vonnegut. B, "Nucleation Catalysis", Industrial and Engineering Chemistry, Vol. 44, no.6, pp. 1292-1297, 1956.

8. Chalmers. B, J. of Aust. Inst. Metals, Vol. 8, pp. 255, 1963.

9. Winegard. W, and Chalmers. B, Trans. Quart. ASM, Vol. 46, pp. 1214, 1954.

10. Fredriksson. H, and Hillert. M, "On the Formation of the Central Equiaxed Zone in Ingots", Met. Trans. A, Vol.3, pp. 565-570, 1972.

11. Fredriksson. H, and Olsson. A, "Mechanism of Transition From Columnar to Equiaxed Zone in Ingots", Materials Science and Technology, Vol.2, pp. 508-516, 1986.

12. Cole. G.S, Casey. K.W, Bolling. G.F, Met. Trans. Vol. 1, pp. 1413, 1970.

13. Campbell. J, and bannister. J.W, Metals Technology, Vol. 2, pp. 409, 1975.

14. Jackson. K.A, Hunt. J.D, Uhlmann. D.H, and Seward. T.P III, Trans. TMS-AIME, Vol. 236, pp. 149, 1966.

15. Langenberg. F.C, Prestel. G, and Honeycutt. C.R, Trans. TMS-AIME, Vol. 221, pp. 993, 1961.

16. Southin. R.T, Trans. TMS-AIME, Vol. 236, pp. 220, 1967.

17. Doherty. R.D, and Feest. E.A, ISI Publication 110, pp. 102, 1968.

18. Witzke. S, Riquet. J.P, and Durand. F, "Diffusion Field Ahead of a Growing Columnar Front : Discussion of The Columnar-Equiaxed Transition", Acta Met. Vol. 29, pp. 365-374, 1981.

19. Burden. M.H, and Hunt. J.D, Journal of Crystal Growth, Vol. 22, pp. 99 and 109, 1974.

20. Sharp. R.M, and Hellawell, J. Crystal Growth, Vol. 6, pp. 253, 1970.

21. Backerud. L, and Chalmers. B, Trans. TMS-AIME, Vol. 245, pp. 309, 1969.

22. Doherty. R.D, Feest. E.A, and Holm. K, Met. Trans. Vol. 4, pp. 115, 1973.

23. Trivedi. R, Acta Met. Vol. 18, pp. 287, 1970.

24. Burden. M.H, and Hunt. J.D, "Mechanism for the Columnar to Equiaxed Transition in Casting Ingots", Met. Trans. Vol. 6A, pp. 240-241, 1975.

25. Tarshis. C.A, Walker. J.L, and Rutter. J.W, Met. Trans. Vol. 2, pp. 2589, 1971.

26. Prates. M, Fissolo. J, and Biloni. H, Met. Trans. Vol. 3, pp. 1419, 1972.

27. Coates. D.E, Subramanian. S.V, and Purdy. G.R, "Solid-Liquid Interface Stability During Solidification of Dilute Ternary Alloys", Trans. Met. Soc., AIME, Vol. 242, pp. 800-809, 1968.

28. Bobadilla. M, Lacaze. J, and Lesoult. G, J. of Crystal Growth, Vol. 89, pp. 531-554, 1988.

29. Rappaz. M, David. S.A, Vitek. J.M, and Boatner. L.A., "Analysis of Solidification Microstructures in Fe-Ni-Cr Single Crstal Welds", Met. Trans. A, Vol. 21A, pp. 1767-1722, 1990.

30. Kurz. W, Giovanola. B, and Trivedi. R, "Theory of Microstructural development During Rapid Solidification"" Acta Met. Vol. 34, no. 5, pp. 823-830, 1986.

31. Ivanstov. G.P, Doklady Akademii Nauk SSSR, Vol. 58, pp. 567, 1947.

32. Erdeljac. J.P, Henein. H, and Mitchell. A, "Melting Kinetics of Segregated Particles in VAR 718", ISS Transactions, Vol. 6, pp. 51-63, 1985.

33. Hunt. J.D, "Steady State Columnar to Equiaxed Growth of Dendrites and Eutectic", Materials Science and Engineering, Vol. 65, pp. 75-83, 1984.

34. Rappaz. M, Int. Materials Rev. Vol. 34, pp. 93-123, 1989.

35. Meyer. M, Dedecke. D, Paul. U, and Sahm. P.R, "Undercooling Related Casting Defects In Single Crystal Turbine Blades", Superalloys 1996, Warrendale, PA, pp. 471-479, 1996.

36. Yu. KO, Nicholas. J.J, and Robinson. M, JOM, Vol. 44, p. 21, 1992.

37. Tu. J.S, Foran. R.K, JOM, Vol. 44, p. 26, 1992.

38. Imwinkelried. Th, Desbiolles. J.L, Gandin. A, Rappaz. M, Rossmann. S, and Thevoz. Ph, " Modeling of Dendriric Single Crystal Solidification at the Macro- and Microscopic Levels : Application to Turbine Blades", Modeling of Casting, Welding and Advanced Solidification Processes -VI, TMS- Min. Met. and Materials Soc., pp. 63-70, 1993.

39. Quested. P.N, McLean. M, and Winstone. M.R, "Evaluation of Electron Beam Cold Hearth Refining (EBCHR) of Virgin and Revert IN738LC", Superalloy 1988, The Min. Met. and Materials Soc., 1988.

40. Shahapurkar. D.S, and Small. W.M, Metall. Trans. Vol. 18B, pp. 231-235, 1987.

41. Huang Xuebing, "Effect of Nitrogen on Nickel based superalloys - Microstructure and Properties", Ph.D. Thesis, Institute of Metal Research, Chinese Academy of Science, Shenyang, P.R. China, 1998.

42. Lamberigts and Lecomte-Beckers, "Reverting Foundry Nickel-Base Superalloys", High Temperature Materials for Gas Turbines and Other Applications, pp. 777-787, 1986.

43. Painter. R.E, Quested. P.N, and Young. J.M, "Effect of Nitrogen Additions on the Casting Quality of Ni-Based Superalloys", Solidification Processing 1987, The Inst. Of Metals, pp. 23-25, 1988.

44. Liu, Zhen, Banerji, Reif, and Fu, "Effect of Solidification Parameters on the Microstructure of IN738LC Ni Based Superalloy", The Eleventh International Conference on Vacuum Melting, pp. 83-85, 1992.

45. Pardo. E, Villafuerte. J.C, and Kerr. H.W, "A Fine Element Study of the Columnar-Equiaxed Transition in GTA Welding of Stainless Steels", Recent Trends in Welding Science and Technology, ASM International, pp. 159-164, 1985.

46. Bramfit, B.L, "The Effect of Carbide and Nitride Additions on the Heterogeneous Nucleation Behaviour of Liquid Iron", Met. Trans. Vol. 1, pp. 1987-1995, 1970.

47. Poole. W.J, Mitchell. A, and Weinberg. F, "Inoculating Stainless Steel With Titanium Nitride", High Temperature Materials And Processes, Vol. 16, No. 3, pp. 173-182, 1997.

48. Ohashi. T, Fujii. H, Nuri. Y, and Asano. K, "Effect of Oxides on Nucleation Behavior in Supercooled Iron", Transactions ISIJ, Vol. 17, pp. 262-269, 1977.

49. Ferniohugh. J, "The Columnar to Equiaxed Transition in Nickel Based Superalloys AM1 and MAR-M200 Hf', Ph.D Thesis, UBC, 1995.

50. Durbar. G.L.R, Osgerby. S, Quested. P.N, Met. Technology, Vol. 11, pp.129-137, 1984.

51. Painter. R.E, and Young. J.M, "Liquid Metal Treatments to Reduce Microporosity in Vacuum Cast Nickel Based Superalloys", The Met. Soc. AIME, pp. 417-425, 1988.

52. Ford. D.A, Hooper. P.R, and Jennings. P.A, " Foundry Performance of Reverted Alloys For Turbine Blades", High Temperature Alloys For Gas Turbine and Other Applications – I, Liege, Belgium, pp. 51-80, 1986.

53. Painter. R.E and Young. J.M, "The Role of Nitrogen on Microstructure of Recycled Nickel-Based Superalloys", 25th Annual Conference of Metallurgists, pp. 243-260, 1986.

54. Karin Frisk, "Solubility of N in Cr-Fe-Mo-Ni Alloys", Met. Transactions A, Vol. 23A, pp. 1271-1278, 1992.

55. Small. W.M, and Pehlke. R.D, "The Effect of Alloying Elements on the Solubility of Nitrogen in Liquid Iron-Chromium-Nickel Alloys", Transactions of the Met. Soc. of AIME, Vol. 242, pp. 2501-2505, 1968.

56. Liao. L and Fruehan. R.J, "Thermodynamics of Ti, Al and Inclusion Formation in Stainless Steel and Nickel Alloys", Transactions of the ISS, I&SM, pp. 91-97, 1989.

57. Heinrich Feichtinger, Xiao-hong Zheng and Christoph Rennhard, "Measurements of Nitrogen Solubility in Iron-Nickel Alloys, Using a New Temperature Gradient Method", Steel Res., Vol. 61, no. 1, pp. 26-29, 1990.

58. Harue Wada and Robert D. Phelke, "Nitrogen Solution and Titanium Nitride Precipitation in Liquid Fe-Cr-Ni Alloys", Met. Trans. B, Vol. 8B, pp. 443-450, 1977.

59. Rawers. J, Bennet. J, Doan. R, and Siple. J, "Nitrogen Solubility and Nitride Formation in Fe-Cr-Mn-Ni Alloys", Acta Mater. Vol. 40, no. 6, pp.1195-1199, 1992.

60. Bol'shov. L.A, Stomakhin. A.Ya, Sokolov. V.M, and Teterin. V.G, " Solubility of Nitrogen in Multicomponent Nickel-Based Melts", Russian Metallurgy, pp. 64-67, 1985.

61. Okomoto. M, Tanaka. R, Naito. T, and Fujimoto. R, Tetsu-to-Hagane 2, no.25, 1962.

62. Cockroft. S.L, Degawa. T, Mitchell. A, Tripp. D.W, and Shmaltz. A, "Inclusions and the EB Refining of Superalloys", Conference on Electron Beam Refining, Bakish Materials Corp., pp. 143-159, 1992.

63. Mitchell. A, "Thermochemistry of Inclusions in Superalloys", Advanced Materials and Processing Techniques, Eds. Froes. F.H, ASM Europe, pp. 233-241, 1987.

64. Cockroft. S.L, Degawa. T, Mitchell. A, Tripp. D.W, and Smaltz. A, "Inclusion Precipitation in Superalloys", Superalloys 1992, The Min. Met. and Materials soc., pp.577-586, 1992.

65. Kubaschewski. O, Alcock. C.B, "Metallurgical Thermochemistry", 5th Edition Oxford: Permagon Press, 1979.

66. Elliot. J.F, "Physical Chemistry Of Liquid Steel", Electric Furnace Steel Making, pp. 301-304, 1985.

67. Turkdogan. E.T, "Physical Chemistry of High Temperature Technology", Academic Press, New York, 1980.

68. Auburtin. P, "Determination Of The Influence of Interdendritic Segregation During The Solidification Of Freckle prone Alloys", M.A.Sc Thesis, UBC, Canada, pp. 112, 1995.

69. Bouse. G.K, and Mihalisin. J.R, "Metallurgy of Investment Cast Superalloy Components", Superalloys, Supercomposites and Superceramics, Eds. Tien. J.K, and Caulfield. T, Materials Science Series, p. 122, 1989.

70. Hellawell. A, Sarazin. J.R, and Steube. R.S, "Channel Convection in Partly Solidified Systems", Phil. Trans. Royal Soc. Lon. A-345, pp. 507-544, 1993.

71. Sarazin. J.R, and Hellawell. A, "Segregation Arising From Natural Convection During Solidification", EPD Congress '91, The Min. Metals and Materials Soc. Pp. 511-522, 1991.

72. Sarazin. J.R, and Hellawell. A, "Channel Flow in Partly Solidified Alloy Systems", Advances in Phase Transitions, pp. 101-115, 1987.

73. Bower. T.F, Brody. H.D, and Flemings. M.C, "Measurements of Solute Redistribution in Dendritic Solidification", Transactions of The Met. Soc. AIME, Vol. 236, pp. 624-634, 1966.

Appendix: 1

An interesting aspect regarding the shape of TiN particles in alloy IN718 is that two different shapes are encountered in this study: a). cubic and b). hexagonal. In the previous studies related to TiN precipitation in iron and nickel alloys, only cubic TiN particles have been reported. It is further seen that the hexagonal TiN particles are very often associated with an alumina core. Figure 61 (a), and (b) present a hexagonal and a cubic TiN precipitate respectively, found in the directionally solidified IN718 samples from the present studies. The smaller TiN particles (of size < 4 microns) often are cubic in structure and are found to be devoid of an alumina nucleus. Although, few cubic TiN particles have been observed with an alumina core.

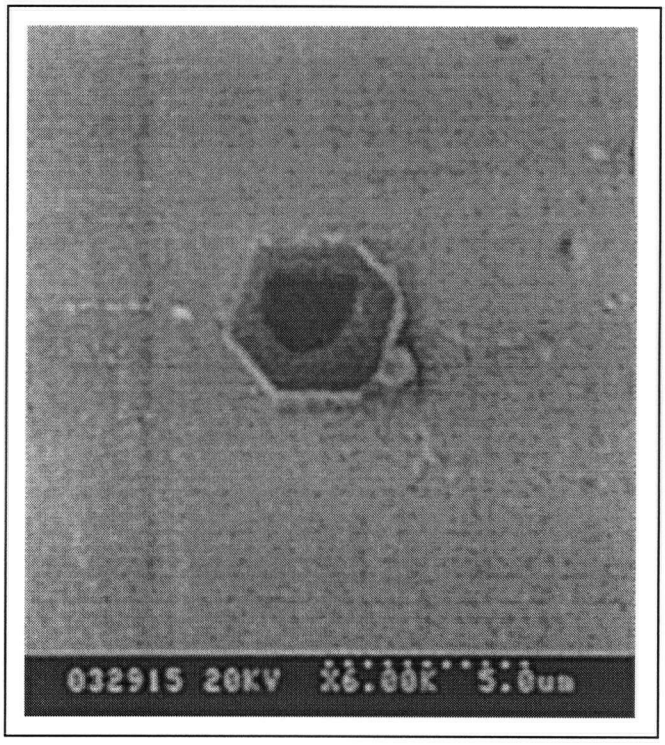

(a)

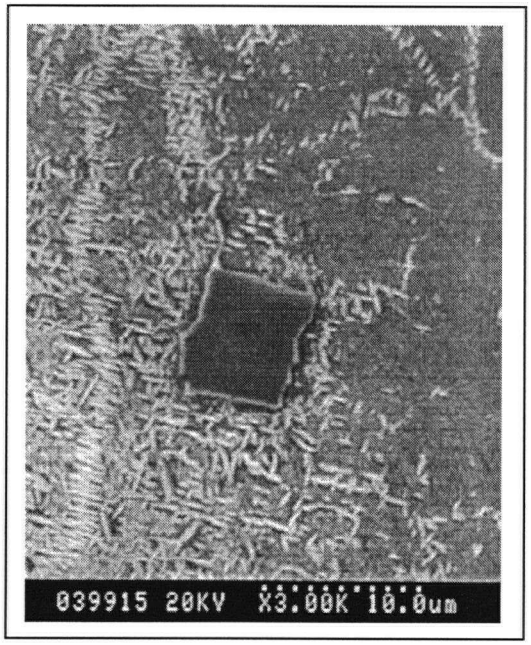

(b)

Figure 61. (a), and (b) a hexagonal and a cubic TiN precipitate respectively.

Hexagonal TiN particles have not yet been reported in literature. The hexagonal TiN particles found in this study are invariably associated with an alumina core. The alumina particle has a hexagonal crystal structure. Since the TiN particle precipitates on the alumina nucleus, this may be influential in causing the TiN particle to grow in a hexagonal crystallographic orientation. It needs to be proved by using conventional techniques for crystal structure determination, like the x-ray crystallographic method if they are in fact hexagonal TiN particles.

Appendix: 2

The TiN agglomerations are very often found to be bridged by alumina particles. This indicates that the alumina particles act as a nucleus for the precipitation of TiN particles and the agglomerate TiN particles are held together by alumina particles. Figure 62(a), and (b) show portions from the top of the 90 ppm [N], 718 DS cast 90 ppm [N] content samples (9) and (13) at (a nitrogen pressure of 100 microns and 400 microns respectively) . The Figures show large number of TiN agglomerations with alumina particles in between holding them together. An EDX microprobe analysis of these portions shows about 44% alumina and 55% Ti (TiN distribution). Figure 63 presents TiN particles which are bridged by alumina particles. These observations substantiate the previous studies by Mitchell et al [63] which have indicated that the TiN agglomerations are bridged by alumina particles. This might be the reason why TiN particles sticks preferentially to the ceramic mold surface in the present study.

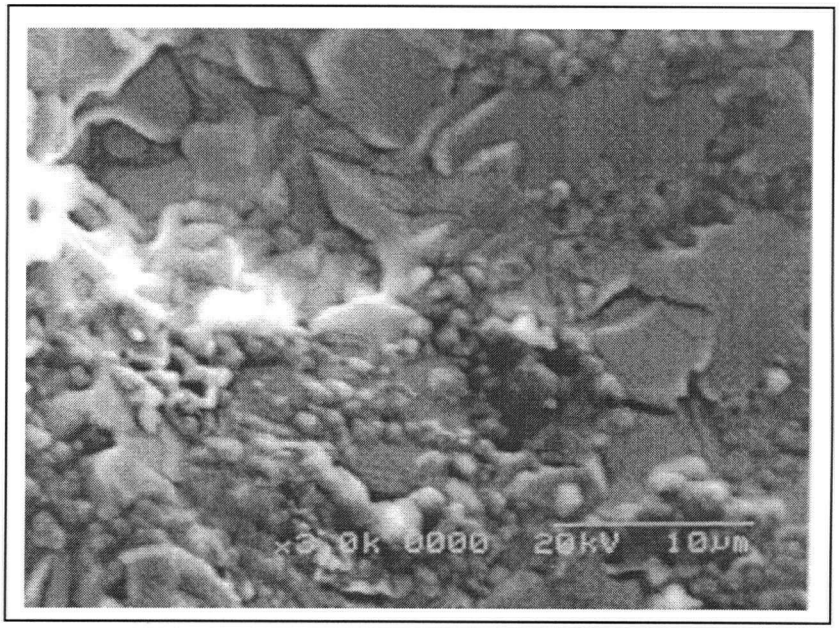

(a)

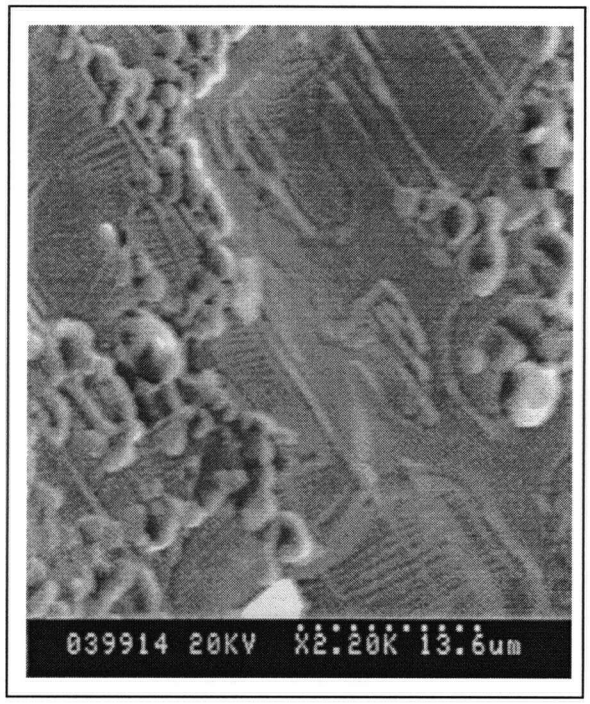

(b)

Figure 62 (a) and (b) TiN agglomerations bridged by alumina particles.

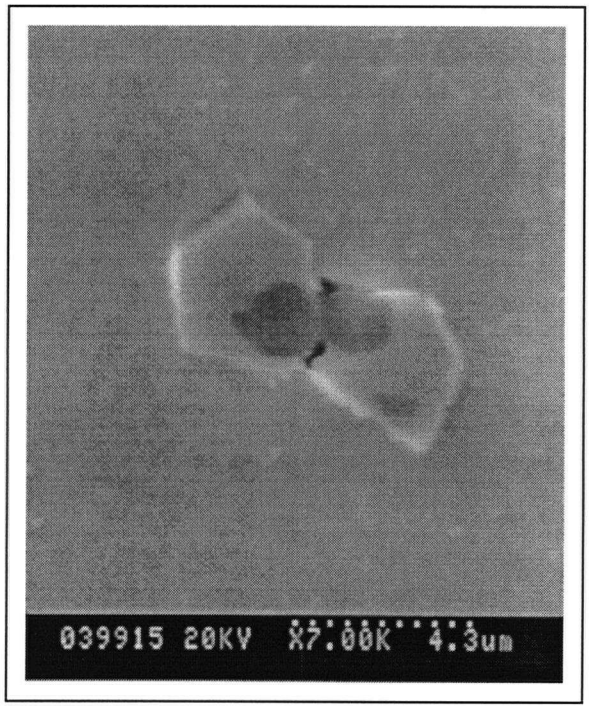

Figure 63. TiN inclusions bridged by alumina particles

Appendix : 3

Two directionally solidified IN718 ingots (were prepared in the induction furnace at a vacuum of 10 microns at two different temperature gradients. Sample 8H was directionally solidified at a high temperature gradient of 27 °C/cm and sample 8L was directionally solidified at a low temperature gradient of 11 °C/cm. The withdrawal rate employed was 33 μm/sec. These samples were then severed into four equal pieces. A portion from each piece was sent to Special Metals Corp. New York, for nitrogen analysis. This data is presented in Table 12.

Sample number (high G)	Nitrogen (ppm)
8H1A (top)	42.1
8H2A	34.8
8H3A	39.9
8H4A (bottom)	62.4

(a)

Sample number (Low G)	Nitrogen (ppm)
8L1A	57.8
8L2A	43.6
8L3A	55.2
8L4A	61.4

(b)

Table 12. Nitrogen distribution along the DS cast ingots a) high temperature gradient, b) low temperature gradient.

From Table 4, the equilibrium nitrogen content at a pressure of 10 microns is determined to be 25 ppm. In Chapter 7 it is discussed that rejection of nitrogen into the bulk liquid is a very significant factor which contributes to the accumulation of nitrogen and TiN particles at the top portion of the ingot. Also, using equation 37 the nitrogen diffusion rate was calculated to be about 32 μm/sec, which is comparable to the withdrawal rate of 33 μm/sec at which these 718 samples are cast. Hence, nitrogen diffusion is not fast enough to cause a significant nitrogen

degassing which have been observed in samples that were directionally solidified at a lower withdrawal rate of 8.1 or 2.4 μm/sec. We still see a decrease in the nitrogen content, but not as much as that observed in the previous cases (in samples 11-15). If there is the same partitioning between the liquid alloy and the solute, we should see a decease in the total nitrogen content, which we do, and there should be an elevated nitrogen content at the top, which there is.

The top portion of the ingot was polished and observed under the SEM for TiN particles. TiN particles were not found at the top of the ingot. This is because, at this withdrawal rate, the TiN particles neither have sufficient rise velocity to float, nor sufficient time to grow into larger particles and float. Since the nitrogen analysis shows a nitrogen content above the saturation solubility value (> 39 ppm at the liquidus temperature), there were TiN particles precipitated above the T_{liq} (1340 ^{0}C), but these particles must have been a part of the solution re-precipitated nitrides.

Appendix : 4

Effect of argon:

Homogeneous 90 ppm [N] samples were directionally solidified under argon pressure to study the influence of an inert atmosphere on TiN precipitation. Table 13 presents the directional solidification experiments conducted on the 90 ppm [N] content samples 18 and 19.

Sample 90 ppm [N]	Withdrawal rate R (μm/sec)
18	8.1
19	2.4

Table 13. Directional solidification experiments conducted under argon atmosphere.

Figure 64 presents the nitrogen distribution and Figure 62 presents the TiN distribution along the DS cast samples 18 and 19 along with that for samples 7 and 8 [90 ppm [N] samples DS cast under vacuum of 3.5×10^{-5} Torr, at 8.1 and 2.4 μm/sec respectively] for comparison.

- From Fig. (64) it can be seen that the nitrogen contents are almost a constant for experiments conducted under argon pressure, when compared to the experiments conducted under vacuum (which indicate a higher nitrogen content at the bottom of the ingot relative to the upper portions).
- From Figure 65 it can be seen that there is a higher TiN concentration at the top of sample 7 (at R= 8.1 μm/sec), when compared to samples 7 and 8 cast under vacuum. An examination of the outer surface of the samples 18 and 19 indicate large TiN particles sticking to the

outer walls (which could not be taken into the nitride counting). This presented in Figure 66 (a) and (b). Hence, the TiN counting is found to be very subjective.

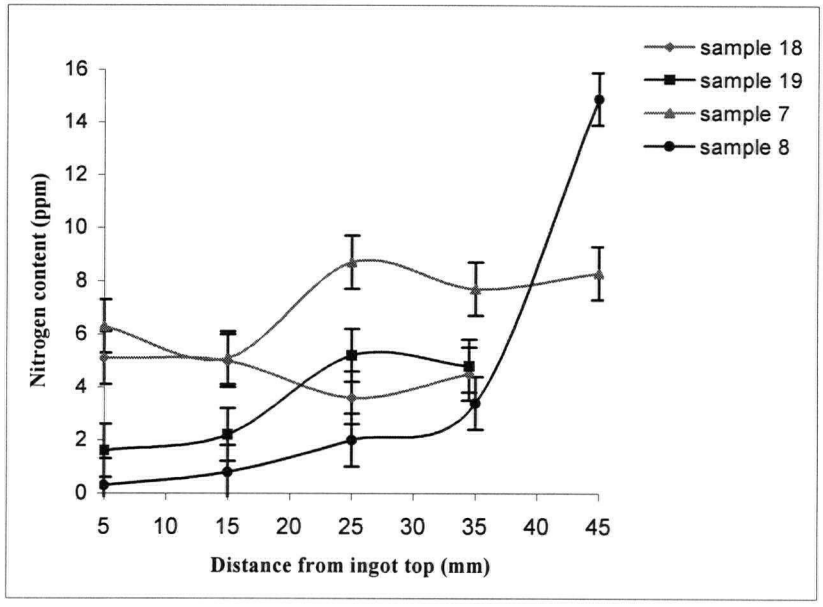

Figure 64. Nitrogen distribution in samples 18, 19 (DS cast under argon pressure of 100 microns), 7 and 8 (DS cast at 3.5 x 10^{-5} Torr, and at 8.1 and 2.4 μm/sec respectively).

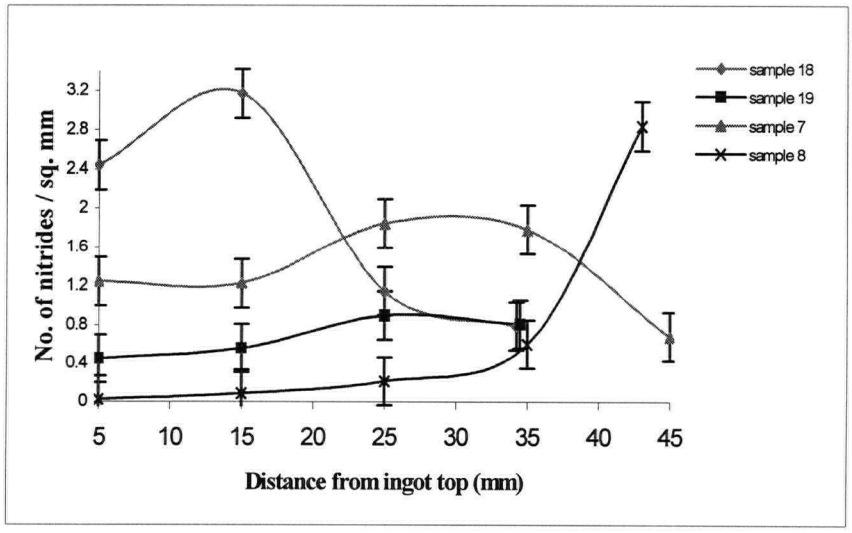

Figure 65. TiN distribution in samples 18, 19 (DS cast under argon pressure of 100 microns), 7 and 8 (DS cast at 3.5 x 10^{-5} Torr, and at 8.1 and 2.4 μm/sec respectively).

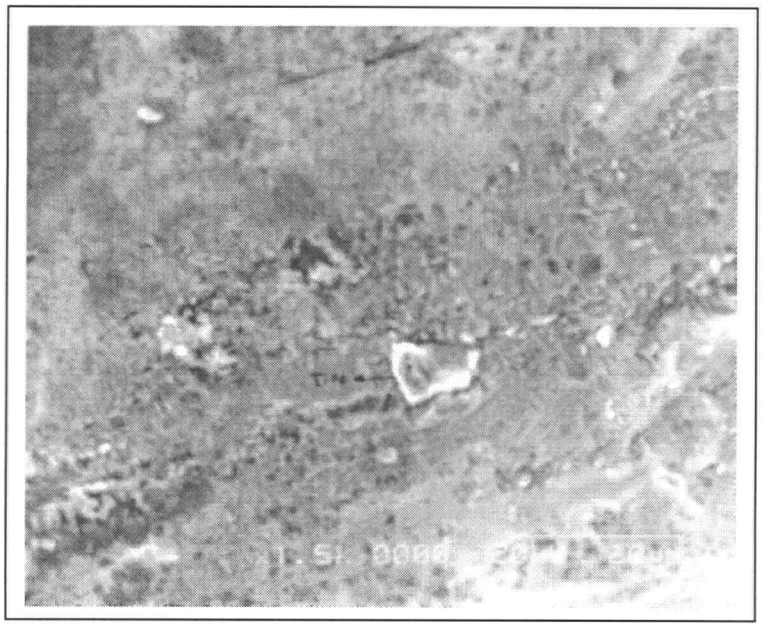

(a)

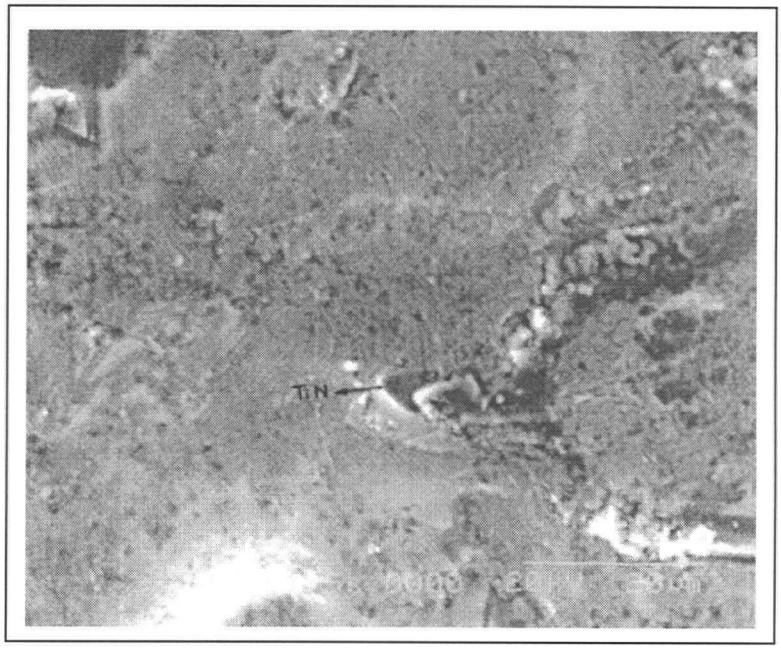

(b)

Figure 66 (a) and (b). TiN inclusions on the outer walls of the Directionally Solidified samples 18 and 19.

From the above DS experiments conducted on IN718 samples under argon pressure, it was found that there is almost a uniform nitrogen distribution along the ingots, irrespective of the withdrawal rate. Also it appears that during directional solidification, the larger TiN particles stick to the outer surface of the ingot.

The purity of the argon gas used for this study is about 99.99%, containing about 15 ppm nitrogen. Hence the presence of nitrogen may have influenced the results to a certain extent.

Appendix : 5

Effect of hafnium addition :

In single crystal Ni-based superalloys (like alloy CSMX-4, where the nominal composition of Ti and Hf are 1 wt % and 0.1 wt. % respectively), the stable nitrides found are hafnium nitrides. Taking the general reaction for the formation of TiN (equation 21, TiN $\Leftrightarrow$ [Ti] + [N]) an attempt was made here to determine what would be the effect on the solubility of TiN if Hf is added to IN718 alloy. Assuming that HfN formation is similar to TiN formation in Ni-based superalloys, the reaction can be written as:

$$HfN_s \Leftrightarrow [Hf]_l + [N]_l \qquad (41)$$

The solubility constant is given by:

$$K_{HfN} = [\%Hf]\,[\%N].\, f_{Hf}.f_N \qquad (42)$$

The activity coefficient of Hf was assumed to be the same as that for Ti (0.372, since no further data were available for Hf). Considering the free energy of formation of TiN (-73 Kcal / mol) and HfN (-81 Kcal / mol) at 1500 K , and substituting them in the free energy equations for reactions 21 and 37, the solubility constant for HfN can be calculated. From this data, the equilibrium nitrogen concentration required for the formation of HfN can be calculated. Considering an alloy with 0% Ti, and gradually increasing the Hf content, the equilibrium nitrogen content for the formation of HfN has been calculated at the liquidus temperature (1340 ^{o}C). This data is presented in Table 14. It can be seen that with Hf addition, the solubility limit decreases.

Wt. %Hf	$[N]_{eqm}$ ppm
0.4	6.3
0.6	4.2
0.8	3.2
1	2.5
1.2	2.1
1.4	1.8

Table 14. Effect of Hf addition on the equilibrium nitrogen contents for HfN formation at T_{liq} (1340 °C) in alloy IN718.

Appendix : 6

Extending the calculations for the solubility of nitrogen and formation of TiN in alloy IN718 (discussed in chapter 2), a similar procedure is adopted here for a typical single crystal alloy CMSX-4.

Solubility Of Nitrogen:

The dissolution of nitrogen in liquid iron alloys can be applied to Ni-based superalloys:

$$\frac{1}{2}N_2(g) = [N] \text{ (1 wt\% liquid iron)} \quad (42)$$

The solubility constant (k) for the above reaction is given by:

$$k = \frac{f_n[N]}{P_{N_2}^{1/2}} \quad (43)$$

Where, f_n is the activity coefficient of nitrogen. The free energy of the reaction is given by [65]:

$$\Delta G^o = 3598 + 23.89T \text{ Joules} \quad (44)$$

Applying a similar procedure to calculate the activity coefficient of nitrogen in alloy IN718(as discussed in chapter 2), the activity coefficient of nitrogen in alloy CMSX-4 was found to be 0.323. The solubility constant for the equation 43 at the liquidus temperature for alloy CMSX-4 (1390 °C) was found to be 0.0436. The solubility of nitrogen at various pressures can be calculated as presented in Table 15. At the liquidus temperature of the alloy (1390 °C), the solubility of nitrogen is found to be 8 ppm at a pressure of 3.5×10^{-5} atm.

Solubility of TiN:

The dissolution of TiN in nickel based alloys is given by equation 21. The free energy for the reaction is given by [67]:

$$\Delta G^{o} = 308780 - 114.35T \text{ Joules} \quad (45)$$

The activity coefficients for Ti and nitrogen were determined to be 0.727 and 0.323 respectively. The solubility constant K was calculated to be 1.88×10^{-4} (at the liquidus temperature).

P_{N2} (atm)	[N] ppm
5×10^{-4}	30
8×10^{-5}	12
3.5×10^{-5}	8
7×10^{-6}	3.5
5×10^{-7}	1

Table 15. Relation between the equilibrium nitrogen contents required for the formation of TiN and P_{N2} for alloy CMSX-4 (at 1390^{0}C).

T (^{o}C)	Superheat (^{o}C)	[N] ppm
1390	0	8
1440	50	15
1490	100	28
1540	150	51

Table 16. Equilibrium nitrogen content required for TiN formation in alloy CMSX-4 above T_{liq} (1390^{0}C).

Table 16 presents the equilibrium nitrogen contents required for the formation of TiN in alloy CMSX-4, above the liquidus temperature (1390 ^{0}C), at a pressure of 3.5 x 10 $^{-5}$ Torr. It can be seen that the solubility of TiN in alloy CMSX-4 increases with an increase in the superheat.

Appendix : 7

Apart from the TiN inclusions, carbides, carbo-nitrides, delta and laves phases have been observed. The carbides are niobium carbides which are invariable cubic in structure. They are grayish or bluish gray in color under an optical microscope. Figure 67 presents an SEM picture of some niobium-carbides found in the DS 718 sample.

The carbo-nitrides mostly have an inner-most alumina core surrounded by a TiN phase, which are together enveloped by a grayish niobium carbide phase. Note that TiN particles are precipitated first and the carbides are precipitated later during solidification (below the carbide solution temperature of 1280 °C). These are large precipitates > 10 microns in size and are near the bottom of the directionally solidified ingot (due to phase precipitation equilibrium). Figure 68 presents a typical carbo-nitride found in the DS cast 718 samples.

The laves phase and the needle shaped delta phases are niobium rich phases. They are the Ni_3Nb phases distributed through out the DS cast ingot.

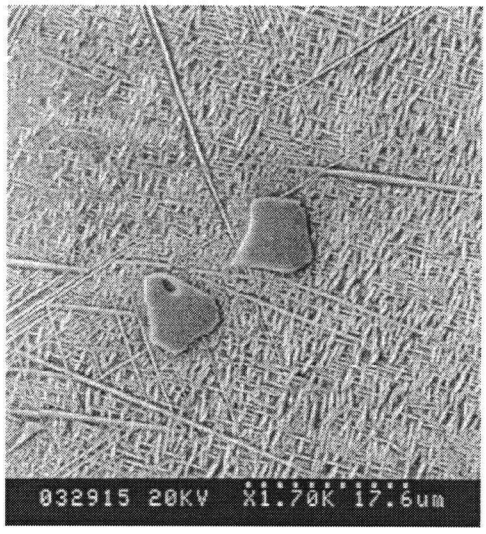

Figure 67. SEM picture of Niobium Carbides.

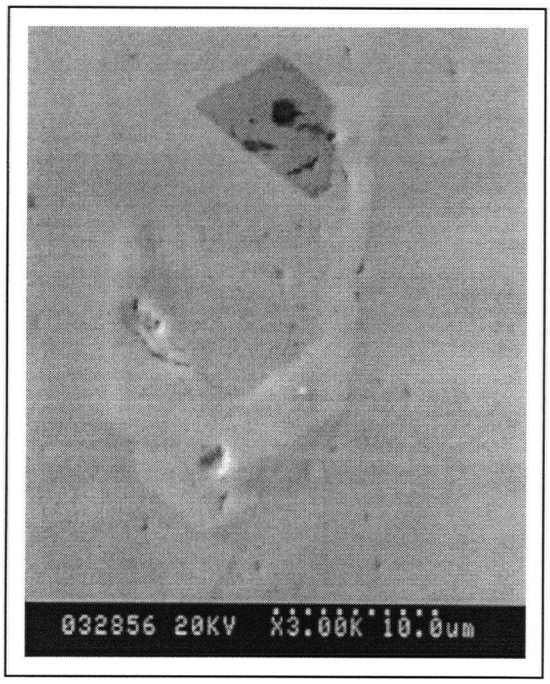

Figure 68. A typical carbonitride (TiN with an alumina core and surrounded by Nb carbide phase)

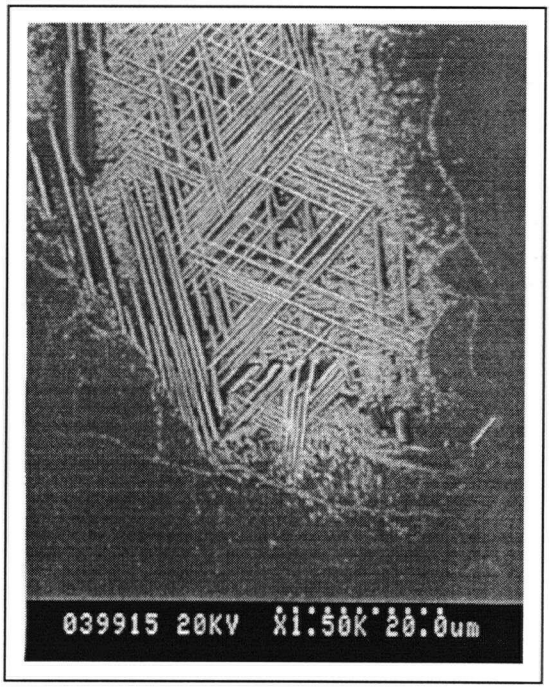

(a)

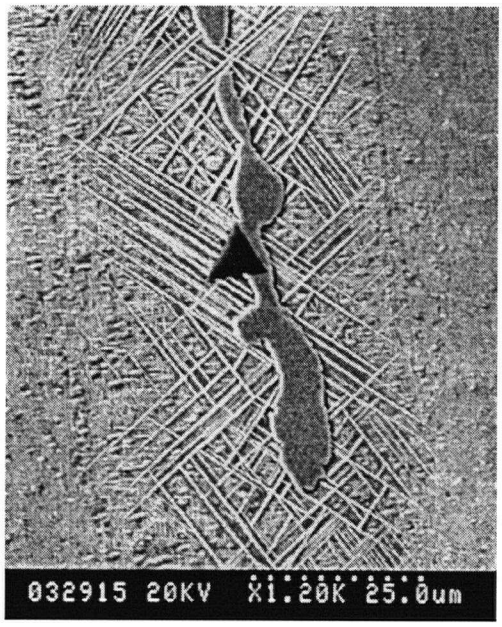

(b)

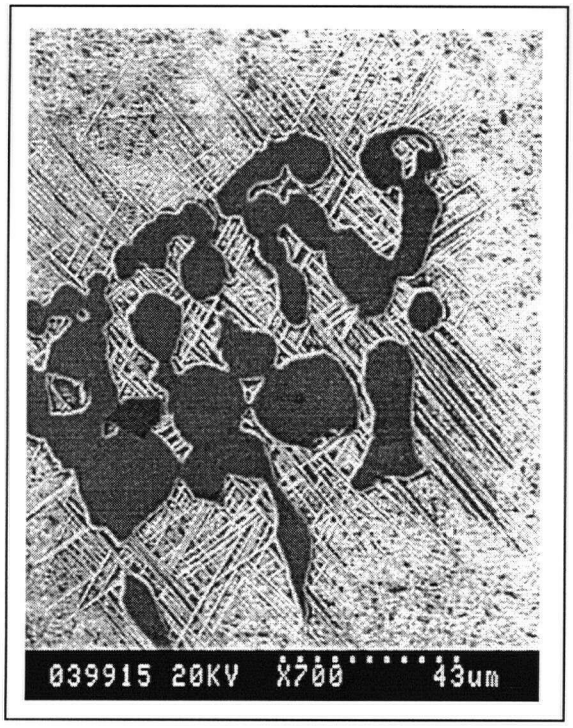

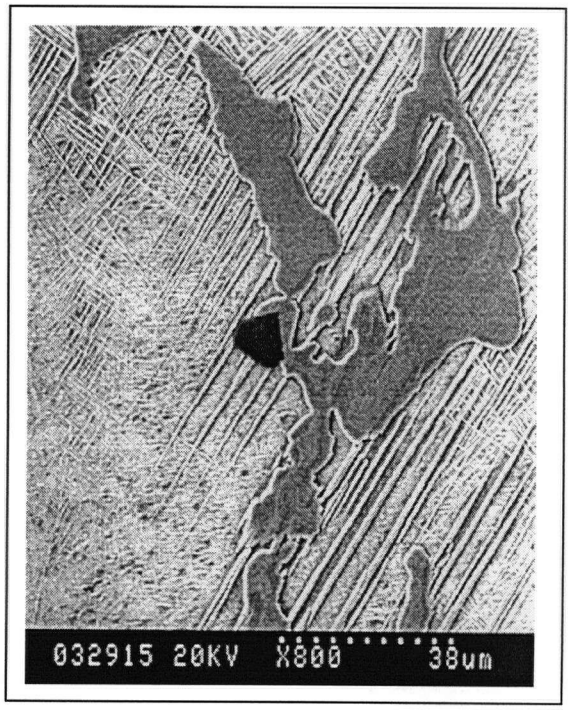

(c) (d)

Figure 69 (a) Delta phase, (b) needle shaped delta phase surrounding a TiN inclusion (c) and (d) TiN inclusion enveloped by Nb rich Laves phases.

Mostly the niobium rich phases are found enveloping the TiN particles. Figures 69 (a), (b), (c), and (d) show the needle shaped delta (Ni_3Nb), niobium rich Laves phases enveloping titanium nitrides.

Appendix : 8

The very top of the DS cast IN718 ingots invariably have a chromium rich deposit. Figure 70 shows a SEM picture of the very top of the sample. A combination of high temperature and low pressure is effective in vaporizing the chromium from the ingot and causing a chromium rich deposit on the walls of the crucible above the ingot and also on the top of the ingot. Figure 71 shows a large TiN particle amidst chromium globules found on the upper outer surface of a DS cast IN718 ingot.

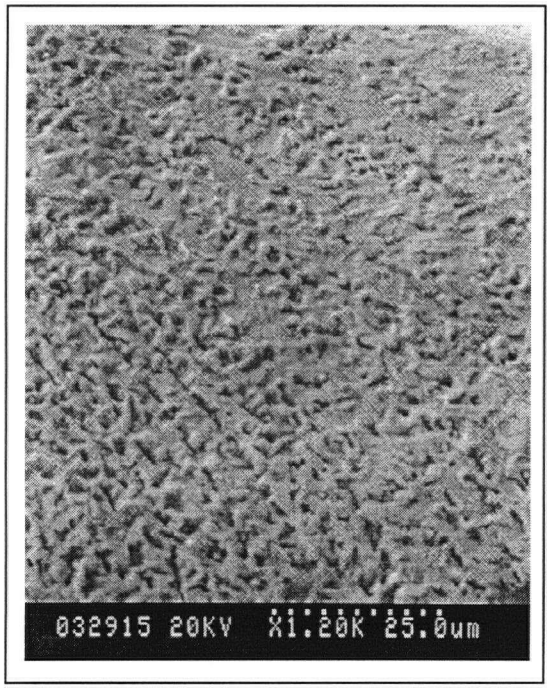

Figure 70. Chromium rich deposit on the top of the ingot.

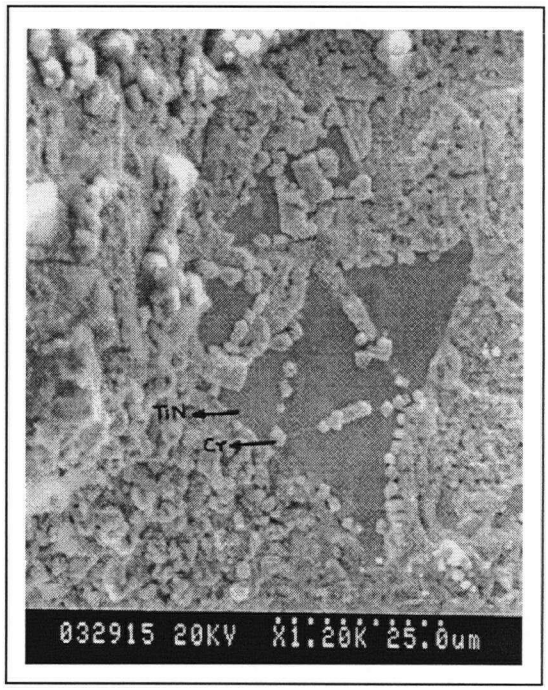

Figure 71. A TiN particle amidst chromium globules on the upper outer surface of the DS cast ingot.